Characterization, modeling and enhancement of novel hybrid salinity gradient driven electrokinetic energy conversion

Jiao, Yanmei

2015

Jiao, Y. (2015). Characterization, modeling and enhancement of novel hybrid salinity gradient driven electrokinetic energy conversion. Doctoral thesis, Nanyang Technological University, Singapore.

https://hdl.handle.net/10356/62150

https://doi.org/10.32657/10356/62150

NANYANG TECHNOLOGICAL UNIVERSITY

Characterization, Modeling and Enhancement of Novel Hybrid Salinity Gradient Driven Electrokinetic Energy Conversion

JIAO YANMEI

SCHOOL OF MECHANICAL AND AEROSPACE ENGINEERING

2014

Characterization, Modeling and Enhancement of Novel Hybrid Salinity Gradient Driven Electrokinetic Energy Conversion

BY

JIAO YANMEI

Thesis Submitted to Nanyang Technological University

in Partial Fulfillment of the Requirements for the Degree of Doctor of Philosophy

School of Mechanical and Aerospace Engineering

2014

Abstract

This thesis reports a study of recently proposed novel hybrid energy conversion technique using a combined principle of electrokinetic (EK) and forward osmosis (FO). The proposed FO-EK energy conversion technique has been demonstrated by using a stack system comprising two submodules, a FO submodule and an EK submodule. Under a salinity gradient, a suction force is created to induce a hydrodynamic flow in the FO submodule based on the principle of FO. Accordingly, electric energy, in forms of EK streaming potential and/or streaming current, is generated across a porous glass housed in the EK submodule. This proposed power generation technique converts the salinity gradient energy into the electric energy without need of external pressure input.

Firstly, two kinds of mathematical models, namely a uniform-capillary model and a heterogeneous-capillary model, are presented to characterize and assess the performance of the proposed FO-EK energy conversion technique. Meanwhile, thorough experiments are carried out to investigate the processes and performance of the FO-EK energy conversion technique and to validate the theoretical models. Results show that, compared to the uniform-capillary model, the heterogeneous-capillary model yields better agreement with the experimental data. In addition, the generated power density decays with increasing the pore size of the porous glass and monotonically increases with increasing the salinity difference between the draw solution (DS) and the feed solution (FS). It is also demonstrated that a maximum power density of 0.165 W m^{-3} can be achieved by using the porous glass with an average pore size 6 μm at 4 M salinity difference.

However, concentration polarization (CP) happened in both FO and EK submodules greatly reduces the energy conversion performance of the hybrid FO-EK system. Consequently, another two studies on the CP are successively conducted specifically on the FO process and the EK process. On the one hand, a series of experimental study based on a micro-FO-device is carried out to visualize and quantify the external concentration polarization (ECP) phenomenon in FO process. Meanwhile, a steady-state 2D numerical model is also developed to interpret experimental results. Research mainly focuses on effects of tangential flow rate on the FO flow rate, the FO efficiency, the thickness of ECP layer and the osmotic pressure distribution within the ECP layer. On the other hand, a numerical analysis is conducted to study the effects of ion concentration polarization (IonCP) on the energy conversion performance of the pressure-driven EK flow through a capillary system. The numerical study not only analyses the inner characteristics of the capillary system, including distributions of the induced potentials, the ion species and the electric conductivities, but also examines the terminal characteristics, including the overall electric resistances, the streaming potentials (i.e., open-circuit potentials), the maximum streaming currents as well as the current-potential curves. Furthermore, the relationships between the inner and the terminal characteristics of the capillary system are also fully investigated through analyzing the IonCPs happened during pressure-driven EK energy conversion process in the capillary system.

Finally, based on the two separated studies on the CPs in FO and EK processes mentioned above, another two experimental studies are carried out to enhance the energy conversion efficiency of the hybrid FO-EK system, in particular, the experiment of continuous flow mode and the experiment of surface treatment to the porous glass with

an average pore size 6 μm. Results show that, for the continuous flow mode, the optimum operation tangential flow rate happens at the region from 30 ml min^{-1} to 50 ml min^{-1} and the maximum increment, compared to that of the initially applied stack mode, reaches up to as much as 9.6 times higher for the DS concentration of 0.5 M and tangential flow rate of 40 ml min^{-1}. For the surface treatment, both the ultrasonic treatment and the SDS surfactant treatment to the porous glass can significantly improve the energy conversion performance of the pressure-driven EK flow. Compared to the porous glass without any surface treatment, the porous glass treated by ultrasonic and SDS 12 mM yields the best energy conversion performance with the maximum power density of 3.08 W m^{-3} and the corresponding increment of 27.3%.

Acknowledgements

This work would not have been possibly accomplished without the help of many people. Foremost, I would like to express my deepest gratitude to my advisors, Dr. Yang Chun, Charles and Dr. Kang Yuejun for their excellent and continuous guidance on my Ph.D study and research, for their patience, motivation, enthusiasm, and immense knowledge. It has been a great honor and pleasure to work with them during the past four years.

In addition, I would like to thank all technicians in Energy Systems Laboratory and Thermal and Fluids Research Laboratory, Mr. Lee Keng Yuen, Mr. Yeo Boon Chuan, Edward, Mr. Ang Koon Teck, Lawrence, Mr. Yap Pow Khim, Eric and Mr. Yuan Kee Hock, for their continuous assistance in lab issues including purchasing all experimental items and building experiment setup. Specifically, I would like to thank my group members: Dr. Lewpiriyawong Nuttawut, Dr. Zhao Cunlu, Dr. Ge Zhengwei, Dr. Liang Qian, Mr. Hon Kar Cherng Louis, Mr. He Jinhua, Ms. Zhou Yi, Mr. Yan Zhibin, Mr. Zhao Yugang, Mr. Phan Dinh Tuan and Mr. Dhiman Das for all the discussions with them, which facilitates the completion of this work.

Furthermore, I would extend my gratitude to Nanyang Technological University for offering me the Ph.D. scholarship and providing me with the fantastic research environment.

Last but not the least, I am immensely indebted to my mother Zhang Qingyun, father Jiao Kaisheng and younger sister Jiao Yanhua. Without their incessant love, encouragement and support, I could not have reached where I am now.

Contents

List of figures

List of tables

Chapter 1: Introduction

1.1 Background and motivation

The need for alternative environmental friendly 'green energy' sources, such as wind, solar, geothermal, biomass, ocean thermal, wave and tidal, has long been a hot issue and becomes even urgent nowadays due to more and more serious global energy and environmental problems. Salinity gradient energy harvesting at the river mouth is completely renewable and sustainable [1, 2]. Increasing attentions and efforts have been paid on the power generation from such salinity gradient energy recently [3-6].

During the past decade, two emerging membrane-based energy conversion techniques, pressure retarded osmosis (PRO) and reverse electro-dialysis (RED), have been developed to harvest the renewable energy from the salinity gradient. In PRO, a dilute solution is separated from a concentrated solution by a semipermeable membrane such that an osmotic pressure gradient is created. Driven by such osmotic pressure gradient, water migrates from the dilute solution region to the concentrated solution region through the membrane, leading to an increase of the hydrostatic pressure of the concentrated region. Power is then generated via a water turbine which is driven by the pressure-driven flow of concentrated solution [7, 8]. However, the PRO technology possesses numerous problems, such as the need of ruggedized membranes to withstand high hydraulic pressure generated in the system [3], more severe membrane fouling issues, and sophisticated peripheral equipment due to the high pressure environment. In RED, specific membranes, i.e., the cation-exchange membranes and the anion-exchange

membranes, are alternately utilized to selectively separate cations and anions from the bulk solutions. The driving force is the concentration difference between the two solutions on both sides of the membranes where an electrochemical potential gradient is generated. This membrane 'stack' terminates with electrodes at each end to convert the ionic flux into an electric current through the oxidation-reduction reactions. However, the power generation efficiency of RED is greatly affected by the shadow effect with up to 40% decrease [9]. Also, an external source of energy is required to pump salt solutions through the RED device. Nonetheless, the aforementioned issues pose limitations of the PRO and RED techniques.

In addition, several other novel techniques were also developed to harvest salinity gradient energy. Brogioli proposed a technique based on capacitance characteristics of the electric double layer (EDL) of porous carbon electrodes in solutions with different concentrations, and the technique is usually abbreviated as CDLE [10]. Sales et al. made improvement on CDLE to increase the energy conversion efficiency. In their study, anion/cation-exchange membranes are introduced to the CDLE system, which may be treated as a combination of RED and CDLE [4]. Also, a mixing entropy battery was proposed by La Mantia et al. to extract energy from the concentration difference of two solutions and store as chemical energy inside the bulk crystal structure of electrodes. This kind of battery stores charges through the chemical bonds of the electrode rather than the capacitance of the EDL of the electrode in CDLE [11]. A desalination battery was reported, which may be considered as a reversed operating process of the mixing entropy battery [12].

Different from those energy conversion techniques, Yang's group recently developed a novel hybrid energy conversion system to extract energy from the salinity gradient, termed as the forward osmosis (FO) - electrokinetic (EK) energy conversion system [13, 14]. Two submodules are included in this system, namely a FO submodule and an EK submodule. For the overall system, a suction force generated in the FO submodule due to the mechanism of FO draws water to flow through a porous glass disk which is housed in the EK submodule. When such osmotic pressure-driven flow passes across the porous glass, streaming potential and streaming current are generated and they can be harvested as the power source to an external electric circuit. This hybrid energy conversion technique could be more advantageous over the other electric energy conversion techniques, such as the PRO and the EK mentioned above. This is due to the following facts that: on the one hand, compared to the PRO systems, the proposed system operates in low pressure environment, especially in the FO submodule, thus has much lower requirement on FO membrane and also much less membrane scaling and fouling problems. Therefore, it is more cost effective. On the other hand, unlike the other pressure-driven EK systems where external pump is needed to provide the pressure-driven flow, the system is directly driven by the salinity gradient energy to generate electricity without need of any extra energy input like pumping power.

1.2 Objective and scopes

With proposing such a novel hybrid energy conversion technique, the main objective of this work is to characterize and improve the novel FO-EK energy conversion system

through carrying out theoretical, numerical and experimental studies. To accomplish this objective, the main scopes are specified as follows:

1. To develop a theoretical model and conduct corresponding experimental investigations on the energy conversion performance of the stack FO-EK system;
2. To separately study the effects of concentration polarization (CP) phenomena specifically happened in FO process and EK process, which always reduce the overall energy conversion efficiency of the FO-EK system, on the corresponding submodule performance; and
3. To improve the FO-EK system, based on results and conclusions from studying the CP phenomena mentioned above, to enhance the energy conversion performance.

1.3 Outline of the thesis

This work mainly consists of seven chapters, covering both fundamental investigations and further improvement to the novel hybrid FO-EK energy conversion technique driven by salinity gradient. Brief introduction to each chapter is given as follows:

Chapter 1 introduces emerging energy conversion techniques driven by salinity gradients and provides the motivation of this study, followed by the objective and scopes of this research work.

Chapter 2 presents a thorough literature review on basic principles and development as well as drawbacks of the EK and the FO technologies. Meanwhile, a brief summary and comments on the literature review are provided.

Chapter 3 reports comprehensive theoretical and experimental studies to assess and characterize the performance of the stack FO-EK energy conversion system. Particularly, two kinds of mathematical models, namely a uniform-capillary model and a heterogeneous-capillary model, are proposed to give mathematical description on the energy conversion process of the proposed FO-EK system. Meanwhile, thorough experiments are also carried out to investigate the process and performance of the FO-EK energy conversion system and to validate the theoretical study. All studies in this chapter mainly focus on the effects of the salinity gradients on the FO-EK system performance, including the FO flux, the flow rate, the pressure drop, the generated streaming potential, the generated maximum streaming current and the output power density.

Chapter 4 presents an experimental study based on a micro-FO-device to visualize and quantify the external concentration polarization (ECP) phenomenon in FO process. Meanwhile, a steady-state 2D numerical simulation based on finite element method (FEM) is also conducted to interpret experimental results. Research works mainly focus on the effects of tangential flow rate on the FO flow rate, the FO efficiency, the thickness of ECP layer and the osmotic pressure distribution within the ECP layer.

Chapter 5 presents a dimensionless numerical study to characterize the effect of ion concentration polarization (IonCP) on the performance of the energy conversion process of the pressure-driven EK flow in a capillary system. The study in this section not only analyses the inner characteristics (including distributions of the induced potentials, the ion species and the electric conductivities) and the terminal characteristics (including the overall electric resistances, the streaming potentials (i.e., open-circuit potentials), the maximum streaming currents as well as the current-potential curves) of the capillary

system, but also fully explores the relationships between the inner and the terminal characteristics through analyzing the IonCPs happened during pressure-driven EK energy conversion process in the capillary system.

Chapter 6, based on the two separated studies on the CPs in FO and EK processes respectively conducted in Chapter 4 and Chapter 5, demonstrates another two experimental studies for enhancing the energy conversion efficiency of the proposed hybrid FO-EK system, namely the experiment of continuous flow mode and the experiment of surface treatment to the porous glass.

Chapter 7 provides a summary of contributions of this research work and also suggests possible and promising works for future studies.

Chapter 2: Literature review

2.1 Electrokinetic (EK) phenomena

2.1.1 Basic principle of EK phenomena in micro/nano-channels

It is well known that majority of substances can be charged immediately once being immersed in an aqueous medium through electrochemical mechanisms of adsorption of the charged species and/or dissociation of the ionizable groups [15, 16]. For example, a glass capillary usually gets negatively charged when in contact with electrolyte solution under suitable solution pH due to the dissociation of silanol groups, $SiOH \leftrightarrow SiO^{-} + H^{+}$ [17]. The negatively charged surface attracts positive ions and repels negative ions, leading to the formation of an electric double layer (EDL). A widely accepted description of the EDL is the Stern model, in which the electric layer in aqueous solution is characterized into two distinct parts: an immobile inner layer (Stern layer) dominated by the electrostatic force and a mobile outer layer (diffusion layer) dominated by the thermal Brownian motion [18]. As shown in Figure 2.1, the centers of any ions attached to the charged surface, i.e., ions in the Stern layer, comprise the Stern plane. Ions whose centers are located beyond the Stern plane form the diffuse mobile part of the EDL. The plane, consisting of the centers of the ions of about one or two radii away from the surface, is defined as the shear plane, where the no-slip fluid flow boundary condition is assumed to

apply. The potential at the shear plane is referred to as zeta potential, ζ, which is slightly different in magnitude from the Stern potential ψ_d [19].

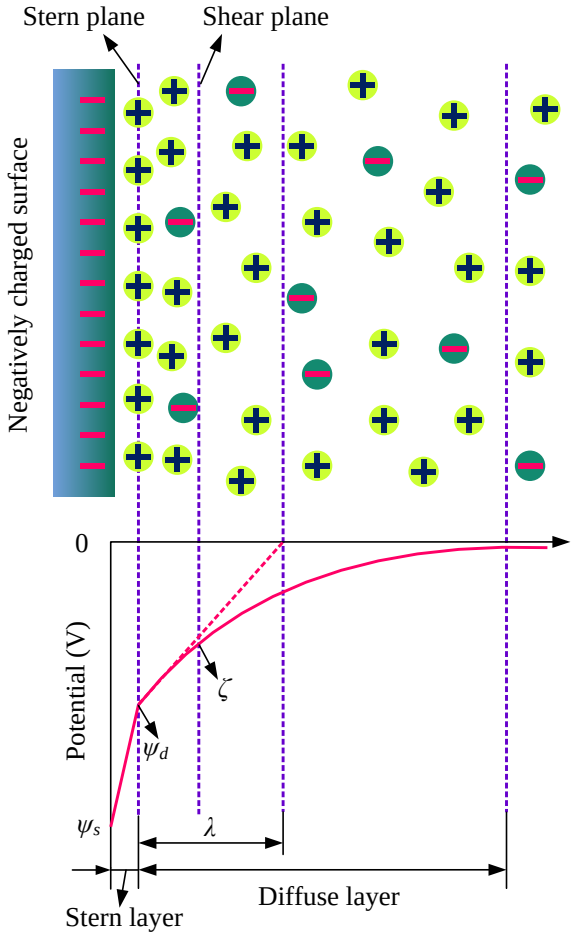

Figure 2.1 Schematic of electric double layer (EDL) of a negatively charged surface according to the Stern model. It shows the electric potential profile, Debye length λ and the overall extent of EDL [19].

The thickness of the EDL, characterized by the Debye length λ, is estimated by considering a balance of electric potential energy and thermal energy [20] which is given as:

$$\lambda = \left(\frac{\varepsilon_0 \varepsilon_r k_B T}{\sum e^2 z_k^2 n_{k,\infty}} \right)^{1/2} = \left(\frac{\varepsilon_0 \varepsilon_r RT}{\sum \tilde{F}^2 z_k^2 C_{k,\infty}} \right)^{1/2} \quad (2.1)$$

Typically, the Debye length represents a characteristic distance from the Stern plane to a plane where the electric potential decays to approximately 33% of the surface potential [19]. A log-log plot of EDL thickness for (1:1) symmetric electrolyte solution, such as NaCl or KCl solution with $|z_k| = 1$, based on the Eq. (2.1), is shown in Figure 2.2.

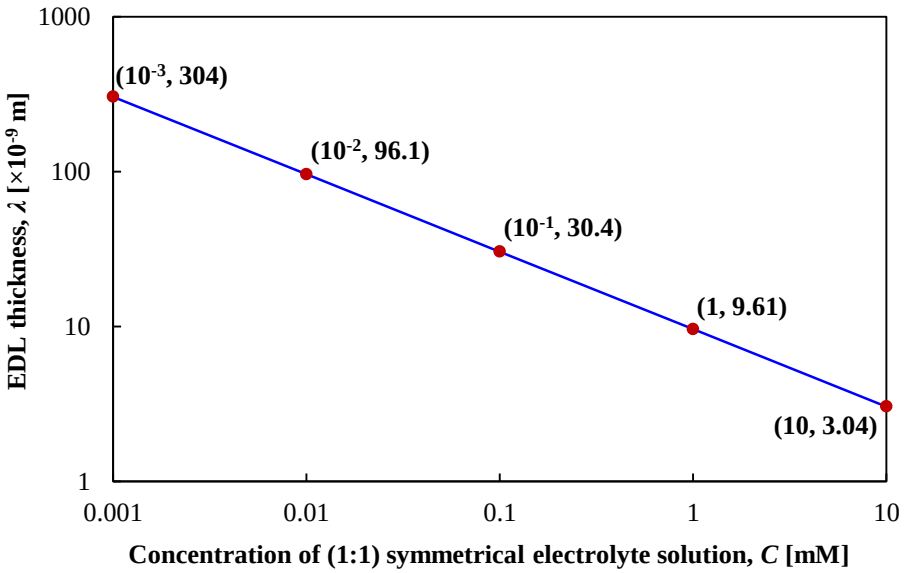

Figure 2.2 Log-log plot of electric double layer (EDL) thickness for (1:1) symmetric electrolyte solution with certain concentrations [20].

The term electrokinetics is associated with the relative motion between two phases, solid and liquid, with a charged interface. Generally speaking, electrokinetic (EK) phenomena are the consequences of the interaction between the EDL and certain applied fields, such as electric field, pressure field, gravitational field or centrifugal field. EK techniques provide some of the most popular small-scale nonmechanical strategies for

manipulating particles and fluids. The most commonly encountered four types of EK phenomena are electroosmosis, streaming potential, electrophoresis and sedimentation potential.

Electroosmosis, as shown in Figure 2.3, is referred to as the induced motion of liquid driven by applied electric field across a stationary charged capillary tube, porous medium or membrane. For example, when a negatively charged micro/nano-channel is subjected to an applied electric field, the excess cations in EDL, gaining movement due to the Coulomb force, drag the liquid molecules towards the cathode terminal. Electroosmosis can be utilized as a pumping mechanism to drive liquid across porous media, capillaries and micro/nano-channels [21-24].

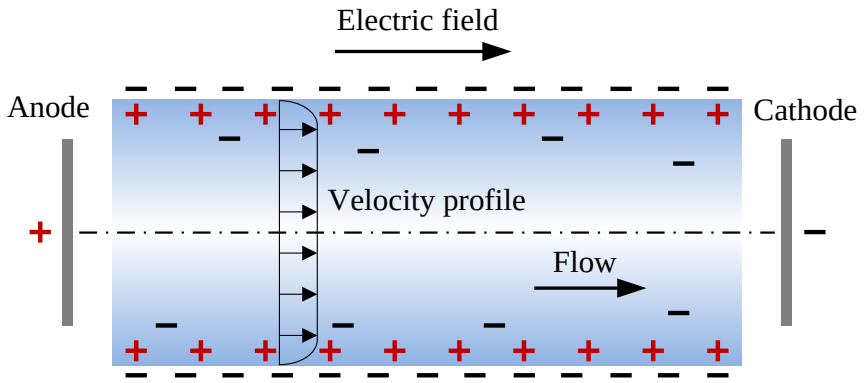

Figure 2.3 Electroosmosis in a surface charged capillary [19].

Streaming potential, Figure 2.4, is considered as an opposite phenomenon of electroosmosis. When an aqueous solution is driven by a pressure gradient to pass through a micro/nano-channel, counterions in the EDL due to the channel surface charges also flow to the downstream end, giving rise to convection current or streaming current. However, as there is no external electric circuit between the inlet and outlet of the

micro/nano-channel, the accumulation of the excess counterions at the outlet generates a potential difference between the two ends of the micro/nano-channel which simultaneously induces a backward conduction current through the bulk of the liquid. The induced potential difference is the so-called streaming potential. At steady state, the net current is zero whereby the streaming current and conduction current sum up to zero. When the micro/nano-channel is connected with an external circuit, the generated streaming potential and streaming current can be harvested as the power source. Obviously, such EK process directly converts the hydrodynamic energy into the electric energy. Practically, the phenomenon of streaming potential/current can also be employed to determine the zeta potential ζ of a charged solid surface [25].

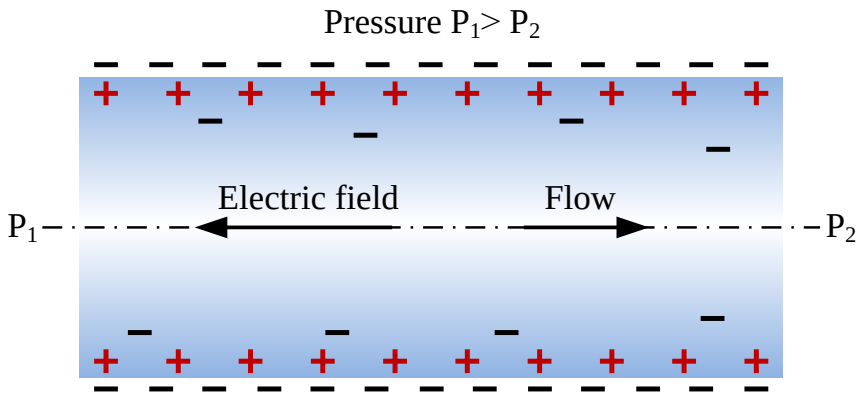

Figure 2.4 A pressure-driven flow through a surface charged capillary [19].

Electrophoresis, as shown in Figure 2.5, is the motion of the charged surface, such as ions, molecules and particles, relative to a stationary liquid [26]. When a charged particle is placed in a stationary aqueous solution, the counterions relative to the surface charges of the particle are attracted and the coions are rejected, generating an EDL around the charged particle. Overall, the region consisting of the charged particle and the

surrounding ionic cloud appears to be neutral. If the charged particle is subjected to an electric field, it will move due to the Coulomb force along the electric field. However, the surrounding mobile counterions and coions in the EDL slightly move in the opposite direction but still around the charged particle. At the steady state, the forward Coulomb force on the charged particle and the backward viscous force due to the stationary aqueous solution are finally balanced. Such EK phenomenon can also be used as an approach to measure the surface potential of a charged particle [19].

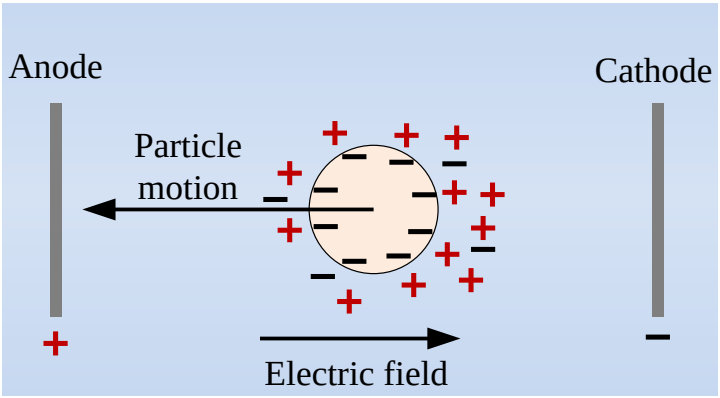

Figure 2.5 Electrophoresis of a surface charged particle under an externally applied electric field [19].

Sedimentation potential, as shown in Figure 2.6, is referred to as the motion of charged particles relative to the stationary liquid driven by the gravitational or centrifugal field. The motion of a dispersed charged particle disrupts the equilibrium symmetry structure of EDL. The relatively backward viscous flow around the particle drags counterions and coions in the diffuse layer of the EDL away from the particle, which results in slight displacement in a relative position between the charged particle and the surrounding EDL. Then the region occupied by the charged particle and the counterions

in EDL becomes polarized with one end dominated by the surface charges of the particle and the other end dominated by the couterions. Consequently, an electric field, usually defined as the sedimentation potential gradient, is finally generated from this process.

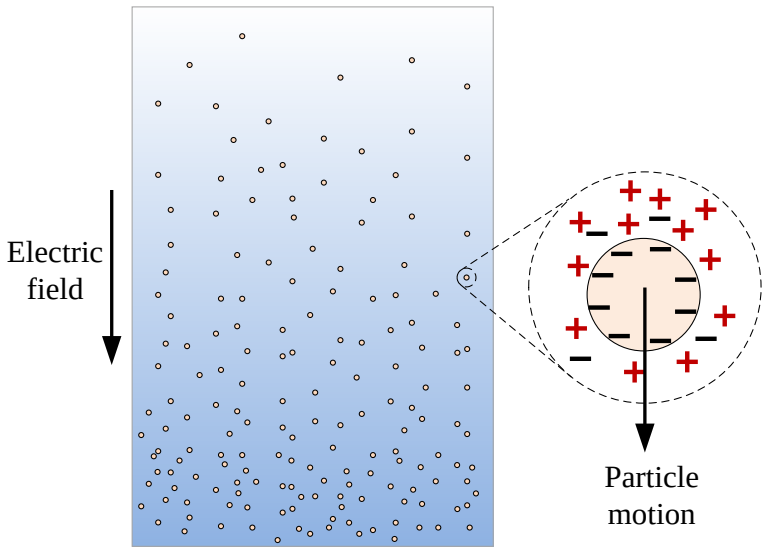

Figure 2.6 Sedimentation potential induced by the motion of charged particles [19].

It is evident that, among the four types of EK phenomena, streaming potential and sedimentation potential are the processes of converting the kinetic energy into electric energy, and electroosmosis and electrophoresis are completely opposite processes.

2.1.2 Development of the streaming potential/current

Recently, power generation based on pressure-driven EK flow has attracted increasing attentions [27-29], especially with the introduction of liquid slip in micro/nano-channels [30]. For the performance of such EK batteries, high energy conversion efficiency and high output power are two critical factors. To achieve better

design and process control, great efforts have been put on developing more accurate theoretical models for the flow-induced streaming potential.

The mathematical models of the streaming potential and the streaming current include two main governing equations, namely the Poisson-Boltzmann (P-B) equation for describing electrical potential profile in the EDL and the Navier-Stokes (N-S) equation for describing the fluid flow field [31]. Meanwhile, the Nernst-Planck (N-P) equation is employed to describe the ion transport in micro/nano-channels. Chang and Yang [32] provided a good review on the microfluidic-based batteries with their conversion efficiencies ranging from 0.01% to 15%. According to the analyses of previous works, it is concluded that the energy conversion efficiency increases with decreasing mobility of the monovalent counterions in the aqueous solution because ionic conductance can cause power dissipation [32, 33]. In this work, the methods and results of the electrochemomechanical energy conversion reported in recent studies are summarized in Table 2.1. This table also includes boundary conditions and some crucial property parameters. It should be pointed out that the electric boundary condition to the P-B equation is either constant zeta potential or constant surface charge density. However, Wang and Kang proved that neither of these two boundary conditions was accurate in modeling the streaming potential process, and they suggested that the electric boundary condition should be determined by a local chemical equilibrium on the solid-liquid interface [31].

Table 2.1 Review on the methods and results of the electrochemomechanical energy conversion in precious works.

Researcher	Channel Parameters				Solution Propoties								Applied Pressure	P_{power}	$P_{effieciency}$	Hydrodynamic Boundary Condition
	Size	$-\zeta$	$-\sigma_s$	δ_s	Electrolyte	C	ρ_f	D	T	ε_r	η	δ				
Yang and Li, 1998 [34]	l=1cm; w=30μm; h=20μm (3D)	25, 50, 75	/	/	KCl	10^{-4}	/	/	298	80	0.9×10^{-3}	/	$0 \le \bar{p} = \frac{p-p_0}{\rho_f U} \le 2000$	/	/	No-slip
Yang et al., 2003 [28]	d=16mm; t=3mm; (glass porous disk) p_{por}=0.3(average pore radius 13μm)	50~200	/	10^{-8} or 10^{-9}	Pure water	/	10^3	0.9×10^{-6}	/	80	/	5×10^{-5}	$-dp/dx=9.8\times10^5$ Pa m^{-1}	~μW cm^{-3}	/	No-slip
Kwok and Yang, 2003 [35]	h=40μm;	100	/	/	KCl	Infinite dilute	/	2×10^{-9}	/	/	/	/	$-dp/dx=10^6$ Pa m^{-1}	/	/	Slip with b=1μm
Daiguji, 2004 [36]	l=5μm; h=30nm; 1×1μm^2 (reservoirs)	/	0 ~ 5	/	KCl	10^{-2} ~ 10	10^3	$D^+=1.96\times10^{-9}$ $D^-=2.03\times10^{-9}$	300	80	10^{-3}	/	$-dp/dx=10^{11}$ Pa m^{-1}	9.28μW m^{-1}	8.25	No-slip
Olthuis et al., 2005 [37]	Sintered porous glass plug; p_{por}=5 (nominal d_{pore} of 1.0-1.6μm); d=60mm; t=3.5mm	/	/	/	KCl (pH:10)	1 or 10^2	/	/	/	/	/	/	0.03 atm (outlet) (by water jet pump)	20nW	/	Exp.
Chun et al., 2005 [38]	d=5μm; l=10^{-2}m	Ψ_s=1 or 3	/	5×10^{-9}~1×10^{-7}	(1:1) solute	10^{-3} ~ 10	/	mobility (D_i/R/T)	298	80	10^{-3}	/	Δp=10bar	>1μW cm^{-3}	/	No-slip
van der Heyden et al., 2005 [39]	l=4.5mm; w=50μm; h=70~1147nm 1.5×1.5mm^2 (reservoirs)	60	4	/	KCl (pH:8)	5.6×10^{-3}~1×10^3	/	/	/	/	/	/	Δp=4bar	/	6	Exp. No-slip
Daiguji et al., 2006 [29]	l=5μm; h=5~100nm; 1×1μm^2 (reservoirs)	/	1~40	/	KCl	10^{-2} ~ 10	10^3	$D^+=1.96\times10^{-9}$ $D^-=2.03\times10^{-9}$	300	80	10^{-3}	/	p_L=0MPa p_R=0.5MPa	/	5.8	No-slip
Mirbozorgi et al., 2007 [40]	h=2μm; l=20μm (2D)	25~300	/	/	KCl	10^{-2}	10^3	$D^+=D^-=2\times10^{-9}$	298	78.5	10^{-3}	/	2×10^4Pa	/	/	No-slip
van der Heyden et al., 2007 [41]	l=4.5mm; w=50μm; h=70~1147nm 1.5×1.5mm^2 (reservoirs)	100	8.2	/	KCl LiCl (pH:7)	10^{-2}~10^2	/	/	/	/	/	/	Δp=4bar	240pW for 490nm	3.2 for h=75nm	No-slip
Ren and Stein, 2008 [42]	h=50, 200nm; w/l=1	/	10	/	KCl	10^{-3}	/	$\mu^*_+=7.32\times10^{-8}$ $\mu^*_-=-7.6\times10^{-8}$	296.15	79	0.93×10^{-3}	/	/	/	7 for b=0 17 for b=25 37 fro b=50	Slip with b=0, 10, 50
Soong et al., 2009 [43]	l=304μm; h=6.08μm	=<200	/	/	(1:1) solute	10^{-3}	997	/	298	78.41	8.9226×10^{-4}	/	$-dp/dx=4.265\times10^4$ Pa m^{-1}	/	/	Slip
Chang and Yang, 2009 [32]	l=5μm; h=15/30nm; 2μm×2μm (reservoirs)	/	1, 3, 5, 10	/	KCl (pH:7)	1, 10^{-1}, 10^{-2}	10^3	/	298	80	10^{-3}	/	$-dp/dx=10^8$ Pa m^{-1}	/	4.78	No-slip
Wu and Wang, 2010 [44]	h=3μm	100 for glass 50 for PDMS	/	/	(1:1) solute	0.0121	10^3	/	298	78.5	0.9×10^{-3}	1.4687×10^{-4}	$-dp/dx=0.88\times10^7$ Pa m^{-1}	/	/	0 for glass 90 for PDMS
Renksizbulut et al., 2010 [45]	l=38.48μm; h=3.85μm;	75			(1:1) solute	10^{-2}	10^3	2×10^{-9}	298	78.5	10^{-3}	/	Δp=5.40 kPa	/	/	Slip

Nomenclature in this Table:

b	Slip length [nm];	P_g	Generated power or power density;	ε_r	Dielectric constant;
C	Concentration [mM];	p_{por}	Porosity;	ζ	Zeta potential [mV];
d	Diameter;	t	Thickness;	η	Energy Convert Efficient [%];
D	Diffusivity [m^2 s^{-1}];	T	Temperature [k];	μ	Dynamic viscosity [Pa s];
d_{pore}	Diameter of the pore;	w	Width;	μ^*	Mobility of ion, $(z_i e D_i)/(k_B T)$ [m^2 V^{-1} s^{-1}];
h	Height;	δ	Conductivity [S m^{-1}];	ρ_f	Fluid density [kg m^{-3}];
l	Length;	δ_s	Surface conductivity [S];	σ_s	Surface charge density [mC m^{-2}];

It was recently proposed that the slip boundary condition on hydrophobic surfaces could significantly enhance the electroosmosis performance in nanochannels [46], and this hypothesis was experimentally verified [47, 48]. It is known that there are mainly two kinds of friction in microfluidics which are resulted from interactions between the solvent and the wall and between the solute and the wall. Consequently, a low density boundary layer of water molecules occurring in the vicinity of hydrophobic surfaces [49] decreases the interaction between the water molecules and the wall. Hence water can flow over the hydrophobic wall more smoothly, giving rise to a non-zero boundary velocity.

Compared with the wetting case with non-slip boundary conditions, significant slip of the liquid in the vicinity of non-wetting solid surfaces is investigated both theoretically and experimentally [46, 50-52]. It was found that the charges within the Stern layer, usually immobile in the case of hydrophilic wetting surface, can flow over hydrophobic surfaces due to slip. As a result, the charge movement contributes to the streaming current by an even larger amount in addition to the increment of the mean velocity within the channel due to the slip velocity at the interface. At the condition of constant surface charge density, the relatively high hydrophobicity of the solid surface can enhance the EK phenomena by a slip-induced amplification factor of $(1+\kappa_{eff}b)$, where κ_{eff}^{-1} is the effective Debye length and b is slip length [47, 53]. Although such kind of boundary condition may be not as precise as the previous modeling with constant surface charge [33, 41], it shows a more qualitative understanding of the effects of liquid slip on the pressure-driven EK flow in microfluidics.

Highly hydrophobic solid surface gives rise to high liquid velocity and thus low pressure consumption. In addition, high surface charge density, obviously, induces a high zeta potential. Ideally improvements in both of these two aspects can greatly enhance the EK flow in micro/nano-channels. However, it is known that the less polarizable the solid surface molecules are, the more hydrophobic the solid surface is. This means that the solid surface hydrophobicity can be increased by diminishment of surface charge density [54], which simultaneously reduces the zeta potential. In order to improve the energy conversion performance of the pressure-driven EK flow, on the one hand, we try to enhance the slip condition of the micro/nano-channels; on the other hand, we should also try to create higher surface charge density. Some approaches have been reported to address this dilemma by adding polymers, employing surface modification or voltage biasing. In fact, there is always tradeoff when balancing strong slip and high surface charge density. Therefore, how to practically balance these two aspects to achieve better hydrodynamic and EK performance of the microfluidic system is the most challenging issue for current and future researches in this field.

2.1.3 Ion concentration polarization (IonCP)

Traditional theoretical analysis based on Onsager reciprocal relationship proposes a relationship between the induced streaming potential gradient and the applied pressure gradient, i.e., $\left(\frac{E_x}{P_x}\right)_{I=0} \simeq \frac{\varepsilon_0 \varepsilon_r \zeta}{\eta \sigma^\infty} \varpi$, where ε is the dielectric permittivity of solvent, ζ is the zeta potential of charged channel surface, η is the dynamic viscosity of the electrolyte solution, σ^∞ is the electrolyte solution conductivity expressed as $\sigma^\infty = \frac{e^2}{k_B T} \sum z_k^2 D_k n_{k\infty}$,

and ϖ is a coefficient expressed as $\left[1-\frac{\tanh(\kappa h)}{\kappa h}\right]$ for slit charged micro/nano-channel with height of 2*h* and $\left[1-\frac{I_1(\kappa a)/I_0(\kappa a)}{\kappa a}\right]$ for circular charged micro/nano-channel with radius of *a* [19]. This expression obviously indicates that, for a given charged micro/nano-channel and a given electrolyte solution with certain concentration, the induced streaming potential gradient linearly increases with increasing the applied pressure gradient. However, according to traditional theoretical studies, the EK energy conversion process is assumed only happening in the charged channel region, which, obviously, oversimplifies the real pressure-driven EK process. On the one hand, the output potential is induced by the accumulation of counterions at the down streaming end of the charged channel. This accumulation of counterions is actually a kind of ion concentration polarization (IonCP) phenomenon which is evidently not included in traditional theoretical studies of streaming potential. On the other hand, the pressure-driven EK energy conversion system is connected with an external electric load by two electrodes placed in two reservoirs quite nearby channel ends. The existing big reservoirs will also greatly influence the flow field at the entrance area of the charged capillary, inducing another IonCP zoon. Those IonCP phenomena, in turn, significantly affect the output energy to the external electric load, especially for conditions of high surface charge densities, low solution concentrations and high applied pressure gradients [55, 56]. Compared to streaming potential process, much more serious IonCP phenomena and thus significant non-linear properties induced by highly applied electric field are observed in electroosmosis process as shown in Figure 2.7 [57-66]. Therefore, most of existing IonCP studies in electrokinetic field focus on electroosmosis process. Only in

recent years, a few studies recognized that such kind of IonCP phenomena occurring in the pressure-driven EK flow process diminishes the generated power and the energy conversion efficiency [29, 36, 55, 67, 68].

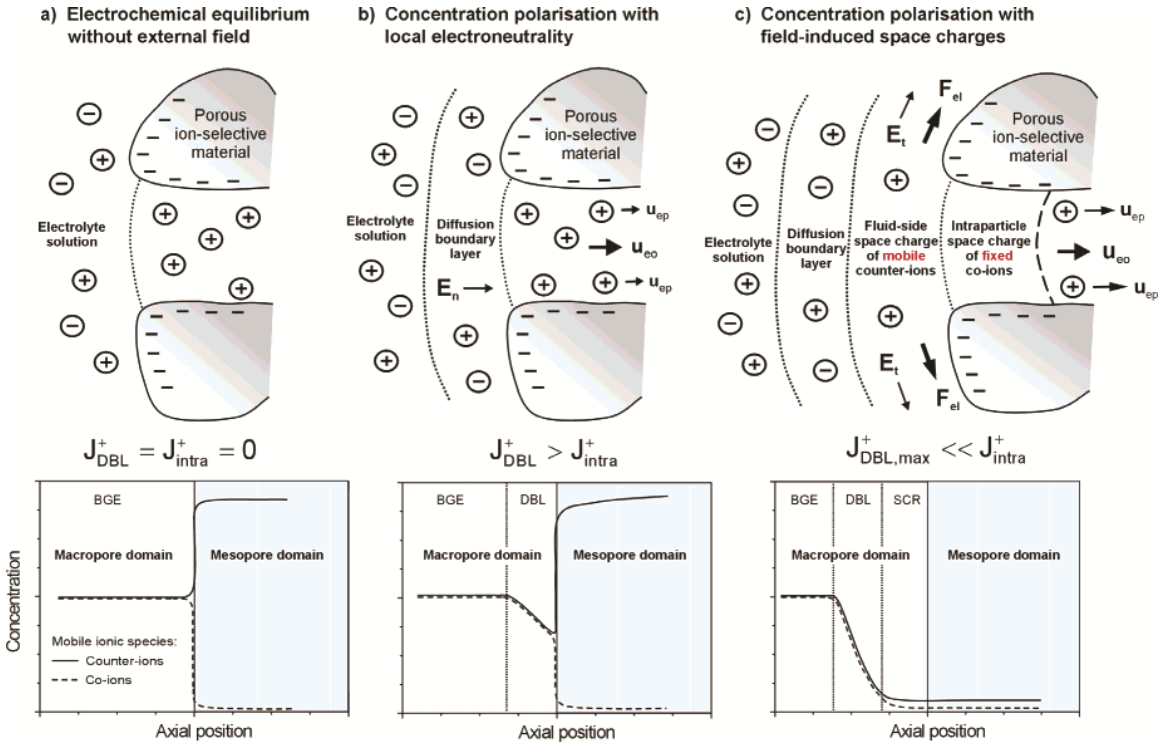

Figure 2.7 Schematics of ion concentration polarization (IonCP) phenomena at the macropore-mesopore junction happened in electroosmosis process and the corresponding normalized ion concentration profiles. Figure a, concentration distributions of ion species at Donnan equilibrium in the absence of external electric field. Figure b, when an electric field is applied, the counterions pass through the negatively charged mesopores, inducing a salt depletion layer, i.e., convection-diffusion layer, nearby the inlet of the mesopore. Figure c, when a stronger electric field is applied, the concentration of ion species at the macropore-mesopore junction are further depleted, generating a fluid-side space charge region and also the second-kind electroosmosis around the macropore-mesopore junction [69].

2.2 Forward osmosis (FO) phenomenon

2.2.1 Basic principle of forward osmosis (FO) phenomenon

The spontaneous transport of water molecules between two solutions with different concentration separated by a semipermeable membrane, being permeable to small water molecules but impermeable to large solute molecules, is widely used in fields of generating fresh water or concentrating salts. The driving force is the chemical potential difference of aqueous solutions, i.e., the osmotic pressure difference. Strathmann provided a detailed derivation for the osmotic pressure of a solution based on the theory of chemical potential equilibrium. According to his analysis, two main assumptions are made: the solution with single component solute is separated from the pure solvent by a strictly semipermeable membrane, and the osmotic system is in equilibrium state. For a solution with molar concentration *c*, the osmotic pressure π is given as:

$$\pi = -\chi RT\left(\nu_c + \nu_a\right)c \tag{2.2}$$

where χ is the osmotic coefficient, ν is the stoichiometric number, and the subscripts '*a*' and '*c*' represent anion and cation, respectively [70].

The performance of osmotic process is mainly determined by properties of semipermeable membrane, including the permeability of solvent and the rejection of solute. In addition, Figure 2.8 illustrates all the other parameters related with osmosis process, which should be considered in calculating the overall solvent permeating flux across the membrane. Based on all parameters shown in this figure, four classical osmosis-related status and their corresponding constrains are elaborated in Table 2.2.

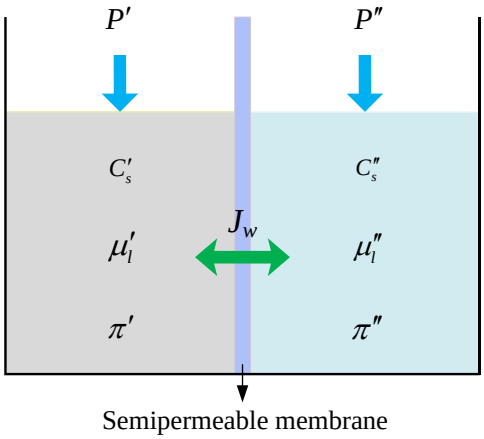

Figure 2.8 Schematic illustration of osmosis process. Two solutions with different concentration are separated by a semipermeable membrane. The subscripts '*l*' and '*s*' represent solvent and solute of the solutions, respectively, '*c*' and 'μ' are respectively the concentration and the chemical potential, '*P*' is the hydrostatic pressure and 'π' is the osmotic pressure, J_w is the permeating flux of solvent across the membrane.

Table 2.2 Four classical osmosis-related status and their corresponding constrains.

Osmosis status	Forward osmosis	Pressure retarded osmosis	Osmotic equilibrium	Reverse osmosis
Parameters Relations	$c_s' > c_s''$ $\mu_l' < \mu_l''$ $\lvert\pi'\rvert > \lvert\pi''\rvert$ $P' = P''$	$c_s' > c_s''$ $\mu_l' < \mu_l''$ $\lvert\pi'\rvert > \lvert\pi''\rvert$ $P' > P''$ $P'-P'' < \lvert\pi'-\pi''\rvert$	$c_s' > c_s''$ $\mu_l' = \mu_l''$ $\lvert\pi'\rvert > \lvert\pi''\rvert$ $P' > P''$ $P'-P'' = \lvert\pi'-\pi''\rvert$	$c_s' > c_s''$ $\mu_l' > \mu_l''$ $\lvert\pi'\rvert > \lvert\pi''\rvert$ $P' > P''$ $P'-P'' > \lvert\pi'-\pi''\rvert$
Flux (J_w) direction	From right to left	From right to left	No flux	From left to right

Obviously, FO is a spontaneous transport process of water molecules driven by pure osmotic pressure difference across a selective semipermeable membrane from a region of higher water chemical potential (i.e., dilute solution, also named as feed solution, FS) to a region of lower water chemical potential (i.e., concentrated solution, also named as draw solution, DS). In other words, the FO separation process directly converts the chemical potential energy into the hydrodynamic energy without need of any internal mechanical

motion. Furthermore, the significant advantages of FO technology are that it operates without need of any extra hydraulic pressure input and has higher rejection of wide range of contaminants and lower membrane fouling propensity than that in pressure retarded osmosis (PRO) separation processes [71]. Consequently, compared with PRO systems, the FO systems are considerably simple and steady and thus need relatively low operational maintenance costs.

2.2.2 Development of the forward osmosis (FO)

Due to the advantages mentioned above, the FO technology has been widely employed in many applications such as wastewater treatment, water purification, seawater/brackish water desalination, food processing, controlling drug release and dehydration of pharmaceuticals during syntheses [71, 72]. Although such technology has received intensive attentions in the past decades, it has its own limitations such as ineffective semipermeable membranes, concentration polarization (CP) and less sustainable to various pH and performance instability in long-term applications.

Hitherto, some commercially available reverse osmosis (RO) membranes as well as other membranes based on cellulose triacetate (CTA) [7, 71, 73], cellulose acetate (CA) [74-76], polybenzimidazole (PBI) [77, 78] and aromatic polyamide [79-81] have been developed for FO processes. Chung et al. also provided comparative studies of the performance of recently developed FO membranes [72]. Some of the membranes show reasonably high fluxes. Even so, great efforts should be continuously put on solving problems such as salt leakage, CP and membrane instability, so that the FO technology could get more and more wide, effective and economical applications.

2.2.3 Concentration polarization (CP)

For FO devices, FS and DS are separately located at the two sides of the semipermeable membrane which only allows the permeating of small solvent molecules and stops the permeating of big solute molecules. Once the FO process starts, the solvent molecules diffuse freely from the FS side to the DS side while the solute molecules are retarded by the semipermeable membrane. Then the solute molecules within the aqueous layers adjacent to the membrane surfaces become depleted at the DS side and enriched at the FS side. This diluting or concentrating phenomenon of solution in the vicinity of the semipermeable membrane is the so-called concentration polarization (CP).

In current practical applications, almost all membranes industrially utilized in membrane processes possess the asymmetric structure which is composed of a dense selective layer (DSL) mechanically supported by thick layers of porous polymer and fabric woven, i.e., porous support layer (PSL). The small solvent molecules can freely migrate through the PSL and the DSL while the big solute molecules can only permeate through the PSL. Therefore, in addition to considering the external concentration polarization (ECP) occurring in the solution layers immediately adjacent to the membrane surfaces, the internal concentration polarization (ICP) taking place within the PSL of the asymmetric membranes should also be considered. Then the lower-than-expected water flux in FO in real applications can be reasonably explained [82].

Due to the asymmetric characteristic of semipermeable membranes, the CP classifications are usually studied together with the orientation of the membranes. Figure 2.9 shows various profiles of the solution concentration and the corresponding osmotic pressure occurring in the FO process under conditions of different membrane structures

and orientations.

Figure 2.9.a shows FO with only ECP phenomena occurring around the semipermeable membrane, i.e., concentrative ECP at the FS side and dilutive ECP at the DS side. Taking the NaCl solution as an example, the convective flow, being induced by the osmotic pressure gradient between the FS and the DS, drags the NaCl solute from the bulk to the surface of the dense selective membrane. Due to the semipermeability of the membrane, only water permeates this membrane, leaving the solute behind. This process leads to the enrichment of the solute at the FS side, especially at the region near by the membrane surface, which is known as concentrative ECP. Simultaneously, when water permeates through the dense selective membrane to the DS side, the DS in the vicinity of the membrane surface is diluted by the influent water, which is known as dilutive ECP. Both concentrative and dilutive ECP phenomena reduce the effective osmotic pressure difference and thus decrease the water flux through the membrane. Approaches, such as increasing the tangential flow velocity or introducing turbulence in the vicinity of the membrane surface, can be applied to minimize the negative effects of ECP in membrane separation processes [83].

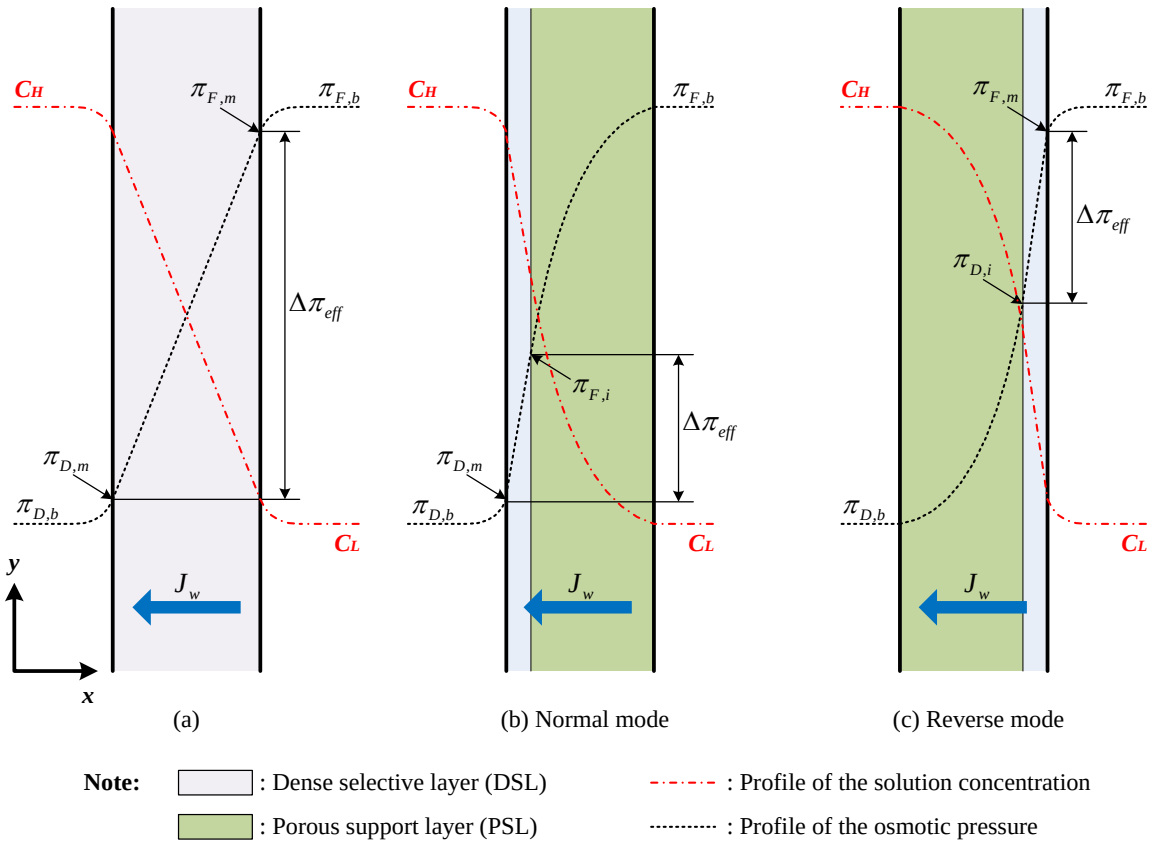

Figure 2.9 Profiles of the solution concentration and the corresponding osmotic pressure for different membrane structures and orientations. (a) A symmetric dense semipermeable membrane with only external concentration polarization (ECP) phenomena, i.e., concentrative and dilutive ECPs. (b) An asymmetric membrane with the dense selective layer (DSL) facing against the DS (Normal mode). The profile of the solution concentration illustrates concentrative internal concentration polarization (ICP) and dilutive ECP. (c) An asymmetric membrane with the porous support layer (PSL) facing against the draw solution (DS) (Reverse mode). The profile of the solution concentration illustrates dilutive ICP and concentrative ECP. Key parameters: C_H and C_L respectively represent solutions of high concentration and low concentration, $\pi_{D,b}$ is the osmotic pressure of the DS in the bulk, $\pi_{D,m}$ is the osmotic pressure in the vicinity of membrane surface at the DS side, $\pi_{F,b}$ is the osmotic pressure of the feed solution (FS) in the bulk, $\pi_{F,m}$ is the osmotic pressure in the vicinity of membrane surface at the FS side, $\pi_{F,i}$ is the effective osmotic pressure of the FS in Normal mode, $\pi_{D,i}$ is the effective osmotic pressure of the DS in Reverse mode, and $\Delta\pi_{eff}$ is the effective osmotic pressure difference. Note that it is assumed that no ECP occurs around the interface between the PSL and the solution since the solute is not reflected by this layer.

The orientation character of the asymmetric membranes gives rise to two different modes of FO, i.e., the Normal mode and the Reverse mode, as well as two additional ICP phenomena shown as Figure 2.9.b and c, respectively.

As shown in Figure 2.9.b, when the DSL of the asymmetric membrane is placed against the DS (i.e., Normal mode), water can freely pass through the PSL and then diffuse across the DSL into the DS side. Meanwhile, solutes can also enter the PSL induced by the convective flow but is blocked by the DSL, which gives rise to the enrichment of solute within the PSL of the asymmetric membrane. This phenomenon is the so-called concentrative ICP. Therefore, for FO in Normal mode, there are mainly two kinds of CPs, namely the dilutive ECP and the concentrative ICP.

On the other hand, when the DSL of the asymmetric membrane is placed against the FS (i.e., Reverse mode) as shown in Figure 2.9.c, the water permeating to the DS side dilutes the solution within the PSL of the asymmetric membrane. This phenomenon is the so-called dilutive ICP. Consequently, for FO in Reverse mode, there are mainly two kinds of CPs, namely the concentrative ECP and the dilutive ICP.

CP is the most significant but common problem occurring in the membrane-based processes due to the special operation principle and the module structure, which thus has been an intensive research topic in the past several decades [82, 84, 85]. All CP effects contribute negatively to the effective osmotic pressure difference, thus reducing the separation performance. The negative effects increase with the increased permeating flux, which is the so-called self-limiting phenomenon in the osmosis processes [86].

2.3 Summary

This chapter provides a literature review on the two related phenomena, namely EK and FO, employed in the novel energy conversion system in this study, covering the basic principles, the development in the past, and the main limitations or drawbacks. A brief summary specifically to each technique is given as below:

1. For the EK phenomena, it is a generic term representing consequences of the interaction between the EDL and some certain applied fields, such as electric field, pressure field, gravitational field or centrifugal field. Due to its specific characteristic scale and operation principle, the EK techniques are usually employed to manipulate particles and fluids in micro/nano-scale. The performance of the EK techniques is thus mainly determined by the properties of the charged solid surface and the fluid properties. Particularly to the pressure-driven EK flow, approaches such as inducing slip boundary conditions at the solid-fluid interface and/or increasing the surface charge density are always utilized to improve the energy conversion performance. However, the energy conversion efficiency of the pressure-driven EK flow is still very low due to its own thermodynamic limitation of requiring high relatively high hydrodynamic energy input. In addition, although sufficient researches have already been carried out from different aspects to study the energy conversion performance of the pressure-driven EK flow, only a few of them recognize that the IonCP phenomena occurring in the process of the pressure-driven EK flow diminish the generated electric power and the energy conversion efficiency.
2. For the FO process, it is a spontaneous transport process of water molecules driven by pure osmotic pressure difference across a semipermeable membrane from a region of

dilute solution to a region of concentrated solution. Obviously, the distinct advantage of the FO separation process is that it directly converts the salinity gradient into the hydrodynamic energy without need of any internal mechanical motion and/or extra hydraulic pressure input. Consequently, the FO systems are considerably simple and steady and thus need relatively low operating and maintenance costs. In practice, the FO technology has already been widely engaged in many applications such as wastewater treatment, water purification, seawater/brackish water desalination, food processing, controlling drug release, and so on. Although great attentions have been paid to such a promising separation technology, the FO technology still has its own limitations such as ineffective semipermeable membranes, CP negative effects, and less sustainable to various pH and performance instability in long-term applications.

This work takes advantages of the EK and the FO techniques, namely the energy conversion property of the pressure-driven EK flow and the hydrodynamic behavior of the FO process, to develop a novel hybrid FO-EK energy conversion system which converts the salinity gradient into electric energy without need of any extra energy input like pumping power. In addition to studies on the energy conversion performance of the FO-EK system, intensive studies are also conducted in this work to investigate the negative but ubiquitous effects of CP phenomena on the FO and the EK processes. Finally, strategies for improving the FO-EK energy conversion system and enhancing the energy conversion performance of the FO-EK system are consequently proposed and implemented based on the CP study results in this work.

Nomenclature

a	Channel radius [m]
b	Slip length [nm]
c	Concentration of electrolyte solution [M]
C	Concentration electrolyte solution [mol m^{-3}] or [mM]
C_k	Concentration of the ion species k [mol m^{-3}] or [mM]
D_k	Diffusivity of ion species k [m^2 s^{-1}]
e	Elementary charge [C]
E_x	Streaming potential gradient [V m^{-1}]
$\tilde{F}$	Faraday constant [C V^{-1}]
h	Half of the channel height [m]
I_0	Zero-order modified Bessel function [-]
I_1	First-order modified Bessel function [-]
J_w	Solvent flux across the membrane [m^3 s^{-1} m^{-2}]
k_B	Boltzmann constant [J K^{-1}]
P	Hydrostatic pressure [Pa]
P_x	Pressure gradient [Pa m^{-1}]
R	Universal gas constant [J K^{-1} mol^{-1}]
T	Temperature [K]
z_k	Valence of the ion species k [-]
n_k	Ionic number concentration of the ion species k [m^{-3}]

Greek symbols

ε_0	Permittivity of vacuum (free space), 8.854×10^{-12} [C m^{-1} V^{-1}]
ε_r	Relative dielectric constant [-]
ζ	Zeta potential [V]
η	Dynamic viscosity [kg m^{-1} s^{-1}] or [Pa s]
κ	Inverse of the EDL thickness [m^{-1}]
λ	EDL thickness [m]
μ	Chemical potential [J mol^{-1}]
π	Osmotic pressure [Pa]
σ^{∞}	Conductivity of electrolyte solution in the bulk [S m^{-1}] or [A V^{-1} m^{-1}]
v	Stoichiometric number [-]
χ	Osmotic coefficient [-]
ψ_d	Stern potential [V]
ψ_s	Surface potential [V]

Subscripts

a	Anion
b	Bulk solution
c	Cation
D	Draw solution
eff	Effective parameter
F	Feed solution
H	Solution of high concentration

i	Interface between the dense selective layer and the porous support layer
k	Ion species
l	Solvent
L	Solution of low concentration
m	Membrane
s	Solute
∞	Bulk solution

Chapter 3: Characterization of forward osmosis (FO) - electrokinetic (EK) energy conversion system

3.1 Introduction

As elaborated in chapter of Introduction, a novel hybrid forward osmosis (FO) - electrokinetic (EK) energy conversion technique without any requirement of external energy input is studied in this work. The FO-EK energy conversion system consists of a FO submodule and an EK submodule. To assess and characterize the performance of the proposed hybrid energy conversion technique, thorough theoretical and experimental studies are conducted in this chapter. Specifically, the research aspects include:

1. Theoretical study of the FO submodule. In this work, appropriate modifications are made based on the existing FO model [71, 86, 87];
2. Theoretical study of the EK submodule. Two theoretical models, namely uniform-capillary model and heterogeneous-capillary model, are developed to comparatively investigate the EK phenomenon through a porous medium;
3. Experimental study of the energy conversion performance of the primarily designed FO-EK stack setup;
4. Assessment and characterization of the performance of the proposed FO-EK hybrid energy conversion technique by comparing and analyzing experimental and

theoretical results, and then proposing further improvement strategies for the primarily designed FO-EK stack system.

3.2 Theory

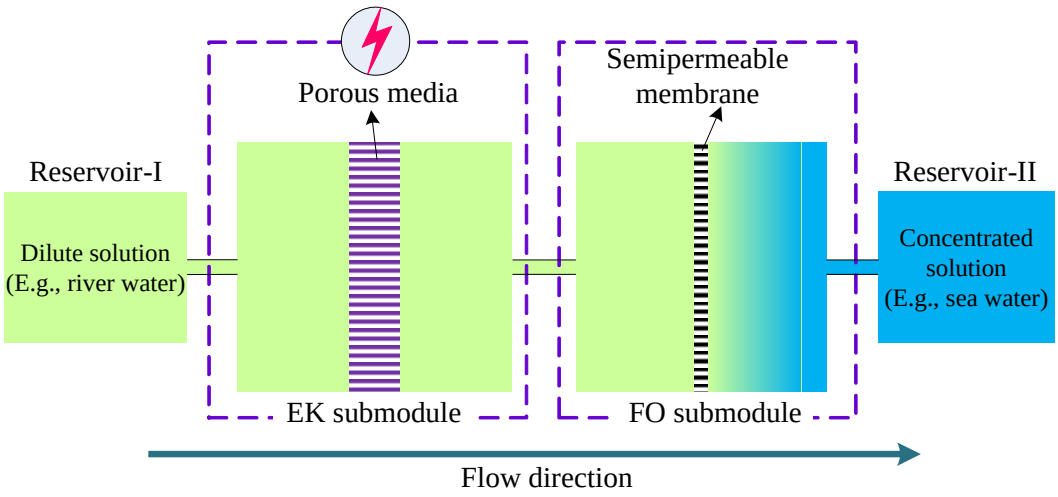

Figure 3.1 Schematic of the proposed FO-EK energy conversion system with two submodules, namely a FO submodule and an EK submodule.

Figure 3.1 shows the schematic of the proposed FO-EK energy conversion system. For such system, mathematical models for FO submodule and EK submodule will be separately developed first, and then two expressions for pressure drop and flow rate will be presented to link these two separate mathematical models together.

3.2.1 Theoretical model for FO submodule

As already discussed in chapter of Literature review, FO is a spontaneous transport process of water molecules driven by the osmotic pressure difference, which is mainly determined by the solution concentration. In this study, DI water and NaCl solution are

employed as the feed solution (FS) and the draw solution (DS), respectively. According to the tabulated values of the osmosis coefficient of NaCl solution with its concentrations ranging from 0 M to 6 M at 25˚C [88], the osmotic pressure π, in unit of Pa, can be expressed as a polynomial function of concentration c in M, i.e.:

$$\pi = a_1 \times 10^6 c + a_2 \times 10^6 c^2 \tag{3.1}$$

where a_1 and a_2 are constants, given as -4.112×10^6 Pa M^{-1} and -0.349×10^6 Pa M^{-2}, respectively. As seen from Figure 3.1, the DS in the FO submodule is continuously diluted by the solvent. Then the absolute value of the osmotic pressure of the DS decreases with the diluted concentration. Finally, the FO flux is reduced due to the diminution in the effective osmotic pressure difference between the DS and FS. Consequently, for the FO-EK energy conversion system with varying DS concentration, effective solution concentration c_{eff} should be employed to calculate the osmotic pressure instead of the initial concentration c, which is given as:

$$c_{eff} = \frac{c + c'}{2} \tag{3.2}$$

where c', an experimentally determined parameter, represents the DS concentration when the overall system is at pseudo-equilibrium state.

In this work, the FO in Normal mode as shown in Figure 2.9.b, including concentrative internal concentration polarization (ICP) and dilutive external concentration polarization (ECP), is employed in both theoretical and experimental studies. Based on the film theory [89], the model for FO flux in Normal mode is expressed as:

$$J_w = A\left[\pi_{F,b} \exp\left(\frac{J_w S}{D}\right) - \pi_{D,b} \exp\left(-\frac{J_w}{k}\right)\right] \tag{3.3}$$

where J_w is the solvent permeating flux, $m^3\ s^{-1}\ m^{-2}$; A is the solvent permeability coefficient, $m\ Pa^{-1}\ s^{-1}$; $\pi_{F,b}$ and $\pi_{D,b}$ are osmotic pressures of the FS and the DS in the bulk, respectively; S is a structure factor of PSL of the semipermeable membrane, m; D is the salt diffusion coefficient, $m^2\ s^{-1}$; k in unit of $m\ s^{-1}$ is the mass transfer coefficient expressed as $k = 0.46\mathrm{Re}^{0.36}\mathrm{Sc}^{0.36}D/d_h$ [90] (Here Re and Sc are the Reynolds number and Schmidt number, respectively; d_h is the hydraulic diameter of the cross-section of the channel.); and the overall term in bracket is defined as the effective osmotic pressure difference $\Delta\pi_{eff}$. For an infinitely dilute solution, the salt diffusion coefficient can be estimated from:

$$D = \frac{|z_c| + |z_a|}{\left(|z_c|/D_a\right) + \left(|z_a|/D_c\right)} \tag{3.4}$$

Since the hybrid energy conversion system proposed in this work operates on a batch process, the pressure drop generated along the flow direction, ΔP, should be considered. Part of the pressure drop is consumed by the EK submodule to generate electric energy and the other part is to overcome the resistance along the pipeline when liquid flows through. Then the solvent permeating flux is rewritten as:

$$J_w = A\left[\pi_{F,b}\exp\left(\frac{J_w S}{D}\right) - \pi_{D,b}\exp\left(-\frac{J_w}{k}\right) - \Delta P\right] \tag{3.5}$$

3.2.2 Theoretical model for EK submodule

When a pressure-driven flow passes across the porous glass housed in the EK submodule, excess counterions in the EDL due to the surface charges of the porous glass are induced to flow downstream, which is commonly referred as convection current or streaming current. However, as there is no external electric circuit between the inlet and

outlet of the porous glass, the accumulation of the excess counterions at the outlet generates a potential difference between the two ends, which simultaneously induces a conduction current in the opposite direction through the bulk of the liquid. The induced electric potential difference is called streaming potential [91, 92]. When the EK submodule is connected with an external circuit, the generated streaming potential and streaming current can be harvested as the power source.

3.2.2.1 EK power generation in a single capillary

Since a porous medium is equivalently treated as a bundle of parallelly packed micro/nano-channels, to model the pressure-driven EK flow through the porous glass, the pressure-driven EK flow through a micro/nano-channel as shown in Figure 3.2 should be considered first. The model development is based on the following assumptions: (1) the distance between the centerline of the channel and the shear plane of the EDL approximates to the micro/nano-channel radius a. As a result, the potential at the shear plane, i.e., the zeta potential ζ instead of the surface potential ψ_s, is employed to calculate the potential distribution; (2) the aqueous solution is assumed to be (z:z) symmetric electrolyte solution; (3) the channel aspect ratio L/a is large such that there is no ionic concentration gradient along the x-direction, i.e., $\partial n_k/\partial x = 0$ and the potential ψ due to the EDL is only a function of r, i.e., $\psi = \psi(r)$; (4) the flow in the micro/nano-channel is regarded as steady, unidirectional and fully developed; (5) the electric energy is small compared to the thermal energy, i.e., $|ze\psi| < k_BT$. As seen from Figure 3.2, the electric potential $\phi(r, x)$ at a given location (r, x) is the superposition of the potential due to the streaming potential gradient E_x and the potential due to the EDL $\psi(r)$, i.e., $\phi(r, x) = \psi(r) - xE_x$.

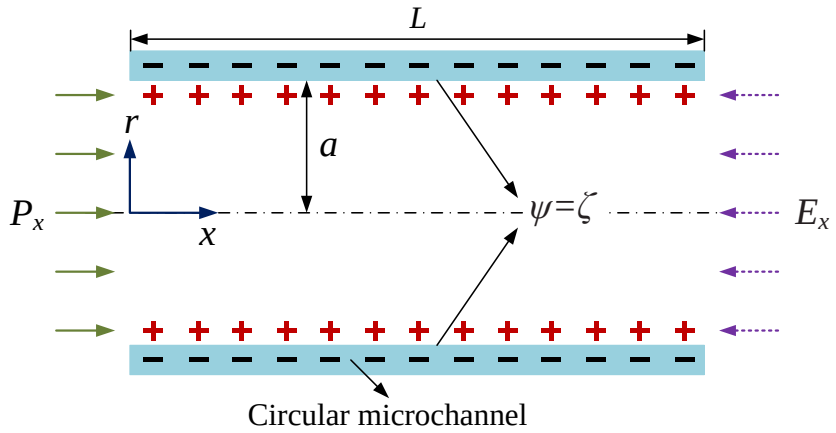

Figure 3.2 Schematic of a negatively charged straight circular micro/nano-channel. The radius and the length of the micro/nano-channel are *a* and *L*, respectively, and the zeta potential of the inner wall is *ζ*. The pressure gradient P_x and the induced electric field strength E_x along the flowing direction are defined as $P_x = -dP/dx$ and $E_x = -\partial\phi/\partial x$, respectively. The cylindrical coordinate is used in this EK system with *r* representing the radial direction and *x* denoting the axial direction.

The governing equations and corresponding boundary conditions for the pressure-driven EK flow in a negatively charged straight circular micro/nano-channel are given as follows:

Linearized Poisson-Boltzmann (P-B) equation: $$\frac{1}{r}\frac{d}{dr}\left(r\frac{d\psi}{dr}\right)=\kappa^2\sinh\left(\frac{ze\psi}{k_BT}\right) \quad (3.6)$$

Boundary conditions: $$\psi\big|_{r=a}=\zeta \quad \text{and} \quad \left.\frac{d\psi}{dr}\right|_{r=0}=0 \quad (3.7)$$

Stokes equation: $$\eta\frac{1}{r}\frac{d}{dr}\left(r\frac{du_x}{dr}\right)=-P_x+\rho_f\frac{\partial\phi}{\partial x} \quad (3.8)$$

Continuum equation: $$\frac{\partial u_x}{\partial x}=0 \quad (3.9)$$

Boundary conditions: $$u_x\big|_{r=a}=0 \quad \text{and} \quad \left.\frac{du_x}{dr}\right|_{r=0}=0 \quad (3.10)$$

where k_B is the Boltzmann constant; T is the absolute temperature; η is the fluid viscosity; ρ_f is the free charge density, expressed as $\rho_f = \sum e z_k n_k$ with subscript 'k' representing cations or anions; u_x is the velocity along x direction; κ is defined as the inverse EDL thickness expressed as $\kappa = \left(\frac{\sum e^2 z_k^2 n_{k,\infty}}{\varepsilon_0 \varepsilon_r k_B T} \right)^{1/2}$. Here, $n_{k,\infty}$ is the ionic number concentration in the neutral electrolyte; ε_0 is the permittivity of vacuum; ε_r is relative dielectric constant [34, 93-95].

The volumetric flow rate of the electrolyte solution, Q, can be obtained by:

$$Q = \int_0^a 2\pi r u_x(r) dr \tag{3.11}$$

The overall electric current along the micro/nano-channel, I, is determined by:

$$I = 2\pi \int_0^a u_x \rho_f r dr + A_c \sigma^\infty E_x F_{cc} \tag{3.12}$$

where A_c is the cross-sectional area of the micro/nano-channel, i.e., $A_c = \pi a^2$; σ^∞ is the bulk electric conductivity, expressed as $\sigma^\infty = \frac{2e^2 z^2 D n_\infty}{k_B T}$; and factor F_{cc} is expressed as $F_{cc} = 1 + \left(\frac{ze\zeta}{k_B T} \right)^2 \frac{1}{I_0^2(\kappa a)} \int_0^1 I_0^2(\kappa a \cdot R) R dR$ with I_0 being the zeroth-order of the modified Bessel function. the first term on the right-hand side of Eq. (3.12) is the convection current which is termed as the streaming current I_{str}, and the second term is the conduction current I_c. Obviously, the maximum streaming current, $I_{str,max}$, is achieved when potential difference at the two ends of the channel is zero. Combing the governing equations and the corresponding boundary conditions, one can obtain the volumetric flow rate and the electric current in non-equilibrium thermodynamics forms as:

$$I = \alpha_{11} E_x + \alpha_{12} P_x \tag{3.13}$$

$$Q = \alpha_{21} E_x + \alpha_{22} P_x \tag{3.14}$$

Here the non-equilibrium thermodynamics coefficients, α_{ij} are given by:

$$\alpha_{12} = \alpha_{21} = \Omega A_c \left(\frac{2G}{\kappa a} - 1 \right) = \frac{\varepsilon_0 \varepsilon_r \zeta A_c}{\eta} \left(\frac{2G}{\kappa a} - 1 \right) \tag{3.15}$$

$$\alpha_{11} = A_c \sigma^{\infty} F_{cc} \left[1 - \frac{\Omega^2 \eta \kappa^2}{\sigma^{\infty} F_{cc}} \left(1 - \frac{2G}{\kappa a} - G^2 \right) \right] \tag{3.16}$$

$$\alpha_{22} = \frac{a^2 A_c}{8\eta} \tag{3.17}$$

where the relationship $\alpha_{12} = \alpha_{21}$ is the so-called Onsager reciprocity relationship [96]; factors Ω and G are respectively expressed as $\Omega = \frac{\varepsilon_0 \varepsilon_r \zeta}{\eta}$ and $G = \frac{I_1(\kappa a)}{I_0(\kappa a)}$ with I_1 being the first-order of the modified Bessel function.

3.2.2.2 EK power generation in porous glass

For the theoretical study of pressure-driven EK flow in porous media, Yang et al. treated the porous media as an equivalent bundle of parallel capillaries with uniform radius, which is termed as the uniform-capillary model in this study as shown in Figure 3.3.a [28]. However, it is well known that the channel radius plays an important role in the electrokinetic streaming potential phenomenon. The energy conversion efficiency reaches maximum when the channel radius is around two times of the EDL thickness, typically in nano/submicron scale [68]. For porous media used in this study, an estimation based on hydrodynamic porous flow shows that the single equivalent pore radius reflecting the log-normal distribution is about several microns. Obviously, this approach is inaccurate in simulating the flow through the porous media with

electrokinetic streaming potential effects. Therefore, the author develop a heterogeneous-capillary model, as shown in Figure 3.3.b, by discretizing the continuous pore size distribution and obtaining multi-representative capillary radius which considers the feature of the representative radii ranging from nanoscale to microscale, making the predictions superior to the single pore size based uniform-capillary model.

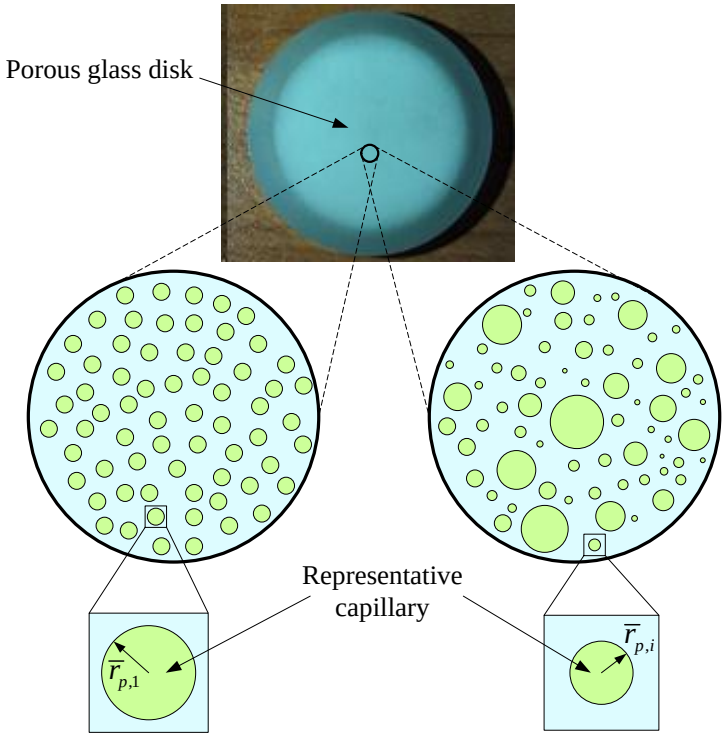

(a) Uniform-capillary model (b) Heterogeneous-capillary model

Figure 3.3 Schematic of the capillary models of porous glass in the EK submodule. a. Uniform-capillary model with uniform representative radius $\overline{r}_{p,1}$ which is the mean radius of the equivalent capillaries of the porous glass; b. Heterogeneous-capillary model with heterogeneous representative radius $\overline{r}_{p,i}$ which is the average radius for a certain range of the capillary size distribution.

Previous studies assumed that the size distribution of the equivalent capillaries of porous media follows a normal distribution [97-99]. However, the normal distribution

cannot provide a good description for the radius distribution due to its distribution range from the negative infinity to the positive infinity. Saksena and Zydney suggested the log-normal pore size probability density distribution [100], which is given as:

$$f\left(r_p\right)=\frac{1}{r_p\sqrt{2\pi b}}\exp\left\{-\frac{\left[\ln\left(r_p/\mu_p\right)+b/2\right]^2}{2b}\right\} \tag{3.18}$$

with $b=\ln[1.0+(\sigma_p/\mu_p)^2]$. The corresponding cumulative distribution function $F(r)$ based on the density distribution function is expressed as:

$$F\left(r\right)=\int_0^r f\left(r_p\right)dr_p \tag{3.19}$$

It is important to realize that, in practical situations, the range of the pore size distribution of a porous medium should be limited by a certain value rather than going to the positive infinity. Therefore, a discrete size distribution is proposed to modify the log-normal distribution, and it is illustrated in Figure 3.4.

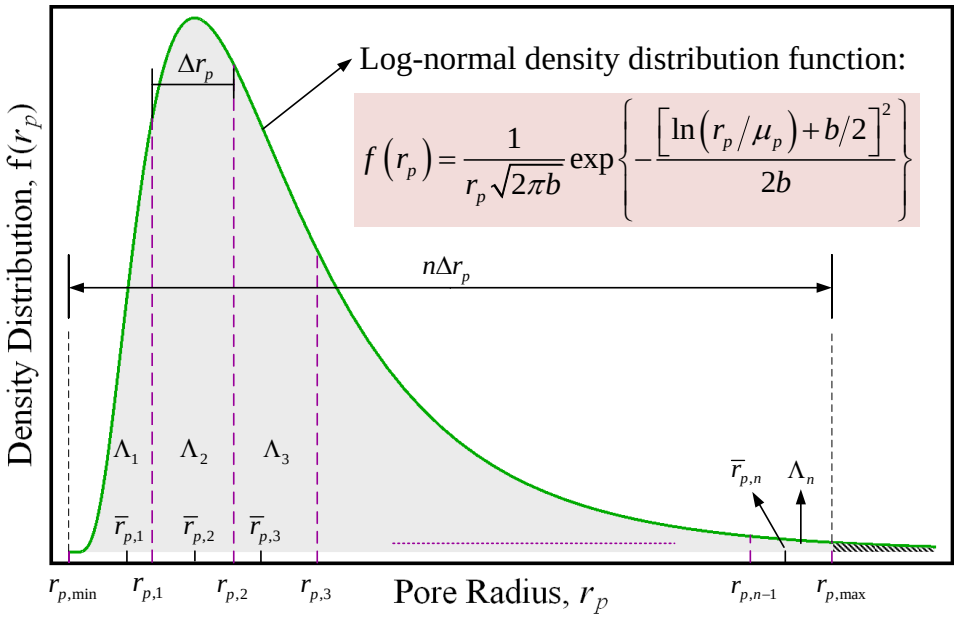

Figure 3.4 Discretization for modifying the continuous log-normal distribution $f(r_p)$. $r_{p,\max}$ and $r_{p,\min}$ are the maximum and minimum radii of the equivalent capillaries, respectively. Δr_p is the step size and n is the number of segments between the maximum and the minimum radiuses. $r_{p,i}$ is the i^{th} capillary size. $\bar{r}_{p,i}$ is the average radius for the size range from $r_{p,i-1}$ to $r_{p,i}$ and Λ_i is the cumulative probability corresponding to the average radius $\bar{r}_{p,i}$.

The corresponding mathematical discretization process of modifying the continuous log-normal distribution is given as:

$$\Delta r_p = \frac{r_{p,\max} - r_{p,\min}}{n} \tag{3.20}$$

$$\begin{aligned} r_{p,i} &= r_{p,\min} + i \cdot \Delta r_p \qquad (i = 1 \cdots n\text{-}1) \\ r_{p,i} &= r_{p,\min} \qquad (i = 0) \\ r_{p,i} &= r_{p,\max} \qquad (i = n) \end{aligned} \tag{3.21}$$

Then the average radius for a range from r_{i-1} to r_i , $\bar{r}_{p,i}$, is calculated as:

$$\bar{r}_{p,i} = \frac{\int_{r_{p,i-1}}^{r_{p,i}} r_p f(r_p) dr_p}{F(r_{p,i}) - F(r_{p,i-1})} \qquad (i = 1 \cdots n) \tag{3.22}$$

The corresponding cumulative probability to the radius $\bar{r}_{p,i}$, Λ_i, is given as:

$$\Lambda_i = \frac{F(r_{p,i}) - F(r_{p,i-1})}{F(r_{p,\max}) - F(r_{p,\min})} \tag{3.23}$$

It is assumed that the total number of the equivalent capillaries of the porous media is N. Then the number of capillaries for a certain radius range can be obtained based on the discrete log-normal distribution as:

$$N_i = N \cdot \Lambda_i \qquad (i = 1 \cdots n) \tag{3.24}$$

Two important structure parameters of the porous glass, porosity ϑ_g and tortuosity τ_g, are elaborated here. The porosity of a porous medium is defined as the ratio of the void

space to the total volume of porous medium under the assumption that all the void space is connected [101]. However, the fluid passes through a porous medium in tortuous way instead of straight way. The tortuosity is defined as the square of the ratio of the tortuous characteristic length of the pore to the apparent length. For the porous glass used in our experiment, if L_e and t_g are the effective length of the equivalent capillary of the porous glass and the thickness of the porous glass, respectively, the tortuosity can be expressed as:

$$\tau_g = \left(\frac{L_e}{t_g} \right)^2 \tag{3.25}$$

The porosity of the porous glass, ϑ_g, is given by [28]:

$$\vartheta_g = \frac{V_{void}}{V_g} = \frac{\sum_1^n N_i \cdot \pi \overline{r}_{p.i}^2 \cdot L_e}{\pi r_g^2 \cdot t_g} = \sqrt{\tau_g} \frac{\sum_1^n N_i \cdot \overline{r}_{p.i}^2}{r_g^2} \tag{3.26}$$

Then the total number of the equivalent capillaries of the porous medium can be determined by combining Eq. (3.24) and Eq. (3.26), which leads to:

$$N = \frac{\vartheta_g}{\sqrt{\tau_g}} \frac{r_g^2}{\sum_1^n \Lambda_i \overline{r}_{p.i}^2} \tag{3.27}$$

According to Eq. (3.13) and Eq. (3.14), the current and the flow rate for a single capillary of radius $\overline{r}_{p,i}$ is given as:

$$I_{p,i} = \alpha_{11,i} E_x + \alpha_{12,i} P_x \Big|_{a=\overline{r}_{p,i}} \tag{3.28}$$

$$Q_{p,i} = \alpha_{21,i} E_x + \alpha_{22,i} P_x \Big|_{a=\overline{r}_{p,i}} \tag{3.29}$$

At the steady state, the net current along the porous glass disk should be zero, i.e.:

$$\sum_1^n N_i I_{p,i} = N \left(\sum_1^n \Lambda_i \alpha_{11,i} E_x + \sum_1^n \Lambda_i \alpha_{12,i} P_x \right) = 0 \tag{3.30}$$

Furthermore, the overall flow rate passing across the porous glass can be expressed as:

$$Q_g = \sum_1^n N_i Q_{p,i} = N\left(\sum_1^n \Lambda_i \alpha_{21,i} E_x + \sum_1^n \Lambda_i \alpha_{22,i} P_x\right) \tag{3.31}$$

The discrete step *n* is a critical parameter to distinguish the uniform-capillary model and the heterogeneous-capillary model. When *n* equals 1, the theoretical model derived above becomes the uniform-capillary model. Normally n is selected as an integer larger than 1.

3.2.3 Relationships between FO and EK submodules

3.2.3.1 Fluid flow rate

When the FO-EK energy conversion system is in operation, the flow rate of the dilute solution passing across the porous glass should be equal to that of the solvent permeating flow rate across the semipermeable membrane, i.e.:

$$Q_g = A_m J_w \tag{3.32}$$

where A_m is the effective area of the semipermeable membrane.

3.2.3.2 Pressure drop

The overall pressure drop generated along the flow direction, ΔP, is composed of two parts: the pressure drop in the porous glass ΔP_{glass}, which is used to generate electric energy, and the pressure drop along the pipeline ΔP_{tube}, which is due to the hydrodynamic friction of the pipeline. With the expressions of $\Delta P_{glass} = -P_x L_e$ and $\tau_g = (L_e/t_g)^2$, the pressure drop in the porous glass can be obtained as:

$$\Delta P_{glass} = -\sqrt{\tau_g} t_g P_x \tag{3.33}$$

In addition, the pressure drop along the pipeline ΔP_{tube} is given as:

$$\Delta P_{tube} = \rho g h_f \tag{3.34}$$

where h_f is the head loss, given by the Darcy-Weisbach equation $h_f = \frac{f_c L_p V^2}{2gD_p}$. L_p and D_p are the length and the diameter of pipeline, respectively; V is the average velocity of fluid; f_c is the coefficient of surface resistance, usually known as friction factor. For the case of Re < 2000, the friction factor is given as: $f_c = 64/\mathrm{Re}$ [102].

3.3 Experiment

Experiments were carried out to assess the performance of the FO-EK energy conversion system and validate the afore-developed theoretical model. The experimental system is shown in Figure 3.5. The assembly diagrams of the FO submodule and the EK submodule are shown in Figures Appendix A and Appendix B, respectively. For the FO submodule, a flat-sheet cellulose triacetate (CTA) FO membrane (Hydration Technology Inc., Albany, OR) is utilized. For the EK submodule, a porous glass disk (Schott Duran®) is used in experimental study due to its good chemical and physical properties. It is established that the electrolyte solution across the porous glass must be of relatively lower concentration for producing larger streaming potential [27, 31]. Furthermore, at a lower solution concentration, the Debye length is relatively thicker which contributes significantly to the streaming current and the streaming potential, and also reduces the magnitude of the conduction current. Thus DI water processed by a water deionization system (Millipore Milli-Q Ultrapure Gradient A10), instead of electrolyte solution, is

utilized as the fluid passing through the porous glass. In addition, the NaCl solution with various molarities of 0.5 M, 1 M, 2 M, 3 M and 4 M are used as the DS in the FO submodule.

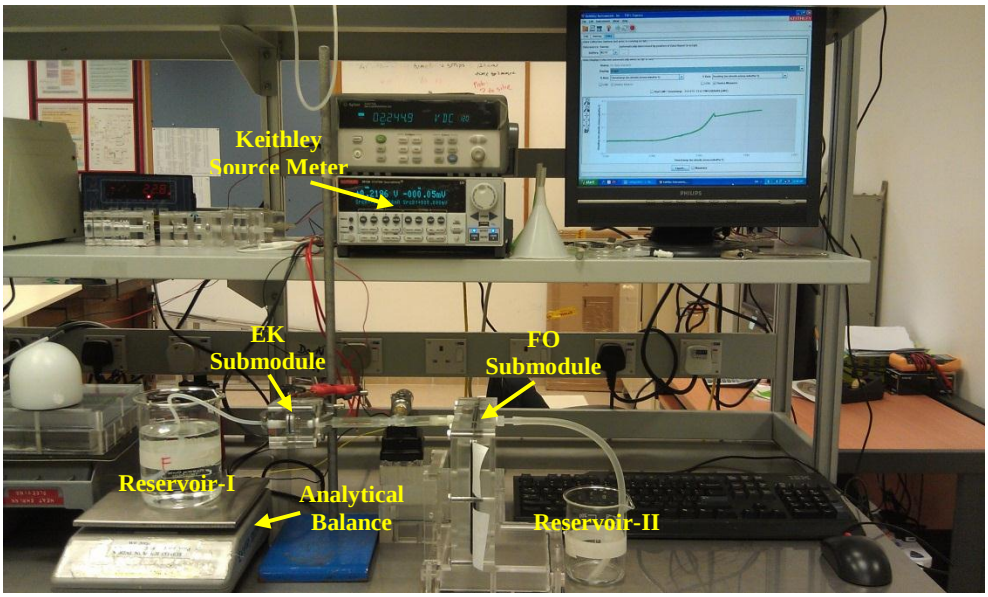

a

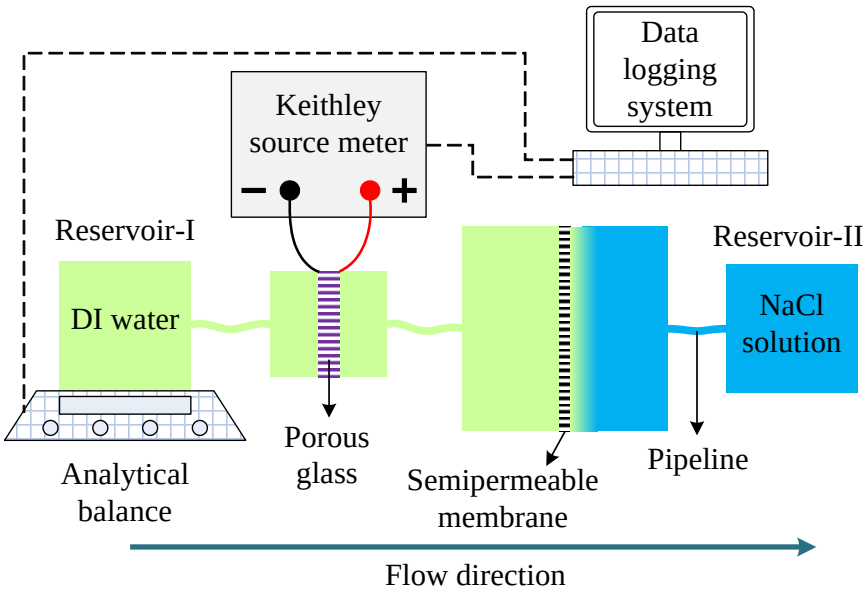

b

Figure 3.5 The experimental system (a) and the corresponding schematic of the experimental system (b) with DI water and NaCl solution as the feed solution (FS) and the draw solution (DS), respectively. A porous glass with radius of 9 mm and thickness of 3.72 mm and a cellulose triacetate (CTA) membrane with effective area of 0.0144 m^2 are used as the EK porous medium and the FO semipermeable membrane.

During the experiment, the suction force created in the FO submodule drives DI water continuously flowing through the porous glass where the streaming current and the streaming potential are generated. Two Silver/Silver-Chloride (Ag/AgCl) electrodes of mesh form are used, and each is placed on each side of the porous glass. Crocodile clips are clipped onto the electrodes for measurement. The measured results are logged into a computer for subsequent processing and analysis. After passing across the porous glass, the DI water continuously flows to the FS chamber of the FO submodule to mix with the original DI water. Finally the mixed DI water makes its way across the membrane driven by osmotic pressure difference to the DS chamber. An orifice on the top of the DS chamber is designed to discharge the excess solution in the DS chamber into a collection container, which maintains a constant static head at the DS side.

The conductivity of DI water is measured as 1.163 μS cm^{-1}. Characteristic parameters of the CTA semipermeable membrane are given as: $A = 2.2 \times 10^{-12}$ m Pa^{-1} s^{-1}, $S = 0.625 \times 10^{-3}$ m [3], and the area of the membrane A_m is 0.0144 m^2. In addition, three sized porous glasses are investigated in this work, and their detailed structure and physical parameters are shown in Table 3.1.

Other relevant parameters involved are as follows: T = 298 K, $\rho = 10^3$ kg m^{-3}, ε_r = 78.5, $\varepsilon_0 = 8.854 \times 10^{-12}$ C m^{-1} V^{-1}, $\eta = 1 \times 10^{-3}$ Pa s, $k_B = 1.381 \times 10^{-23}$ J K^{-1}, $e = 1.602 \times 10^{-19}$ C and z = 1.

Table 3.1 Structure and physical parameters of the three sized porous glass used in experimental study.

Porous glass No.	r_{max} [μm]	ϑ_g [%]	τ_g	c_{eff}/c	r_g [mm]	t_g [mm]	ζ [V]	μ_p/r_{max}	σ_p/μ_p
PG1	50	31.16	3.0	0.86	9	3.72	0.055	0.75	0.5
PG2	20	24.94	1.9	0.8					
PG3	8	21.33	1.43	0.76					

3.4 Results and discussion

Three different sets of results are presented for comparison study, with one set obtained from the experimental data and the other two sets from the theoretical predictions of the uniform-capillary model and the heterogeneous-capillary model. With all the given parameters elaborated in last section, the theoretical models are numerically solved by using a self-developed code with the software of Wolfram Mathematica.

3.4.1 Discrete segments of the capillary model

Since the FO-EK energy conversion system is for power generation, the output power density is a key parameter in assessing the performance of the energy conversion system. The output power density for this system is defined as a ratio of the generated power to the overall volume of micro/nano-channels [103]. The experimental results, Figure 3.10, show that the power density generated from this system using PG3 is much greater than that using PG1 or PG2. Therefore, to facilitate the study of the discrete segments, the output power density generated by PG3 is selected for analysis.

Figure 3.6 presents the effects of the discrete segments *n* in the capillary model on the output power density, which shows that with increasing the number of discrete segments the theoretical results better agree with the experimental results. Furthermore, the two curves of the output power density for the cases of n = 10 and n = 20 are indistinguishable, indicating that the number of the discrete segments has no effect on the capillary model result when n is greater than or equal to 10. Consequently, n = 10 is chosen as the standard number of the discrete segments in the heterogeneous-capillary model for later analyses.

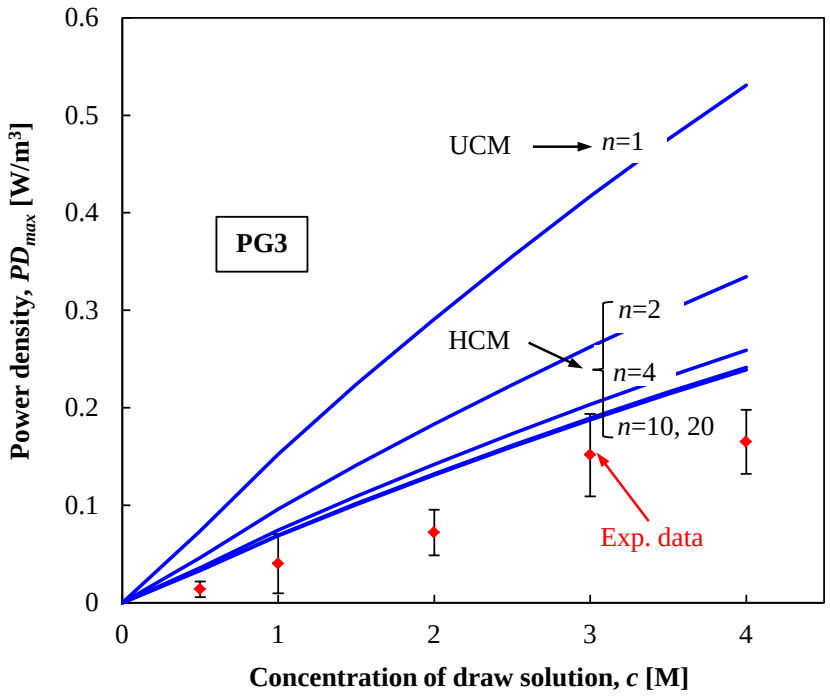

Figure 3.6 Effects of the number of discrete segments *n* used in the capillary model on the output power density from PG3. UCM and HCM respectively represent the uniform-capillary model and the heterogeneous-capillary model.

3.4.2 Flux and flow rate

Figure 3.7 shows the effects of DS concentration on the permeating flux J_w which characterizes the membrane performance in the FO submodule. The results show that the theoretical relationship given by Eq. (3.5) can explain the trend of the experimental data very well.

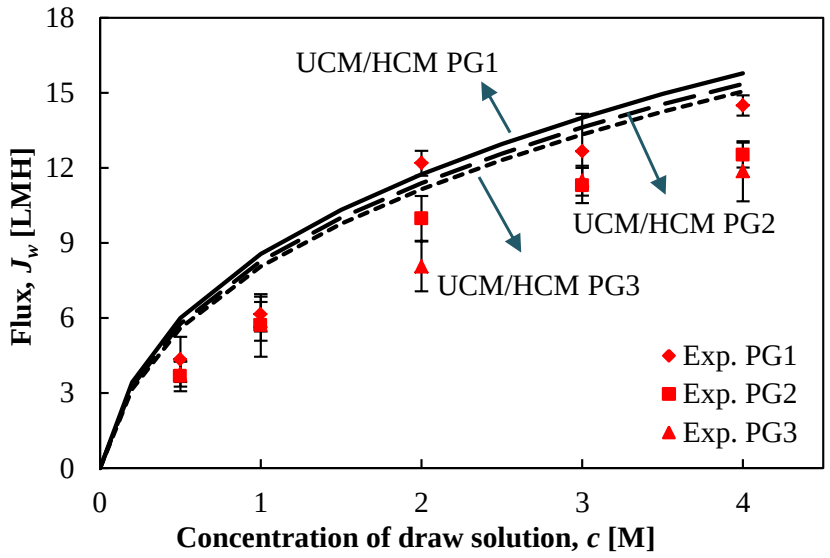

Figure 3.7 Effects of draw solution (DS) concentration on permeating flux J_w. Here, LMH means L m^{-2} h^{-1}.

In addition, the experimental permeating fluxes obtained from three different sizes of porous glass become larger with increasing the DS concentration but perform quite close with each other, especially in the low concentration region. This observation shows that under our experimental conditions the concentration difference between the DS and the FS has a more significant effect on the permeating flux than the pore size of porous glass. This conclusion can also be confirmed by the theoretical models. Based on the theoretical results, both the uniform- and heterogeneous-capillary models yield almost the same flux

variation curves for each size of porous glass. Furthermore, it is seen from the figure that, at condition of the same DS concentration, the slight difference between these three fluxes is obviously induced by the porous glass, showing the smaller the pore size, the larger the pressure drop within porous glass and thus the lower the flux. Finally, it is clear that a larger concentration difference between the DS and the FS generates a higher permeating flux. However, higher permeating flux can induce more serious concentration polarization effects, resulting in slow increment of the permeating flux. This is the so-called self-limiting effect [86] which can reasonably explain the phenomenon that both experimental and theoretical fluxes increase sharply at low concentration region but slowly at high concentration region. Due to the linear relationship represented by Eq. (3.32), a similar trend can also be concluded for the flow rate Q_g.

3.4.3 Pressure drop

Figure 3.8.a and Figure 3.8.b respectively show the predicted results of the ratio of the pressure drop caused by the porous glass to the overall pressure drop $\Delta P_{glass}/\Delta P$ and the ratio of the overall pressure drop to the effective osmotic pressure difference $\Delta P/\Delta \pi_{eff}$. Both the uniform-capillary model and the heterogeneous-capillary model are included. One important fact is that for each size of porous glass, these two kinds of ratios do not change with the DS concentration. In other words, these two ratios are only a function of the pore size of porous glass. Also the two ratios predicted from the uniform-capillary model are slightly higher than those from the heterogeneous-capillary model. As seen from Figure 3.8.a, both theoretical models show a similar trend, namely the pressure drop in porous glass decreases with increasing the pore size of porous glass. A similar trend is also noted for the ratio of $\Delta P/\Delta \pi_{eff}$ shown in Figure 3.8.b, which indicates that the use of

porous glass with a smaller pore size generates a larger proportion of the overall pressure drop to the effective osmotic pressure difference. Although there is a remarkable increase of the ratio of $\Delta P/\Delta\pi_{eff}$ with decreasing the pore size, a maximum ratio of 0.149% is noted according to the heterogeneous-capillary model.

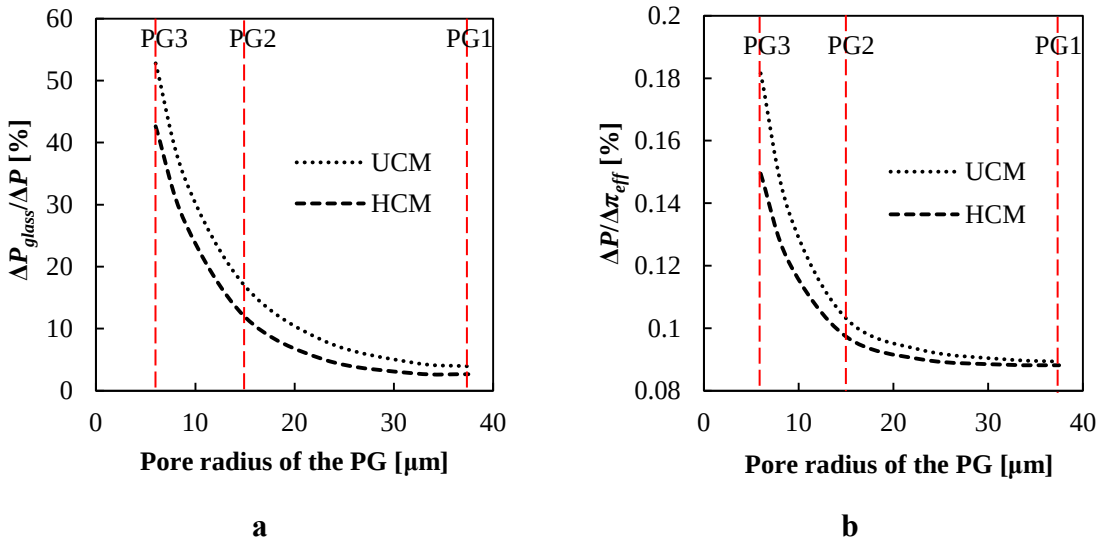

Figure 3.8 Theoretical predictions of both the uniform-capillary model (UCM) and the heterogeneous-capillary model (HCM) for (a) Ratio of the pressure drop caused by the porous glass to the overall pressure drop $\Delta P_{glass}/\Delta P$ and (b) Ratio of the overall pressure drop to the effective osmotic pressure difference $\Delta P/\Delta\pi_{eff}$.

3.4.4 Streaming potential and maximum streaming current

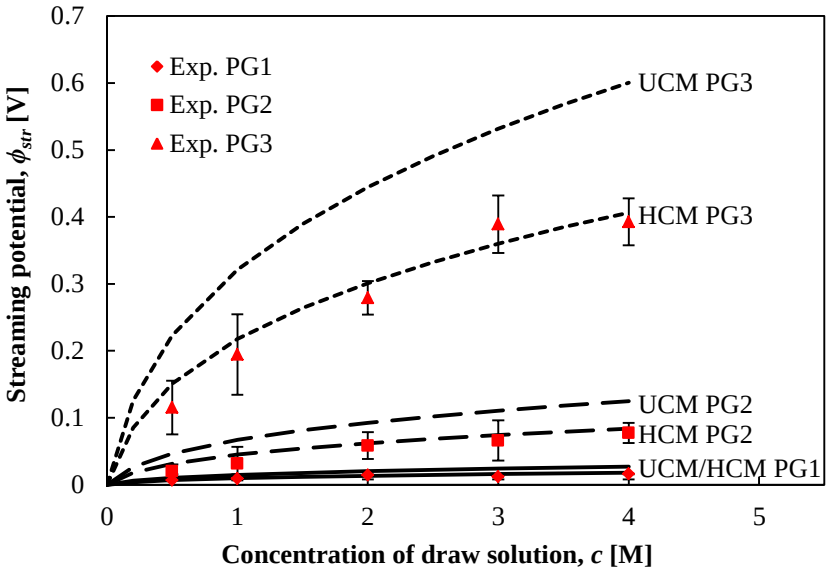

a

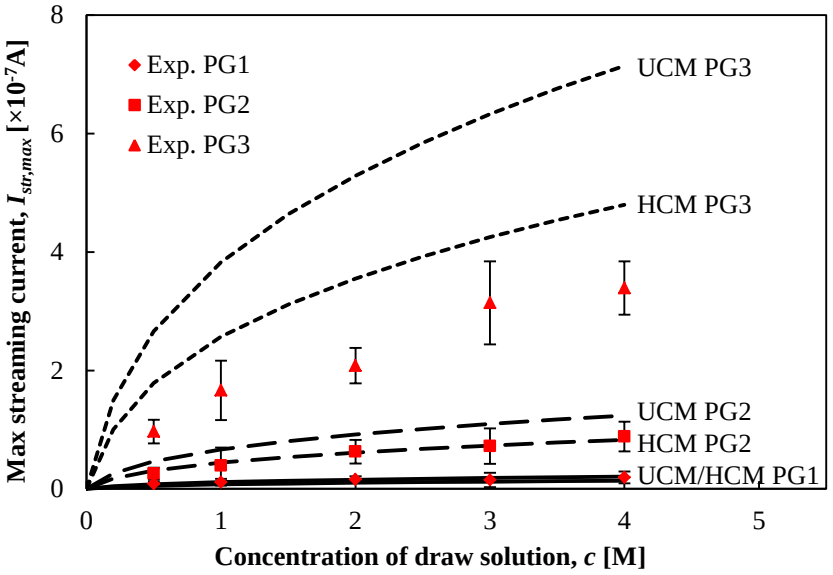

b

Figure 3.9 Effects of draw solution (DS) concentration on streaming potential ϕ_{str} (a) and maximum streaming current $I_{str,max}$ (b).

Figure 3.9.a and Figure 3.9.b present the effects of the DS concentration on the generated streaming potential ϕ_{str} and maximum streaming current $I_{str,max}$, respectively.

Both theoretical and experimental results show that for a given size of porous glass, the streaming potential and the maximum streaming current increase with increasing the DS concentration; the increment is sharper at low concentration and slower at high concentration. As shown from Figure 3.9.a, for each size of porous glass, the generated streaming potentials predicted by the heterogeneous-capillary model are more consistent with the experimental results, while the uniform-capillary model overestimates the results. Figure 3.9.b shows that, compared to the experimental maximum streaming currents, the heterogeneous-capillary model provides good predictions for PG1 and PG2, but a slightly overestimated prediction for PG3. However in general, the heterogeneous-capillary model shows better agreement with the experimental data than the uniform-capillary model.

In addition, both theoretical and experimental results show that for a given DS concentration the porous glass of larger pore size, such as PG1 or PG2, yields relatively lower streaming potential and maximum streaming current than the porous glass of smaller pore size like PG3. Thus it can be concluded that porous glass of smaller pore size performs better in EK energy conversion process.

3.4.5 Output power density

At a certain DS concentration, the electric power converted from the induced EK flow in porous glass is the multiplication of potential with current. Since the streaming current is a linear decreasing function of the terminal potential difference under the open-circuit condition, the maximum power output occurs at the half of the streaming current where the current is exactly the half of the maximum streaming current [32, 36], namely:

$$P_{power,max} = \frac{1}{4}\phi_{str} \cdot I_{str,max} \tag{3.35}$$

If the ratio of the generated power to the overall volume of micro/nano-channels is introduced as the power density [103], *PD*, the maximum power density is given by:

$$PD_{max} = \frac{P_{power,max}}{V_g \vartheta_g} \tag{3.36}$$

where $V_g\vartheta_g$ is the overall volume of micro/nano-channels. Based on this equation, we can obtain both the theoretical and the experimental maximum power densities which are plotted in Figure 3.10. A nearly monotonously increasing relationship between the maximum power density and the DS concentration is observed in this figure. In addition, the curves of the maximum power density predicted from the heterogeneous-capillary model are consistent with the experimental results. However, the uniform-capillary model overestimates the maximum power density, especially for the porous glass of small pore size like PG3. Furthermore, the maximum power density predicted by the heterogeneous-capillary model is 0.241 W m^{-3} and the maximum experimental power density is 0.165 W m^{-3}; both can be achieved by using the porous glass with an average pore size 6 μm at a 4 M DS concentration. In addition, if typical seawater (equivalent to 0.5 M NaCl solution) and rive water (equivalent to 0.005 M NaCl solution) are employed as the DS and the FS respectively, the generated maximum power density can be predicted as 0.033 W m^{-3} based on our theoretical model. It is shown that the maixmum power density obtained in this study is about the same order of magnitude as the power density of EK power conversion reported in a similar porous material [28]. The difference is that, rather than being driven by the salinity gradient utilized in this study, the EK power generation

process reported in the literature is due to pressure-driven flow induced by external pumping.

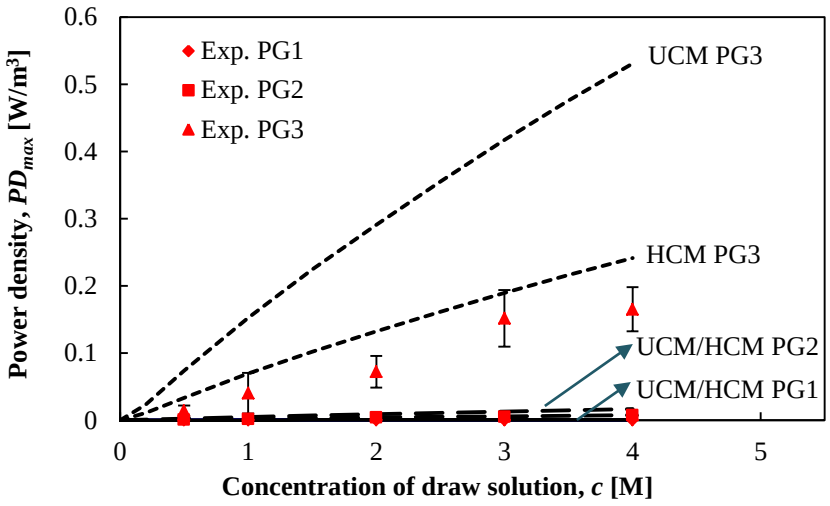

Figure 3.10 Effects of draw solution (DS) concentration on the maximum power density PD_{max}.

Alternatively the power density can also be defined as the ratio of the generated power to the effective surface area of a semipermeable membrane. With such surface power density, the order of magnitude of the calculated power density for PG3 is about 10^{-6} W m^{-2}. Although this value is much smaller compared to the other two membrane-based power generation technologies, PRO and RED, with their power densities of order about 1 W m^{-2} [3], the proposed EK-FO technique has a great potential to be further improved. On the one hand, as shown in Figure 3.8.b, the pressure drop caused by the pipeline and the porous glass is generally no more than 0.149% of the effective osmotic pressure generated in the FO submodule. This means that the EK submodule could be greatly scaled up to make the best use of the effective osmotic pressure and thus gives rise to much higher power density. On the other hand, since this new hybrid energy

conversion system is still in its initial stage, it is expected to greatly increase the generated power density through further improvement in design and operation, such as the use of the continuous flow mode instead of the currently applied batch mode, and the surface treatment to FO semipermeable membrane (for less polarization) and porous glass (for stronger EK effect) etc.

The energy conversion efficiency η_{eff} is defined as the ratio of the useful energy output to the total energy input. Specifically, for this study, the generated power is the useful energy obtained, which is given by Eq. (3.35), and the energy flow rate delivered from the spontaneous mixing of two solutions with two different concentrations is the energy input, which is given as [3]:

$$P_{power,mix} = 2RTQ_g \left(C_D \ln \frac{C_D\left(1+\frac{V_F}{V_D}\right)}{C_D + C_F \frac{V_F}{V_D}} + C_F \frac{V_F}{V_c} \ln \frac{C_F\left(1+\frac{V_F}{V_D}\right)}{C_D + C_F \frac{V_F}{V_D}} \right) \qquad (3.37)$$

where R is the universal gas constant, C_c and C_d are respectively the concentrated solution concentration and the dilute solution concentration in unit of mol m^{-3}, V_c and V_d are volumes of the concentrated solution and the dilute solution being mixed. Taking the typical seawater and river water as example, the energy conversion efficiency can be estimated as 0.15%. This estimation shows that the hybrid energy conversion technology reported in this study is of competitive compared to the other pressure-driven EK power generation technologies, such as the mechanical-electrokinetic battery [27] and the electrokinetic micro/nano-channel battery [28] with maximum energy conversion efficiencies of 0.77% and 0.045%, respectively.

3.5 Summary

In this chapter, both theoretical and experimental studies are conducted to assess the performance of the proposed FO-EK hybrid energy conversion system. Two different mathematical models are presented, and they are the uniform-capillary model and the heterogeneous-capillary model. The following conclusions can be drawn:

1. Under the experimental conditions, the performance of the proposed hybrid FO-EK energy conversion system is better for a porous glass with a smaller pore size, and it almost monotonously increases with increasing the DS concentration;
2. The heterogeneous-capillary model fits well with experimental results when the discrete segments are greater than or equal to 10, and it yields more accurate results compared to the uniform-capillary model;
3. The maximum power density predicted by the heterogeneous-capillary model is 0.241 W m^{-3} and the maximum experimental power density is 0.165 W m^{-3}; both can be achieved by using the porous glass with an average pore size 6 μm at the DS concentration 4 M.

Nomenclature

a	Radius of capillary [m]
a_1	Osmosis coefficient, -4.112×10^6 [Pa M^{-1}]
a_2	Osmosis coefficient, -0.349×10^6 [Pa M^{-1}]
A	Water permeability coefficient [m Pa^{-1} s^{-1}]
A_c	Cross-section area of capillary [m^2]
A_g	Cross-section area of porous glass disk with radius r_g [m^2]
A_m	Effective area of the membrane applied in FO submodule [m^2]
A_r	Cross-section area of the representative capillary with radius $\bar{r}_p$ [m^2]
B	Solute permeability coefficient [m s^{-1}]
c	Concentration of electrolyte solution [M]
c'	Concentration of the DS when the FO-EK energy conversion system is at pseudo-equilibrium state [M]
C	Concentration electrolyte solution [mol m^{-3}] or [mM]
d_h	Hydraulic diameter [m]
d_p	Diameter of the equivalent center pore of the porous glass [m]
D	Salt diffusion coefficient [m^2 s^{-1}]
D_k	Diffusivity of ion species k [m^2 s^{-1}]
D_p	Diameter of the pipe along the pipeline [m]
e	Elementary charge [C]
E_x	Streaming potential gradient [V m^{-1}]
f	Probability density distribution function [-]

f_c Coefficient of the surface resistance [-]

F Cumulative probability distribution function [-]

G $I_1(\kappa a)/I_0(\kappa a)$ [-]

$\tilde{F}$ Faraday constant [C V^{-1}]

h_f Friction loss [m]

h_L Total head loss [m]

h_m Minor loss [m]

$\vec{\mathbf{i}}$ Electric current density vector [A m^{-2}]

I Overall electric current [A]

I_c Conduction current [A]

I_{str} Convection current or streaming current [A]

I_x Electric current along axial flow direction [A]

I_0 Zero-order modified Bessel function [-]

I_1 First-order modified Bessel function [-]

J_w Solvent flux across the membrane [m^3 s^{-1} m^{-2}]

k Mass transfer coefficient [m s^{-1}]

k_B Boltzmann constant [J K^{-1}]

k_f Minor loss coefficient [-]

K Solute resistivity [s m^{-1}]

l_p Effective length of the equivalent center pore of the porous glass [m]

L Length of the capillary [m]

L_e Effective length of the equivalent capillary of the porous glass [m]

L_p Length the pipe along the pipeline [m]

n	Total number of the steps between the maximum and minimum radiuses [-]
n_f	Amount of the fiction losses along the pipeline [-]
n_k	Ionic number concentration of the species k [m^{-3}]
n_+	Ionic number concentration of the cations [m^{-3}]
n_-	Ionic number concentration of the anions [m^{-3}]
N	Total number of the equivalent capillaries of the porous glass [-]
P	Hydrostatic pressure [Pa]
PD	Power density [w m^{-3}]
P_{power}	Output power generated in porous glass [w]
P_x	Pressure gradient, $-dP/dx$ [Pa m^{-1}]
ΔP	Overall pressure drop [Pa]
Q	Total volumetric flow rate in capillary micro/nano-channel [m^3 s^{-1}]
Q_g	Total volumetric flow rate passing through the porous glass disk [m^3 s^{-1}]
Q_r	Total volumetric flow rate passing through the representative single capillary of the porous media [m^3 s^{-1}]
r_p	Radius of the equivalent capillary [m]
$\bar{r}_p$	Mean radius of the equivalent capillaries of the porous media [m]
$r_{p,i}$	Radius of the i^{th} capillary [m]
$\bar{r}_{p,i}$	Average radius for a certain range of the capillary size distribution [m]
$r_{p,max}$	Maximum radius of the equivalent capillaries [m]
$r_{p,min}$	Minimum radius of the equivalent capillaries [m]
Δr_p	Step size of the capillary radius [m]
R	Universal gas constant [J K^{-1} mol^{-1}]

Re	Reynolds number [-]
S	Structure factor [m]
Sc	Schmidt number [-]
t	Thickness [m]
T	Temperature [K]
u_x	Velocity along the axial direction of the capillary [m s^{-1}]
V_p	Volume of the equivalent center pore of the porous glass [m^3]
V_{total}	Total volume of the porous glass [m^3]
V_{void}	Void volume of the porous glass [m^3]
z	Absolute value of the valence for (z:z) electrolyte [-]
z_k	Valence of the ion species k [-]

Greek symbols

ε	Permittivity of material [C m^{-1} V^{-1}]
ε_0	Permittivity of vacuum (free space), 8.854×10^{-12} [C m^{-1} V^{-1}]
ε_r	Relative dielectric constant [-]
ζ	Zeta potential [V]
η	Dynamic viscosity [kg m^{-1} s^{-1}] or [Pa s]
κ	Inverse of the EDL thickness [m^{-1}]
λ	EDL thickness [m]
Λ_i	Cumulative probability of the radius range from r_{i-1} to r_i
μ	Chemical potential [J mol^{-1}]
μ_p	Mean radius of the equivalent capillary [m]

π Osmotic pressure [Pa]

$\Delta\pi$ Osmotic pressure difference [Pa]

ρ_f Free charge density [C m^{-3}]

ρ Fluid density [Kg m^{-3}]

σ^{∞} Conductivity of electrolyte solution in the bulk [S m^{-1}] or [A V^{-1} m^{-1}]

σ_p Standard deviation of the radius of the equivalent capillary [m]

τ Tortuosity [-]

ν Stoichiometric number [-]

ϕ Overall electric potential [V]

$\Delta\phi$ Electric potential difference between the two ends of the porous glass [V]

ϕ_{str} Streaming potential [V]

χ Osmotic coefficient [-]

ψ Potential due to the electric double layer (EDL) [V]

ψ_s Surface potential [V]

Ω $\varepsilon\zeta/\eta$ [m^2 V^{-1} s^{-1}]

ϑ Porosity [-]

Subscripts

a Anion

b Bulk solution

c Cation

D Draw solution

eff Effective parameter

F	Feed solution
g	Porous glass disk
k	Ion species
l	Parameters related to the solvent
m	Membrane
max	Maximum value
mix	Mixture
s	Parameters related to the solute
∞	Bulk solution

Chapter 4: External concentration polarization (ECP) in forward osmosis (FO)

4.1 Introduction

Concentration polarization (CP), including external concentration polarization (ECP) and internal concentration polarization (ICP), is a significant inherent phenomenon occurring in membrane-based separation processes, which decreases the chemical potential gradient across the membrane, and thus reduces the solvent permeating flux, and finally diminishes the separation efficiency. Different from reverse osmosis (RO) suffering from high externally imposed pressure at the high concentration side, the forward osmosis (FO) process operates without need of any extra pressure. Therefore, the asymmetric semipermeable membrane used in FO process has lower propensity to get series ICP, especially when the porous support layer facing against dilute solution. In fact, studies have demonstrated that the ECP effect, particularly at the concentrated solution side, plays overwhelming roles in determining the performance of FO process [104, 105]. However, most of those previous studies always straightforwardly start their research based on high tangential volume flow rate. In this situation, the ECP layer can be well controlled in a quite thin region near the membrane surface and then studies proceed to focusing on the other effects such as ICP [74, 106-109], properties of feed solution (FS) and/or draw solution (DS) [82, 110-116], membrane structures [77, 78, 80, 117-128], flow patterns [129-131], etc. Evidently, higher tangential volume flow rate

definitely gives rise to lower ECP, but also induces higher propensity of fouling and scaling of membrane [132] and higher energy consumption. Above all, the FO efficiency does not always increase significantly with the growth of tangential volume flow rate. When the volume flow rate beyond a certain value, the FO efficiency will be kept level off [104]. Although the ECP effect plays significant role in FO process, to the best knowledge of author, neither experimental study has been systematically conducted to investigate the properties of such ECP layer, nor the experimental visualization and quantitative characterization.

In addition, for existing theoretical studies, two classical theories about FO process are film theory [86, 87, 131, 133-137] and convection-diffusion theory [138-142]. Film theory is a one-dimensional (1D) analytical model based on assumptions that, solvent permeating flux along the membrane is axially invariant and it has no effect to the axial velocity field [143]. In real FO process, however, the solvent permeating flux will definitely dilute the DS, which, in turn, decreases the permeating flux at the downstream region. Meanwhile, once the solvent permeates across the membrane into the DS chamber, the axial velocity profile must be varied due to the constant cross-section area of the chamber. Conversely, the convection-diffusion theory, composed by mass transfer equation, momentum equation and convection-diffusion equation, can provide much more actual predictions to the FO process since it is free of assumptions proposed in film theory.

Furthermore, it is also found that, from the pioneer proposal of FO concept [137, 144] to its application, most of performance studies on FO are conducted from macroscopic perspective. Jensen, Lee et al. [145] studied FO on a chip with channel

dimensions in order of micrometer, but only focused on functional study of osmosis pump rather than mechanism study of FO. As well known that, compared to conventional technologies, microtechnology could provide a quantity of potential benefits, which, particularly for the FO study in microscope, include enhancing water transport, improving system performance, increasing separation efficiency, and facilitating experimental studies on FO mechanism.

Consequently, the objective of this chapter is to study the ECP phenomenon in FO process based on microtechnology. In particular, experimental study is firstly conducted to investigate the variations of FO flow rate and FO efficiency with increasing the tangential volume flow rate and to visualize and quantify the ECP phenomenon in FO process through a microchannel device. In order to further interpret experimental study, corresponding numerical simulation is also conducted based on convention-diffusion theory.

4.2 Experiment

4.2.1 Design and fabrication of FO device

To study FO process with focusing on properties of ECP layer on DS side, a microchannel system is firstly designed and fabricated in this work which consists of two identical FO chambers for DS and FS as sketched in Figure 4.1.a. Fluorescent solution together with microscope is utilized to visualize the ECP layer. In order to get a clear view on the platform of microscope, the FO device should be transparent and as small as possible, and the side-surfaces of the channel device perpendicular to the FO flux should be kept smooth enough. Inspired by conventional photolithography technique in

fabricating poly-dimethylsiloxane (PDMS) micro/nano-channels, an aluminous channel mode with four smooth side-walls for casting PDMS is pre-fabricated by milling and grinding. Based on this specially designed FO mode, these basic requirements for channel device mentioned above could be easily satisfied. For this FO device, two chambers share the same channel structure, being composed of one main channel for FS/DS and two subordinate channels as inlet and outlet. Schematic of the DS chamber and the corresponding main dimenisons are shown in Figure 4.1.b. Length l_0 and width w_0 of the cross-section of main channel facing against the semipermeable membrane are 25 mm and 500 μm, respectively. The height h_0 of the main channel is 1 mm. In addition, the cross-section of the inlet/outlet channel is 500 μm × 500 μm with height of 10 mm. The overall FO device is mechanically assembled together by two cover sheets of polymethyl methacrylate (PMMA) and two bolts. The size of the membrane should be a little bit larger than the cross-section of main chamber but smaller than the cross-section of PDMS block. Only in this way, the FO membrane can be well sealed in between the FS and the DS chambers without any fluid leakage.

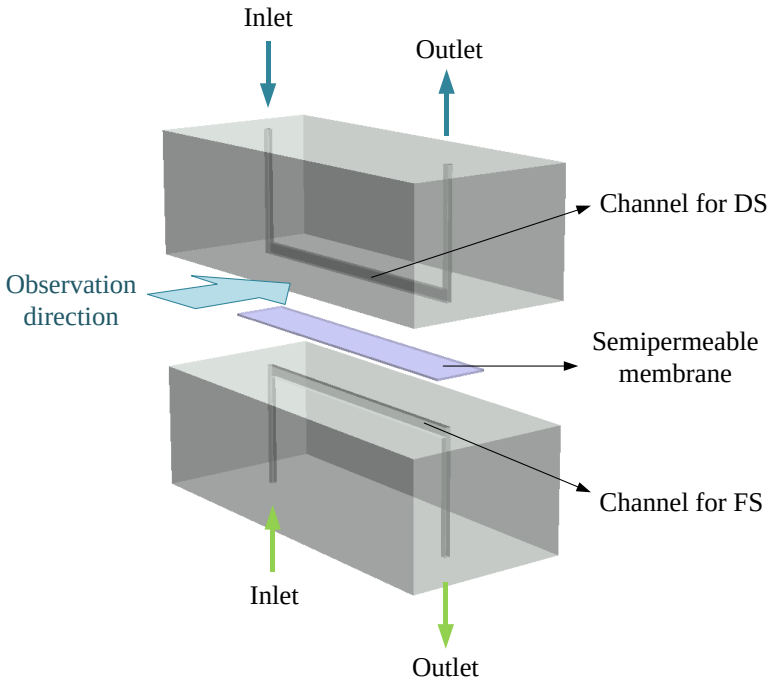

a

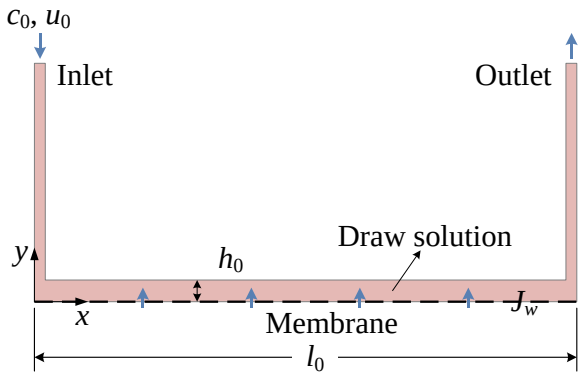

b

Figure 4.1 a. Schematic of main components of the FO device; b. Main dimensions of the DS chamber. In figure b, the dashed line represents the semipermeable membrane, c_0 and u_0 are respectively the initial concentration and the inlet velocity of DS; h_0 and l_0 are respectively the height and the length of the main DS channel; and J_w is the solvent permeating flux due to osmotic pressure difference between the DS and the FS.

In this work, a kind of flat-sheet cellulose triacetate (CTA) FO membrane (Hydration Technology Inc., Albany, OR) is utilized as the semipermeable membrane due to its remarkable property of high water permeability coefficient. This kind of membrane consists of a thin selective layer and a thick embedded-polyester-woven porous support layer. The overall thickness varies from 30 to 50 μm depending on different locations. This thickness property meets well with the requirement of assembling the FO device since that such thin FO membrane induces negligible deformation to the soft PDMS blocks. The dense selective layer of membrane is placed against the DS, which is the most common assembly pattern applied in FO separation process. Since this kind of semipermeable membrane has a high salt rejection of more than 99%, the salt flux across the membrane can be reasonably ignored. In addition, this specially designed FO membrane can effectively diminish the ICP due to the significantly reduced thickness of the porous support layer compared with conventional FO membranes [109]. Meanwhile, the DI water is employed as the FS to further reduce the ICP effects to almost zero. In those situations, the ICP at the FS side could be reasonably decoupled from FO process.

4.2.2 FO experiment setup and procedure

The FS and the DS used in this study are DI water and NaCl solution with a concentration of 1 M. In order to visualize the ECP phenomenon, Fluorescein-Na (Sigma-Aldrich Corporation, Singapore), a kind of fluorescent solute with excitation/emission wavelength of 460 nm/515 nm, was utilized. The concentration of Fluorescein-Na solution was prepared at 55.4 μM. The diffusivities of NaCl and Fluorescein-Na are 1.48×10^{-9} m^2 s^{-1} and 4.25×10^{-10} m^2 s^{-1} [146], respectively. An epifluorescence microscope (Carl Zeiss, Germany) illuminated by a mercury lamp (Zeiss,

mbq 52ac) was applied to observe the fluorescein solution. A coupled charge device (CCD) camera (Sensovation AG, Germany) together with 5× objective lens was employed to capture the optical images which were simultaneously stored into a computer through software Sensovation SamBa EZ-series, IEEE 1394. In addition, a two-channel syringe pump (KDScientific, USA) was employed to provide continuous volume flow rate to FS and DS. A precious analytical balance (B-220C, Fisher Scientific) with readability of 0.0001 g was used to measure the FO permeating volume flow rate. For all experimental study, co-current flow of FS and DS was adopted to balance the pressure generated in two chambers beside membrane. Prior to each test, FO device should be cleaned and rinsed by DI water in an ultrasonic machine for 30 minutes and dried by compressed air.

4.2.2.1 Relationship between FO efficiency and Reynolds number

Experiments in this section mainly focus on characterizing the relationship between the FO volume flow rate and the tangential volume flow rate. The schematic of the experiment setup is shown in Figure 4.2. The DI water and the 1 M NaCl solution mixed with 55.4 μM Fluorescein-Na solution were employed as the FS and the DS, respectively. Since the weight measurement was significantly sensitive to external noise, all slits on the glass cover of balance were required to be tightly sealed. Two syringes together with syringe pump were used to provide tangential flow through the FO device. If air bubbles were trapped inside the chambers or tubes, a higher volume flow rate was applied to flush away those bubbles. Measurements of weight variation of FS were conducted throughout all experiments in this section since that, different with DS, the density of FS was constant for all FO process no matter how the tangential volume flow rate changes.

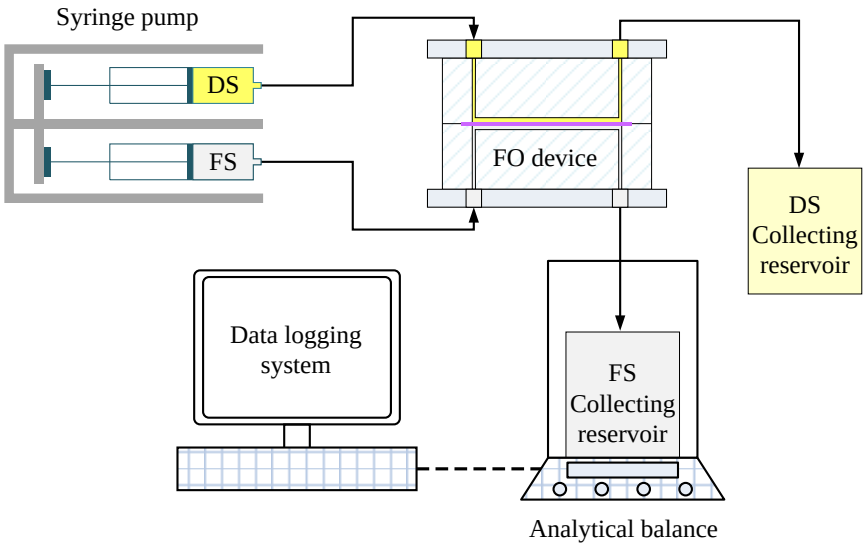

Figure 4.2 Schematic of the volume flow rate measurement system.

For calibration experiment, both chambers of FO device were injected with FS so that there was no osmotic flux across the membrane. With syringe pump running at a certain volume flow rate (5, 10, 20, 40, 60, 80, 100 and 150 μl min^{-1}), the weight vartiation was accurately monitored and recorded by data logger which could be further processed into the real volume flow rate provided by syringe pump. For measurement of FO volume flow rate, DS and FS were separately filled into the corresponding chamber. Along with FO running, the FS permeated across the membrane into the DS chamber, diluting the DS. Meanwhile, the weight variation of FS was also recorded which could be later processed to another volume flow rate. The difference between these two kinds of volume flow rate is just the FO volume flow rate.

4.2.2.2 Relationship between CP layer and Reynolds number

The main focus of this experiment is to visualize the ECP layer and quantify the osmotic pressure distribution within the ECP layer at different Reynolds numbers. Along

with FO proceeding, the DS is continuously diluted by the permeating DI water from the FS side but also simultaneously refreshed by the injected DS. Finally, the DS reaches a steady state with large concentration gradient within the layer nearby membrane but almost zero at the region far away from membrane. Based on the same mechanism, the fluorescein-Na solution should also be diluted and refreshed and finally reaches such steady state. The concentration variation of Fluorescein-Na can be easily detected by microscope with exciting illumination. Therefore, the Fluorescein-Na was utilized here to indirectly visualize the ECP layer of NaCl solution.

Experiments showed that, even in the situation of no FO flux, images of the DS channel taken under exciting light exhibited heterogeneous distribution of gray value due to the inevitable fabrication defection. In order to decouple this intrinsic noise, calibration experiment should be conducted first. The schematic of ECP layer visualization experiment is shown in Figure 4.3. For calibration experiment, DS was injected into both DS and FS channels by syringe pump to purely visualize the DS channel, so that the microscope could accurately capture the background view of the DS channel. Visualization experiment of ECP layer was then conducted based on the calibration experiment. In this experiment, DS and FS were simultaneously injected into the corresponding DS channel and FS channel. For both experiments, syringes were fixed onto a syringe pump which was previously set at a required volume flow rate, 50 μl min^{-1}, 100 μl min^{-1} or 150 μl min^{-1}. Meanwhile, five observation points with equal intervals along axial direction of DS channel were determined with assistance of tick marks on the object stage. All those images taken from calibration experiment and visualization experiment at the pre-determined observation points were then post-processed by

software of Adobe Photoshop CS4, Wolfram Mathematica 8 and ImageJ to figure out the pure images of ECP layer at different axial positions and different Reynolds numbers.

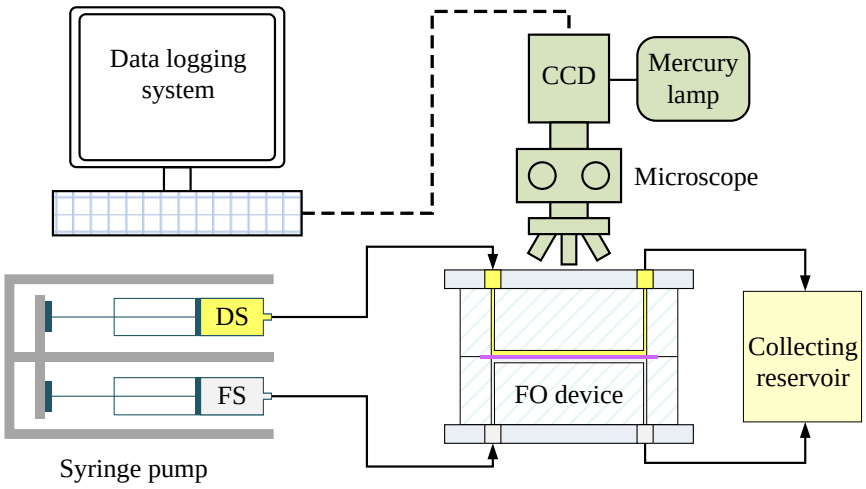

Figure 4.3 Schematic of external concentration polarization (ECP) layer visualization experiment.

4.3 Numerical simulation

4.3.1 Governing equations

In order to interpret experimental results, a two-dimensional (2D) numerical simulation about the steady FO process confined in a microchamber is accordingly conducted. The CP effect at the FS side could be reasonably ignored due to that the DI water is employed as FS and the high-salt-rejection CTA membrane is utilized as the semipermeable membrane. In this situation, analysis only focuses on ECP layer at the DS side with assumptions that parameters including fluid density ρ, diffusivity D, and dynamic viscosity η are independent on solution concentration and the FO membrane is

strictly semipermeable with 100% rejection to salt. The simplified 2-D configuration of the DS channel is shown as Figure 4.1.b. The convection-diffusion theory is utilized here by combining momentum equation, continuity equation and convection-diffusion equation. Scaling analysis is recommended in numerical study. Non-dimensional variables are defined as: $\tilde{\nabla} = h_0 \nabla$, $\tilde{\mathbf{u}} = \frac{\mathbf{u}}{u_0}$, $\tilde{p} = \eta \frac{p_0 u_0}{h_0}$, $\tilde{c} = \frac{c}{c_0}$, $\mathrm{Re} = \frac{h_0 u_0 \rho}{\eta}$, $\mathrm{Pe} = \frac{u_0 h_0}{D}$. Re and Pe are the Reynolds number and Péclet number. Based on those pre-defined non-dimension parameters, governing equations for steady fluid flow without any body force and source term are given as:

Momentum equation: $\mathrm{Re}\left[\tilde{\mathbf{u}} \cdot \tilde{\nabla} \tilde{\mathbf{u}}\right] = -\tilde{\nabla} \tilde{p} + \tilde{\nabla}^2 \tilde{\mathbf{u}}$ (4.1)

Continuity equation: $\tilde{\nabla} \cdot \tilde{\mathbf{u}} = 0$ (4.2)

Convection-diffusion equation: $\mathrm{Pe}\left[\tilde{\mathbf{u}} \cdot \tilde{\nabla} \tilde{c}\right] = \tilde{\nabla}^2 \tilde{c}$ (4.3)

Moreover, Fluorescein-Na is utilized in experimental part to visualize and quantify ECP layer. Therefore, in addition to the mass transfer equation for NaCl, another mass transfer equation for the fluorescent solution concentration should also be counted into the governing equations. For the FO process, it is assumed that the osmotic pressure is only created by the NaCl solute since the concentration of Fluorescein-Na could be reasonably neglected compared to that of NaCl. Meanwhile, it is assumed the diffusion processes of these two kinds of solutes have no mutual effect with each other.

4.3.2 Boundary conditions

Referring to Figure 4.1.b, boundaries of the simulation domain can be generally categorized into four types: the inlet, outlet, membrane and walls. Dimensionless boundary conditions are analyzed in this section.

For momentum and continuity equations, velocity at the inlet is unit; at the outlet, the pressure is treated as zero; the permeating flux of DI water perpendicular to membrane surface due to osmotic pressure difference is expressed as $\frac{ARTc_0}{u_0}\tilde{c}_1$ with *A*, *R*, *T* and subscript '1' representing water permeability coefficient, universal gas constant, temperature and NaCl salt; no-slip boundary condition is applied to all the walls.

For mass transfer equation for the concentration distribution of NaCl solution, concentration at the inlet is unit which is freely developed with the fluid flow at outlet; mass insulation boundary is reasonably set at membrane and all walls. All boundaries conditions corresponding to mass transfer equation of fluorescent solution are same with those of NaCl solution except that the fluorescent solution concentration at inlet is $\tilde{c}_2$, normalized by c_0, with subscript '2' representing fluorescent salt.

Here the no-slip boundary is mathematically expressed as $\tilde{\mathbf{u}} = 0$. And the insulation boundary is generally defined as that the electrolyte flux due to convection equals to that due to diffusion, i.e., $-\frac{1}{\mathrm{Pe}}\mathbf{n}\cdot\tilde{\nabla}\tilde{c} + \mathbf{n}\cdot\tilde{\mathbf{u}}\tilde{c} = 0$.

Numerical simulations were performed by using commercially available finite element software, Comsol Multiphysics 3.5a (Comsol Inc., Sweden), with coupling three build-in modes. One incompressible Navier-Stokes mode was applied to solve the velocity filed and two convection-diffusion modes were used to investigate mass transfer

of NaCl and Fluorescein-Na. Known parameters are given as: A = 2.2 × 10^{-12} m Pa^{-1} s^{-1} [3], R = 8.314 J K^{-1} mol^{-1}, T = 298 K, ρ = 10^{-3} kg m^{-3}, η = 1 × 10^{-3} Pa·s. In addition, totally five dependent variables were achieved through simulations which are $\tilde{u}$, $\tilde{v}$, $\tilde{p}$, $\tilde{c}_1$ and $\tilde{c}_2$. The liner system solver UMFPACK was selected along with relative convergence tolerance of 10^{-6} and maximum iterations of 25. Mesh independence were also tested for all simulations. The computation processes were conducted on an Inter (R) Xeon (R) CPU E5-2643 0 @ 3.30 GHz, 128 GB random access memory computer.

4.4 Results and discussion

4.4.1 FO flow rate and FO efficiency

In this section, the calibration experiment data and the corresponding fitted function between volume flow rate shown by pump and actual volume flow rate are shown in Figure in Appendix C. All the later experiments were conducted based on this calibrated relationship.

Figure 4.4 shows relationships of FO flow rate Q_{FO} versus Re and FO efficiency η_{FO} versus Re. Good consistencies between numerical results and experimental results are observed from this figure for both FO flow rate and FO efficiency. In particular, the FO flow rate sharply rises with the growth of Re only at the region of 0 < Re < 1, which later increases slowly at the region of Re > 1. Correspondingly, with increasing the Re of tangential flow, the FO efficiency drops rapidly at the region of 0 < Re < 1 first and then afterwards gets closer and closer to zero. It is well known that the FO flux across the membrane is proportional to the concentration difference between two solutions at both

besides of the membrane. Since the DI water is used as FS, then the FO flux can be equivalently treated as only a function of DS concentration on the membrane surface. When there is no tangential flow, i.e., Re = 0, the DS is continuously diluted by the permeating DI water from the FS side which in turn slows down the FO process as well as the diluting process to the DS. Although the FO process getting more and more slowly due to the continuously diluted DS concentration on the membrane surface, it still goes on according to thermodynamics. However, once there is a tangential flow on the membrane surface at DS side, even with a small value, the diluted DS on the membrane surface will be refreshed and then the osmotic pressure will be dramatically enhanced and finally the FO flow rate increases substantially as shown at region of $0 < Re < 1$. Although both FO flow rate and tangential flow rate increase, the increment speed of the former is far lower than that of the latter. Therefore, the FO efficiency, according to the definition, decreases significantly at this region. With continuously increasing the tangential flow rate after Re = 1, since the ECP layer has been already compressed within a thin layer nearby the membrane surface, it only shrinks a little and thus the DS concentration on the membrane surface is only slightly increased at this Re region. Further elaborations about those variations of the ECP layer and the corresponding DS concentration on the membrane surface will be given in the following section. In this situation, the FO flow rate increases quite slowly and the FO efficiency almost approximates to zero.

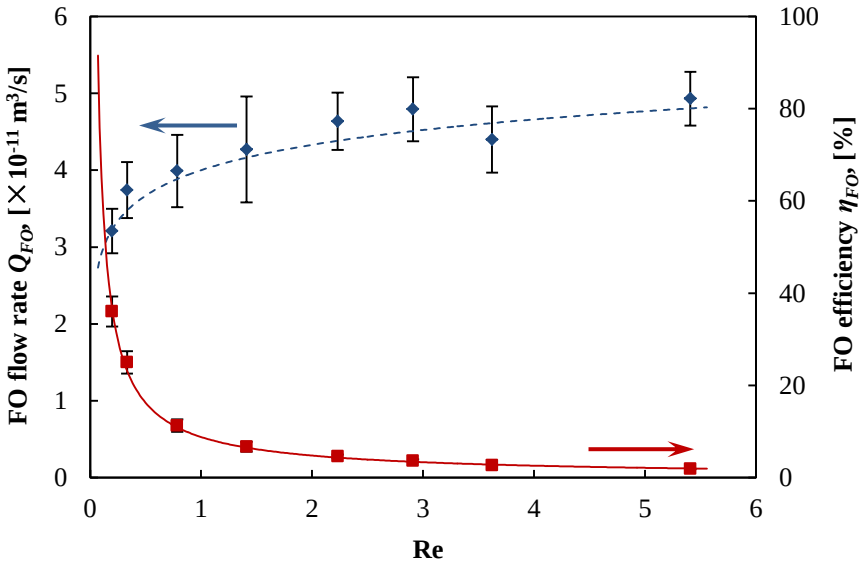

Figure 4.4 Relationship between FO flow rate Q_{FO} and Re shown as diamond symbols and dashed line and relationship between FO efficiency η_{FO} and Re shown as square symbols and solid line. The continuous curves represent numerical results and discrete points are obtained from experiment. Here, the FO efficiency is defined as the ratio of the FO flow rate across semipermeable membrane to the tangential volume flow rate, i.e., $\eta_{FO} = Q_{FO}/Q_t$.

Studies in this section provide worthy optimizing method to FO process. At low Re number ranging from 0 to 1, the ECP phenomenon predominately determines the FO flow rate due to the seriously reduced osmotic pressure within ECP layer. Although the FO flow rate is low at this Re number range, the FO efficiency is high. On the other hand, at high Re number larger than 1, the ECP is greatly reduced by high tangential flow rate. However, the enhancement in FO flow rate is not significant due to the little variation of ECP layer and membrane surface concentration. In this situation, if higher FO flow rate is wanted, methods such as reducing ICP or using high performance semipermeable membrane are preferred instead of simply increasing the tangential flow rate.

4.4.2 Region of CP layer

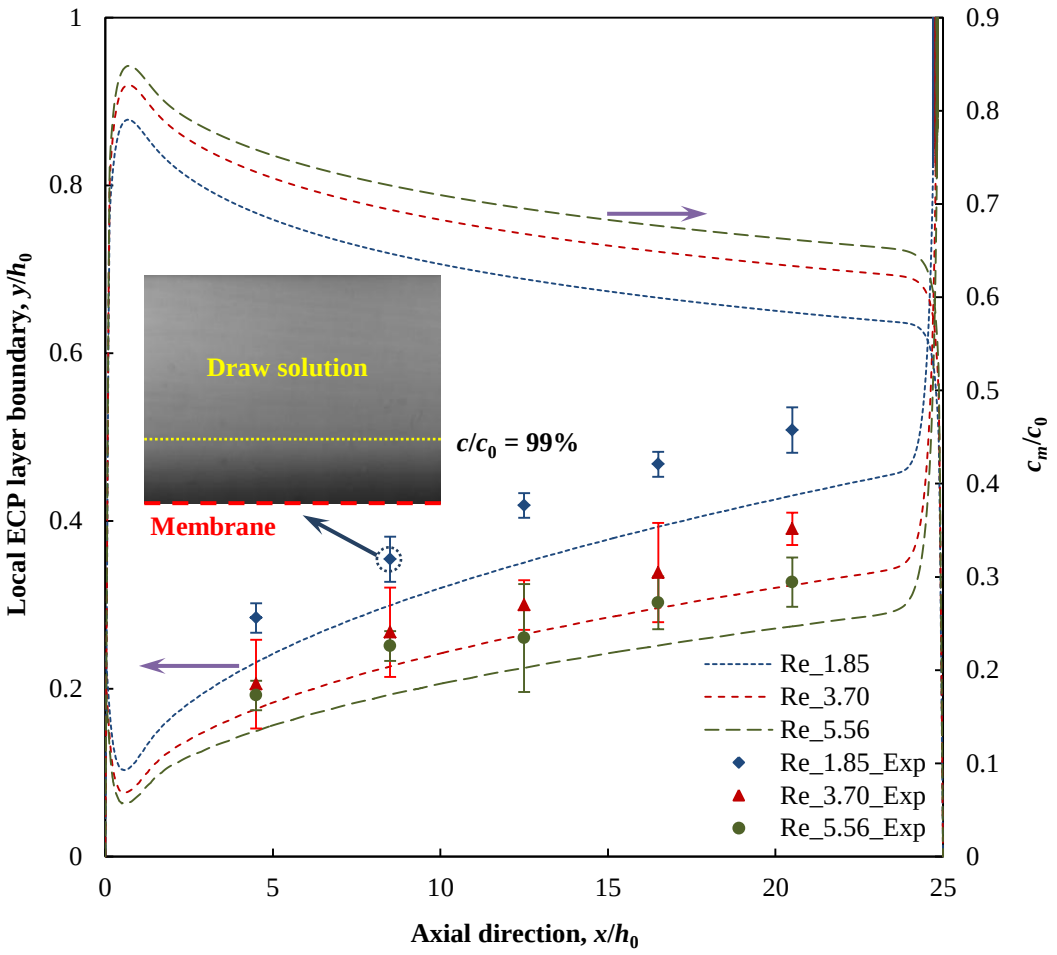

Figure 4.5 The discrete data and the continuous curves at the bottom part, separately obtained from experiment and numerical simulation, represent variation of the ECP layers with axial position at three different Re. The upper curves represent the numerically obtained relationship between dimensionless DS concentration on the membrane surface c_m/c_0 and axial position at three different Re.

In order to experimentally visualize and quantify the ECP phenomenon at the DS side, an indirect measurement method was utilized in this study as elaborated in Section 4.2. Here, it is reasonably assumed that the gray value of the captured image of DS

linearly increase with the variation of DS concentration. Generally, ECP layers at three tangential flow rates, 50 μl min^{-1}, 100 μl min^{-1} and 150 μl min^{-1}, were systematically investigated. The corresponding Reynolds numbers of the tangential flows are calculated as 1.85, 3.70 and 5.56, respectively. For each flow rate, five sets of experimental data are obtained along axial direction of DS channel which jointly constitute the ECP boundary as shown in Figure 4.5. This figure also shows three numerical profiles of the ECP boundary and other three numerical profiles of the dimensionless DS concentration on the membrane surface corresponding to the three aforementioned Reynolds numbers. Here, the boundary of the numerical ECP layer is defined as the location, the concentration of which is 99% of the bulk DS concentration.

It can be seen from Figure 4.5 that: (1) good consistence in variation trends between numerical ECP layers and experimental ECP layers proves that the convection-diffusion model used in this study not only provides well prediction to the FO process but also interprets the experimental results; (2) unlike normally assumed in film theory [86, 87, 131, 133-137], both numerical and experimental results show that the ECP layer varies along axial direction. This is mainly because that, the ECP layer at the forepart of DS channel is refreshed immediately by the injected fresh DS and thus compressed within a thinner region. Meanwhile, the fresh DS is also simultaneously diluted by the permeating DI water from the FS side along the axial direction. The ECP layer at the rear part of DS channel is refreshed by this diluted DS, which cannot effectively constrain the ECP within a thin region the same as that at the forepart. Therefore, the ECP layer is thin at the forepart but thick at the rear part; (3) high tangential flow rate gives rise to thin ECP layer and high membrane concentration. As well known that, the thickness of ECP layer

indicates the intensity of ECP phenomenon, i.e., the thicker the ECP layer is, the more serious the ECP phenomenon is. With increasing the tangential volume flow rate, faster mass refreshment of DS is induced by the increased convection flow so that the ECP can be reasonably reduced and thus ECP layer is thinner and membrane concentration is higher. In this situation, the FO flux is subsequently increased due to the enhanced membrane concentration. Consequently, it is reasonably concluded that high tangential flow rate gives rise to high FO flow rate, which also coincides with relationship shown in Figure 4.4; (4) less and less significant reduce in ECP is caused by equal increment in tangential flow rate. One reasonable prediction about the effects of tangential flow on ECP phenomena is that, there must be one critical Re_c above which no any decrease in thickness of ECP layer happens. Then the increase in FO flow rate with the growth of Re (as shown in Figure 4.4) is then level off due to the relatively stable CP layer.

The obtained results in this part investigate properties of ECP at different axial positions and different Reynolds numbers of tangential flow, which also provides a further detailed explanation to the relationship between the FO flow rate and the Reynolds number of tangential flow.

4.4.3 Osmotic pressure distribution within ECP layer

Theoretically, the osmotic pressure π is estimated as a linear decreasing function of the solution concentration according to Eq. (2.2). If the osmotic pressure is scaled by the osmotic pressure in the bulk π_0 with solution concentration of c_0, the dimensionless osmotic pressure distribution π/π_0 can be equivalently represented by the dimensionless concentration distribution c/c_0. Then the numerical and the experimental dimensionless osmotic pressure distributions within the DS channel at three different Reynolds numbers

smaller than Re_c are easily obtained as shown in Figure 4.6. From this figure it can be concluded that, (1) the ECP layer is compressed within a thinner and thinner region along with the rise of the tangential volume flow rate, which has been fully explained in Section 4.4.2; (2) the ECP phenomenon can be effectively reduced and thus the FO volume flow rate can be enhanced by increasing the tangential volume flow rate. Within the ECP layer, the concentration of the diluted DS indicates the intensity of ECP, i.e., the lower the concentration of the diluted DS is, the more serious the ECP phenomenon is. It is shown that the DS within the ECP layer is the most diluted at Re = 1.58 but the least diluted at Re = 5.56. In other words, the diluted DS within ECP layer can be timely and effectively refreshed by the tangential flow with high volume flow rate. In addition, due to the least diluted DS concentration within the ECP layer at Re = 5.56, the DS concentration on the membrane surface is the highest and the FO volume flow rate is thus greatly enhanced compared with that at Re = 1.58.

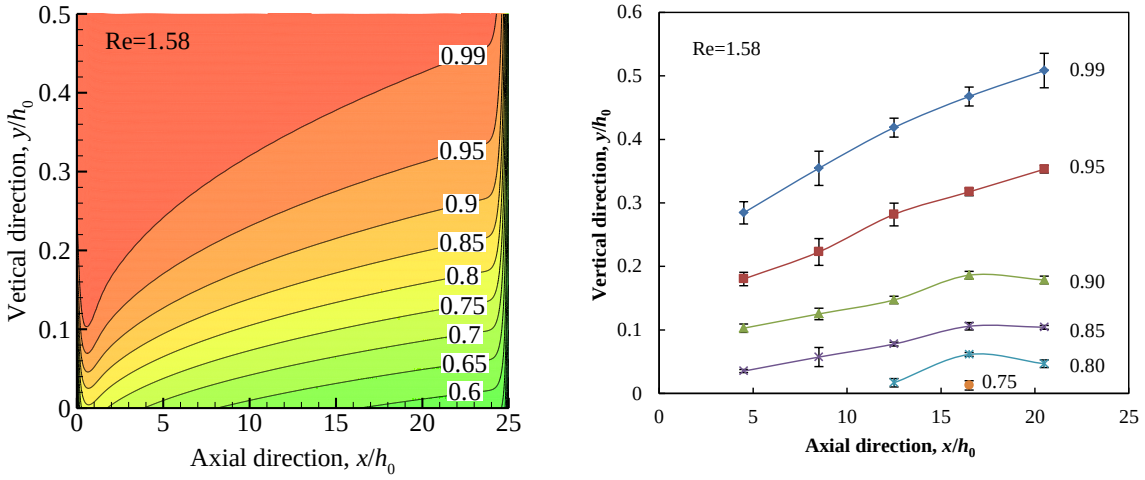

a **b**

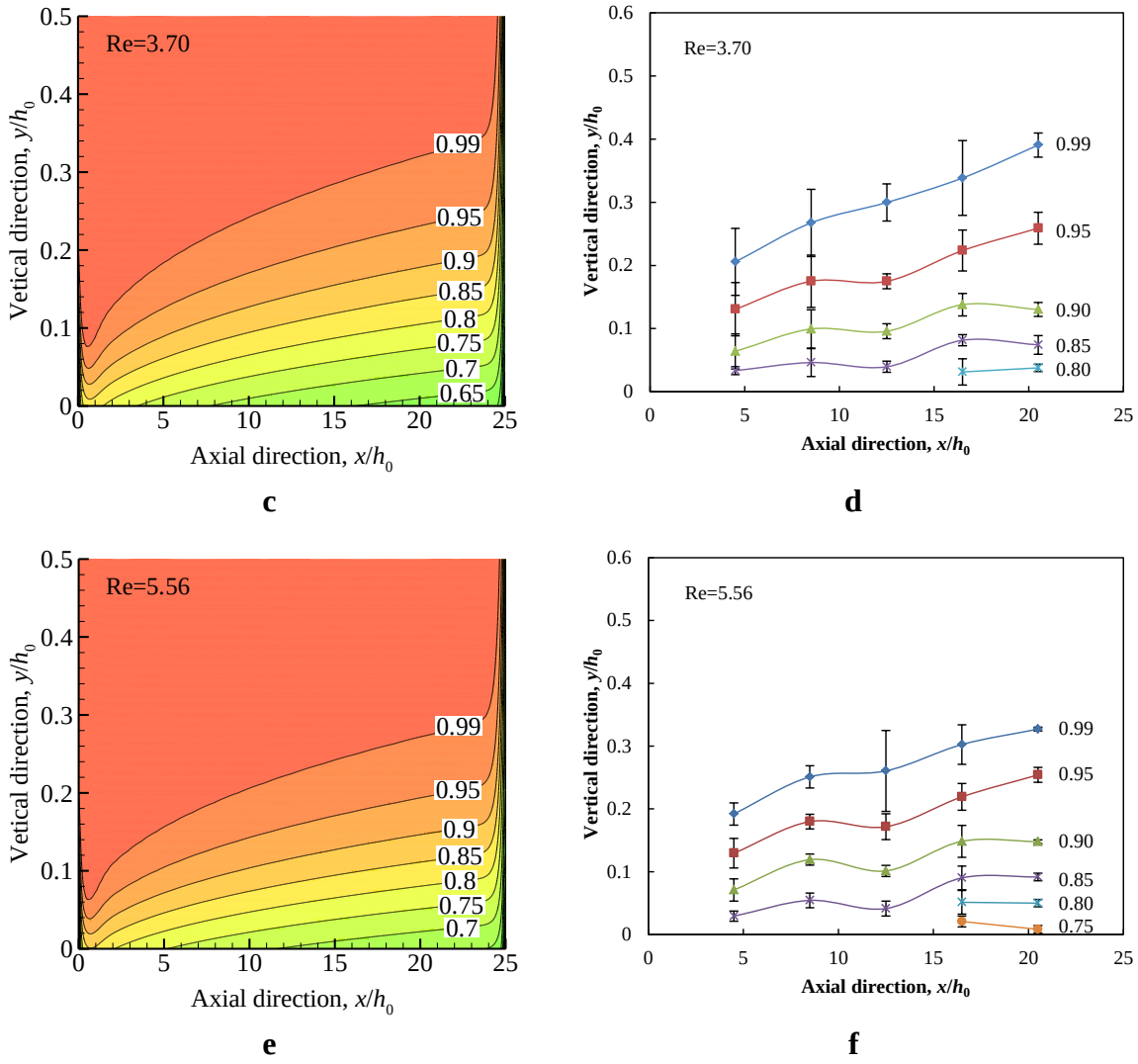

Figure 4.6 Dimensionless osmotic pressure distributions within the DS chamber at three different Reynolds numbers smaller than Re_c. For each tangential volume flow rate with a specific Reynolds number, the left figure is obtained from numerical analysis and the right figure is achieved from experimental data.

4.5 Summary

In summary, two main works are carried out in this chapter, experimental investigation and numerical simulation. For the experimental investigation, due to significant advantages of microtechnology compared with conventional macrotechnology, a micro-FO-device is utilized to systematically study the predominating ECP phenomenon in FO process. Specifically, two main experiments are carried out. One is to study the relationships between the FO flow rate and the tangential flow rate and between the FO efficiency and the tangential flow rate; the other one is to study the ECP layer variation at different axial locations and different tangential flow rates as well as the osmotic pressure distributions within the ECP layer. In order to interpret experimental results, a 2D numerical simulation about of steady FO process in a microchamber is conducted based on the convection-diffusion theory. Compared to the conventional 1D film theory with assumptions of no permeating flux variation and no flow field variation along axial direction, the convection-diffusion theory is reasonably selected to simulate FO process because it does not involve those assumptions mentioned above. The governing equations consist of the mass transfer equation, the momentum equation and the convection-diffusion equations. The osmosis process is reflected by the solvent permeating flux across the membrane into the DS region, which is set as an essential boundary condition in the simulation part. Main findings based on comparative study between numerical and experimental results are summarized as:

1. Compared to the commonly used film theory, the convection-diffusion theory can provide better interpretation and prediction to the FO process due to less assumptions set in this theory;

2. The thickness of the ECP layer and the solvent permeating flux vary along with the axial direction;
3. Higher tangential volume flow rate gives rise to thinner ECP layer and higher FO flow rate but lower FO efficiency;
4. The FO flow rate and the FO efficiency will be kept level off when the Reynolds number of tangential volume flow rate is beyond a critical value Re_c. In this situation, to obtain higher FO flow rate, methods such as reducing ICP or using high performance semipermeable membrane are desired.

In addition to these fundamental and optimization studies on the ECP phenomenon in FO process, the main contribution of this work is the experimental study based on microtechnology, especially the visualization and quantitative characterization of the ECP layer, which haven't been done by other researchers.

Nomenclature

A	Water permeability coefficient [m Pa^{-1} s^{-1}]
c	Concentration [M]
D	Salt diffusion coefficient [m^2 s^{-1}]
h_0	Height [m]
J_w	Solvent flux across the membrane [m^3 s^{-1} m^{-2}]
l_0	Length [m]
Pe	Péclet number [-]
Q	Volumetric flow rate [m^3 s^{-1}]
R	Universal gas constant [J K^{-1} mol^{-1}]
Re	Reynolds number [-]
T	Temperature [K]
u_0	Inlet velocity [m s^{-1}]
w_0	Width [m]

Greek symbols

η	Dynamic viscosity [kg m^{-1} s^{-1}] or [Pa s]
η_{FO}	FO efficiency [-]
ρ	Fluid density [kg m^{-3}]

Subscripts

0	Bulk solution

1	NaCl salt
2	Fluorescent salt
c	Critical value
FO	Forward osmosis
m	Membrane
T	Tangential flow

Chapter 5: Ion concentration polarization (IonCP) in pressure-driven electrokinetic (EK) flow through a capillary system

5.1 Introduction

As already elaborated in chapter of Literature review, the ion concentration polarization (IonCP), occurrence at the inlet and the outlet of the surface charged micro/nano-channel, significantly affects the output energy to the external electric load, especially for conditions of high surface charge densities, low solution concentrations and high applied pressure gradients [55, 56]. However, since the IonCP in pressure-driven EK process is not as significant as that in electroosmosis process due to the highly applied electric field, most of previous studies on IonCP in EK processes focus on the electroosmosis process while only a few pay attention to the IonCP in pressure-driven EK process. Although the other few studies considered the IonCP in the energy conversion process of the pressure-driven EK flow, they just emphasize on analyzing the effects of the channel and the fluid properties on the generated power and the corresponding energy conversion efficiency, as well as on the distributions of ion species, potentials, pressures and current densities inside the channel. As for the questions how the IonCP essentially affects the inner characteristics and the terminal characteristics of the surface charged

channel in pressure-driven EK process and what the relationships between those two kinds of characteristics are, they do not give sufficient and precise investigations or elaborations [29, 36, 67, 68]. However, if such a novel energy conversion technique is attempted to be put into real applications, the most pressing issue undoubtedly is to figure out those two questions mentioned above.

In this chapter, a comparison study based on numerical simulations is conducted to investigate the IonCP effects on the energy conversion performances of the pressure-driven EK flow through a capillary system, consisting of a single capillary connected with two big reservoirs at each end. In addition to investigating the inner characteristics of the energy conversion system, the terminal characteristics are also explored under various given conditions. Furthermore, the relationships between those two kinds of characteristics are reasonably built up through analyzing the various induced IonCPs.

5.2 Theoretical model and numerical simulation

5.2.1 Theoretical model for pressure-driven EK flow in a capillary system

5.2.1.1 Governing equations

As shown in Figure 5.1.a, we consider a pressure-driven EK flow through a glass capillary system, consisting of a single capillary connected with two big reservoirs at each end. This energy conversion system could be reasonably considered as a power source when it is connected with an external electric load through electrodes. Here, we simplify the mechanical process of the energy conversion system without considering the

chemical reactions and polarizations on electrodes. In fact, the charged capillary zoon is the real function element and the connected reservoirs are only side parts of the equivalent battery which exactly reduce the output power. The streaming potential in the traditional theory with a single capillary is the electric potential difference between two ends of capillary but in the theory adopted in this study with a capillary system is the electric potential difference between the two electrodes. In order to quantificationally obtain characteristics of such kind of power source, numerical simulations are conducted in this study based on the extracted theoretical model and the simplified two-dimensional (2D) geometry domain as shown in Figure 5.1.b. Meanwhile, the corresponding equivalent circuit diagram is accordingly shown in Figure 5.1.c.

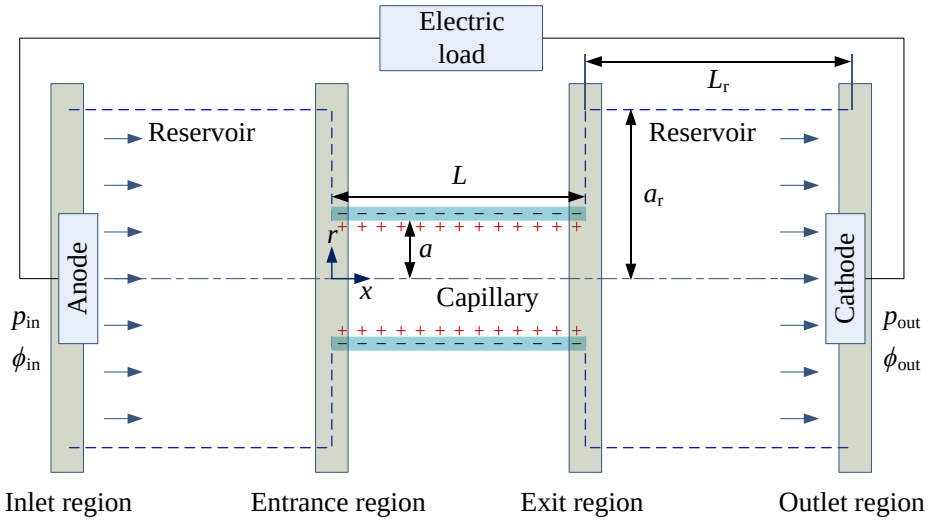

a

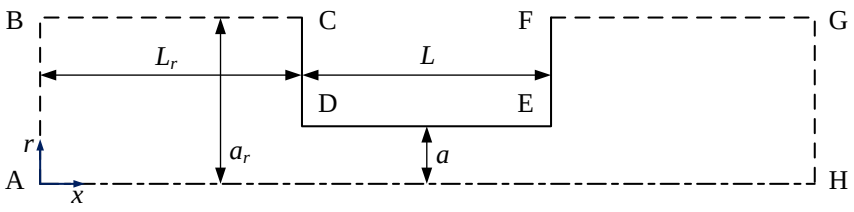

b

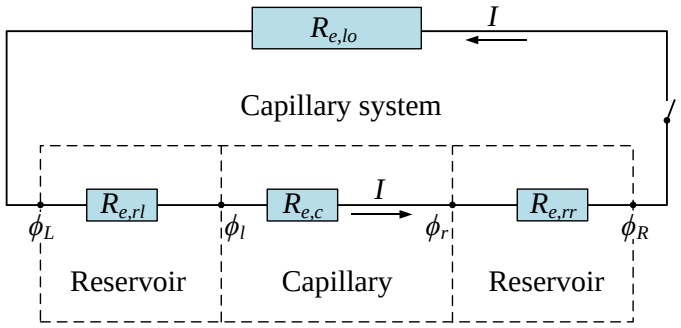

c

Figure 5.1 a. Schematic of a pressure-driven EK energy conversion system consisting of a negatively charged capillary and two identical reservoirs. In this figure, the entrance/exit region specially means the partial reservoir region and the immediately connected partial capillary region. The inlet/outlet region means the partial reservoir region far away from the capillary. The radius and the length of the charged capillary are represented by *a* and *L*, respectively. The radius and the length of the reservoir are represented by a_r and L_r, respectively. The cylindrical coordinate is employed in this capillary system with *r* and *x* respectively representing the radial direction and the axial direction. b. The extracted 2D axisymmetric domain corresponding to the capillary system adopted in current study. c. The equivalent circuit diagram corresponding to the real pressure-driven EK energy conversion system connected with an external electric circuit. $R_{e,rl}$, $R_{e,rr}$, $R_{e,c}$, and $R_{e,lo}$ are the electric resistances of left reservoir, right reservoir, capillary and external electric load, respectively. ϕ_L and ϕ_R are the potentials at the left and the right ends of the capillary system. ϕ_l, and ϕ_r are the potentials at the left end and the right ends of the capillary. *I* is the current though the electric circuit.

For pressure-driven steady laminar EK flow, the governing equations, including Poisson equation, conservation equations of cation and anion species, conservation equation of mass and Navier-Stokes equation, are given as follows [19]:

$$\nabla^2\phi = -\frac{F\sum z_k c_k}{\varepsilon_0 \varepsilon_r} \tag{5.1}$$

$$\nabla\bullet\left[c_k\mathbf{u} - D_k\nabla c_k - \frac{z_k F c_k D_k}{RT}\nabla\phi\right] = 0 \tag{5.2}$$

$$\nabla \bullet \mathbf{u} = 0 \tag{5.3}$$

$$\rho \mathbf{u} \bullet \nabla \mathbf{u} = -\nabla p + \eta \nabla^2 \mathbf{u} - F \nabla \psi \sum z_k c_k \tag{5.4}$$

where the subscript '*k*' represents the ion species including cation and anion species; *c*, *z*, *D* are the concentration, valence and diffusivity of ion specie, **u** is a velocity vector, $\phi(r, x)$ is the electric potential at a given location (r, x), ρ and η are fluid density and viscosity, *T* is temperature, *p* is pressure, *F* is the Faraday constant, *R* is the Universal gas constant, ε_0 and ε_r are the permittivity of vacuum and the dielectric constant of the fluid. The dimensionless analysis is employed in this study due to its outstanding universality property compared to the dimensional analysis. In order to develop a dimensionless model for the pressure-driven EK flow in a capillary system, the following reference groups are introduced: characteristic length: $L_{ref} = a$, reference concentration: $c_{ref} = c_0$, reference potential: $\phi_{ref} = \frac{RT}{F}$, reference electric strength: $E_{ref} = \frac{\phi_{ref}}{L_{ref}}$, reference velocity: $u_{ref} = \frac{\varepsilon_0 \varepsilon_r \phi_{ref}}{\eta} E_{ref}$, reference pressure: $p_{ref} = \eta \frac{u_{ref}}{L_{ref}}$, reference charge density: $\delta_{ref} = \varepsilon_0 \varepsilon_r \frac{\phi_{ref}}{L_{ref}}$, reference electric current density: $i_{ref} = F u_{ref} c_{ref}$, reference electric conductivity of solution: $\sigma_{ref} = \frac{L_{ref} i_{ref}}{\phi_{ref}}$, reference electric resistance of solution: $R_e = \frac{1}{\sigma_{ref} L_{ref}}$, Reynolds number $\mathrm{Re} = \frac{\rho u_{ref} L_{ref}}{\eta}$ and Péclet number $\mathrm{Pe}_k = \frac{u_{ref} L_{ref}}{D_k}$. Consequently, the governing equations above can be further deduced into the following dimensionless forms as:

$$\tilde{\nabla}^2\tilde{\phi} = -\frac{1}{2}(\kappa a)^2 \sum z_k \tilde{c}_k \tag{5.5}$$

$$\mathrm{Pe}_k\left(\tilde{\mathbf{u}}\bullet\tilde{\nabla}\tilde{c}_k\right) = \tilde{\nabla}^2\tilde{c}_k + \tilde{\nabla}\bullet\left(z_k\tilde{c}_k\tilde{\nabla}\tilde{\phi}\right) \tag{5.6}$$

$$\tilde{\nabla}\bullet\tilde{\mathbf{u}} = 0 \tag{5.7}$$

$$\mathrm{Re}\left(\tilde{\mathbf{u}}\bullet\tilde{\nabla}\tilde{\mathbf{u}}\right) = -\tilde{\nabla}\tilde{p} + \tilde{\nabla}^2\tilde{\mathbf{u}} - \frac{1}{2}(\kappa a)^2\tilde{\nabla}\tilde{\phi}\sum z_k\tilde{c}_k \tag{5.8}$$

where the inverse of Debye length κ given by $\kappa = \sqrt{\frac{2c_0F^2}{\varepsilon_0\varepsilon_r RT}}$. The overall term κa is defined as the inverse of the scaled Debye length, *K*. In addition to those dimensionless governing equations above, the dimensionless current density is given as:

$$\tilde{\mathbf{i}} = \tilde{\mathbf{u}}\sum z_k\tilde{c}_k - \sum z_k\frac{1}{Pe_k}\tilde{\nabla}\tilde{c}_k - \tilde{\nabla}\tilde{\phi}\sum z_k^2\frac{1}{\mathrm{Pe}_k}\tilde{c}_k \tag{5.9}$$

where the three terms on the right-hand side of the equation are the convection current density, the diffusion current density and the migration current density, respectively.

5.2.1.2 Boundary conditions

As shown in Figure 5.1.b, the 2D axisymmetric simulation domain, the fluid velocity components in radius direction and axial direction are *u* and *v*, respectively. All the boundary conditions are listed in Table 5.1. In this study, two kinds of electric status, the streaming potential $\tilde{\phi}_{str}$ status and the current-potential ($\tilde{I} - \Delta\tilde{\phi}$) status are going to be investigated, which are commonly restrained by the Poisson equation and the respective specific boundary conditions to this governing equation. When solving the streaming potential, the zero potential gradient at the outlet is always employed by other research works based on assumption that the downstream reservoir is large enough to allow the

ion concentration gradient to be zero [29, 36, 40, 55]. However, they do not even investigate how big the reservoir could be reasonably assumed as large enough. In this study, we directly use the boundary condition of zero output current at the outlet to obtain the streaming potential. Substantially, the method proposed in this study is more accurate compared to the previous one since it confirms to the physical definition of the streaming potential and has no limitation to the size of reservoirs. When calculating the current-potential relationships, the boundary condition at the outlet should be replaced by $\tilde{\phi} = \tilde{\phi}_0 \left(0 \le \tilde{\phi}_0 \le \tilde{\phi}_{str}\right)$.

Table 5.1 Boundary conditions corresponding to the model employed in this study for a capillary system.

BCs \ GEs	Poisson Eq.	Ion species conservation Eq.	Mass conservation Eq.	N-S Eq.
Channel wall (DE)	$\frac{\partial \tilde{\phi}}{\partial \tilde{r}} = -\tilde{\sigma}_s$	$\frac{\partial \tilde{c}_k}{\partial \tilde{r}} = 0$	$\tilde{u} = \tilde{v} = 0$	
Inlet (AB)	$\tilde{\phi} = 0$	$\tilde{c}_k = 1$	$\tilde{p} = \tilde{p}_0$	
Outlet (GH)	$\int \tilde{\mathbf{i}} = 0$	$\tilde{c}_k = 1$	$\tilde{p} = 0$	
Reservoir wall-I (CD, EF)	$\frac{\partial \tilde{\phi}}{\partial \tilde{x}} = 0$	$\frac{\partial \tilde{c}_k}{\partial \tilde{x}} = 0$	$\tilde{u} = \tilde{v} = 0$	
Reservoir wall-II (BC, FG)	$\frac{\partial \tilde{\phi}}{\partial \tilde{r}} = \frac{\partial \tilde{c}_k}{\partial \tilde{r}} = \frac{\partial \tilde{u}}{\partial \tilde{r}} = \frac{\partial \tilde{v}}{\partial \tilde{r}} = 0$			
Central axis (AH)				

All above is discussing about the case of energy conversion process in a capillary system which is relatively close to real EK system since it involves the connected reservoirs in the mathematical model. As already elaborated in the introduction section, the traditional theory studies the pressure-driven EK flow in a single capillary based on assumptions that the hydrodynamic flow in the capillary is fully developed Stokes flow and the ion concentration gradients are zero along the axial direction. However, once the

reservoirs exist, the ion concentration distributions at the entrance and the exit regions will be dramatically affected by the abrupt contraction and expansion flow fields and the surface charges, inducing ion depletion and enrichment, i.e., IonCPs. Those IonCP phenomena will in turn influence the output potential and current. Consequently, in order to figure out the energy conversion performance difference between the capillary system and the single capillary, numerical simulations based on traditional theory for the pressure-driven EK flow through the single capillary are also conducted in the following section.

5.2.2 Theoretical model for pressure-driven EK flow in a capillary

The extracted 2D geometry domain as shown in Figure 5.2 for studing the pressure-driven EK flow through a single capillary is similar with that throguh a capillary system. The difference is that, the fictional reservoirs in this section are only employed to constrain the bulk ion concentration as unit, and they are not involved in calculations of the flow field and the induced electric field strength.

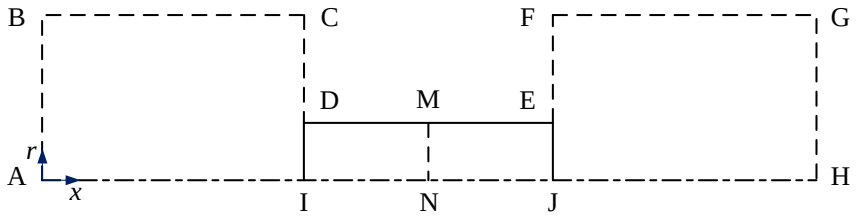

Figure 5.2 The extracted 2D axisymmetric domain corresponding to the single capillary adopted in the traditional theory for pressure-driven EK flow.

5.2.2.1 Governing equations

The traditional theory of the pressure-driven EK flow through a single capillary is developed based on following assumptions: (1) the potential $\tilde{\psi}$ due to the EDL is only a function of $\tilde{r}$, i.e., $\tilde{\psi}=\tilde{\psi}(\tilde{r})$; (2) the electric potential $\tilde{\phi}(\tilde{r},\tilde{x})$ at a given location $(\tilde{r},\tilde{x})$ is the superposition of the potential due to the induced potential gradient $\tilde{E}_{\tilde{x}}$ and the potential due to the capillary surface charge $\tilde{\psi}(\tilde{r})$, i.e., $\tilde{\phi}(\tilde{r},\tilde{x})=\tilde{\psi}(\tilde{r})-\tilde{x}\tilde{E}_{\tilde{x}}$; (3) there is no ion concentration gradient along the axial direction, i.e., $\partial\tilde{c}_k/\partial\tilde{x}=0$; (4) the EK flow in the capillary is regarded as steady, unidirectional and fully developed, i.e., Stokes flow. Then the governing equations are given as follows:

$$\tilde{\nabla}^2\tilde{\psi}=-\frac{1}{2}(\kappa a)^2\sum z_k\tilde{c}_k \tag{5.10}$$

$$0=\tilde{\nabla}^2\tilde{c}_k+\tilde{\nabla}\bullet\left(z_k\tilde{c}_k\tilde{\nabla}\tilde{\psi}\right) \tag{5.11}$$

$$\tilde{\nabla}\bullet\tilde{\mathbf{u}}=0 \tag{5.12}$$

$$0=-\tilde{\nabla}\tilde{p}+\tilde{\nabla}^2\tilde{\mathbf{u}}+\frac{1}{2}(\kappa a)^2\tilde{E}_{\tilde{x}}\sum z_k\tilde{c}_k \tag{5.13}$$

Since the ion concentration gradient along the axial direction is zero, the dimensionless current density is then simplified as:

$$\tilde{\mathbf{i}}=\tilde{\mathbf{u}}\sum z_k\tilde{c}_k+\tilde{E}_{\tilde{x}}\sum z_k^2\frac{1}{\mathrm{Pe}_k}\tilde{c}_k \tag{5.14}$$

The potential due to the capillary surface charge, $\tilde{\psi}(\tilde{r})$, and the ion concentration distributions, $\tilde{c}_k$, are firstly solved by Eq. (5.10) and Eq. (5.11), both of which act on the whole domain including the charged capillary and the fictional reservoirs. Then the unidirectional flow field and the induced electric field strength are solved by Eq. (5.12)

and Eq. (5.13) in cooperating with the pre-solved ion concentration distributions. The latter numerical step only acts on the charged capillary domain. Similarly, when the target is to solve the streaming potential, defined as $-L\tilde{E}_{Str}$, an additional governing equation that the overall current is zero, namely $\int \tilde{\mathbf{i}} = 0$, should also be included into the mathematical model. Once the induced streaming potential gradient is obtained, the current-potential curve can be thereby achieved by applying series of electric filed strengths, confirming to the relationship of $0 \le \tilde{E}_{\tilde{x}} \le \tilde{E}_{Str}$, to the volume force term of the Stokes equation.

5.2.2.2 Boundary conditions

As for the boundary conditions, since the traditional theory treats the pressure-driven EK flow in the single capillary as fully developed unidirectional flow, the first problem for numerical simulation to overcome is how to achieve such kind of flow through some simulation tricks. As known that, the entrance length is the length within a duct or tube after which the velocity profile is no longer varies in the flow direction. For laminar flow, the entrance length L_e is usually defined as $L_e \approx 0.12a\,\mathrm{Re}$ with a representing the channel radius [147]. In order to get a fully developed velocity profile within the capillary region, an entrance length is set at the inlet boundary to define a fictional entrance length outside the capillary domain. Here, the entrance length value must be not only greater than the aforementioned entrance length to fulfill the velocity profile requirement but also as low as possible to make sure the pressure is not significant affected by the extended fictional channel length outside of the capillary domain. As calculated, the Reynolds number here is about 4.7×10^{-4}, thus the scaled entrance length

$\tilde{L}_e$, i.e., L_e/a, should be at least larger than 0.12Re which is approximated as 0.6×10^{-4}. The same requirement to the exit length should also be fulfilled here. Based on numerical simulation results, the entrance and the exit lengths at the inlet and the outlet boundaries are finally determined as 2. In addition, the other boundary conditions are completely listed in Table 5.2.

Table 5.2 Boundary conditions corresponding to the model employed in traditional theory for a single capillary.

BCs \ GEs	Poisson Eq.	Ion species conservation Eq.	Mass conservation Eq.	Stokes Eq.
Channel wall (DE)	$\frac{\partial \tilde{\psi}}{\partial \tilde{r}} = -\tilde{\sigma}_s$	$\frac{\partial \tilde{c}_k}{\partial \tilde{r}} = 0$	$\tilde{u} = \tilde{v} = 0$	
Left end (AB)	Zero potential	$\tilde{c}_k = 1$	/	
Right end (GH)	Zero potential	$\tilde{c}_k = 1$		
Reservoir wall-I (CD, EF)	$\frac{\partial \tilde{\psi}}{\partial \tilde{x}} = 0$	$\frac{\partial \tilde{c}_k}{\partial \tilde{x}} = 0$		
Reservoir wall-II (BC, FG)	$\frac{\partial \tilde{\psi}}{\partial \tilde{r}} = \frac{\partial \tilde{c}_k}{\partial \tilde{r}} = 0$			
Central axis (AH)				
Inlet (DI)	/		$\tilde{p} = \tilde{p}_0$ and $\tilde{L}_{entrance} = 2$	
Outlet (EJ)			$\tilde{p} = 0$ and $\tilde{L}_{exit} = 2$	
Central axis (IJ)			$\frac{\partial \tilde{u}}{\partial \tilde{r}} = \frac{\partial \tilde{v}}{\partial \tilde{r}} = 0$	

5.2.3 Numerical procedure

In this work, both of those two models were solved based on numerical methods without any approximations or simplifications as adopted in traditional analytical solutions, which obviously makes the simulation results from both models much more comparable and reliable. Numerical simulations were performed by using a commercially

available finite element software, Comsol Multiphysics 4.3b (Comsol Inc., Sweden), with coupling four build-in modules. One Electrostatics module was used to solve electric potential distribution, two Transport of Dilute Species modules were used to solve the ion concentration distributions and one Laminar Flow module was used to solve the fluid velocity filed. The stationary solver with automatic highly non-linear (Newton) method was employed along with relative convergence tolerance of 10^{-6} and maximum iterations of 50. Mesh independence were also tested for all simulations. The computation processes were conducted on an Inter (R) Xeon (R) CPU E5-2643 0 @ 3.30 GHz, 128 GB random access memory computer.

5.3 Results and discussion

In this study, KCl electrolyte solution is employed as the working fluid to generate the EK flow. The temperature T, density ρ, viscosity η, and relative dielectric constant ε_r of the electrolyte solution are provided as 298 K, 10^3 kg m^{-3}, 10^{-3} Pa s, and 80, respectively. The valences of K^+ and Cl^- are 1 and –1, and the ionic diffusion coefficients are 1.957×10^{-9} m^2 s^{-1} and 2.032×10^{-9} m^2 s^{-1}, respectively. In addition, the other constant parameters involved in simulations are given as: $F = 9.649 \times 10^4$ C mol^{-1}, R = 8.314 J K^{-1} mol^{-1} and $\varepsilon_0 = 8.854 \times 10^{-12}$ C m^{-1} V^{-1}. Furthermore, the dimensionless sizes of the charged capillary and the connected reservoir are fixed at $a \times L = 1 \times 50$ and $a_r \times L_r = 50 \times 50$.

In order to verify the correctness of the proposed simulation methods for the pressure-driven EK flow within a capillary system, the streaming potentials obtained from the present simulation method and the previously reported simulation method [55]

are compared as shown in Figure 5.3. All simulation conditions for both simulation methods are same except the boundary condition at the outlet for Poisson equation. Particularly, the potential gradient at the outlet is set as zero for the previously reported simulation method, while the current at the outlet is set as zero for the current simulation method. Compared to the previous simulation method, the advantage of the current simulation method is that it has no limitation on the reservoir sizes and thus possesses higher general applicability. This figure shows that, the streaming potentials obtained from both simulation methods always agree with each other under various given conditions. Therefore, it is reasonably concluded that the simulation method proposed in this study could provide valid and correct numerical predictions to the pressure driven EK flow.

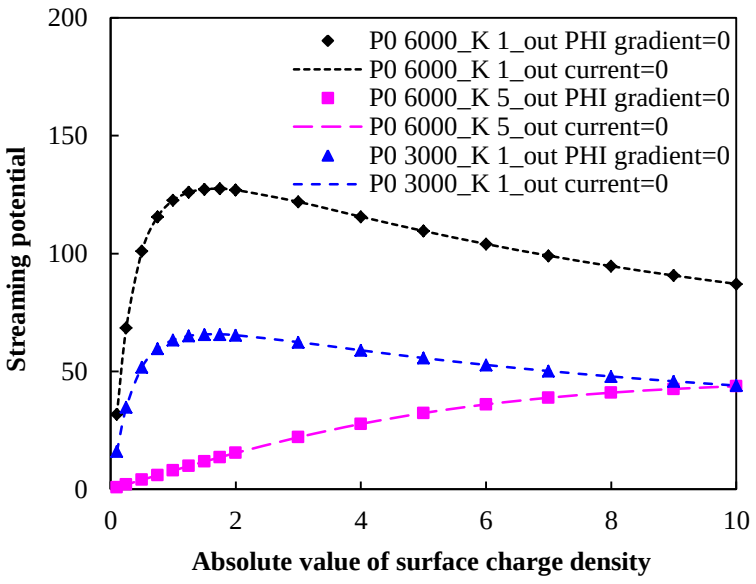

Figure 5.3 Comparison between the streaming potentials obtained from the present simulation method and the previously reported simulation method [55].

Based on the verified numerical method, energy conversion processes of the pressure driven EK flow through a capillary system and through a single capillary are comparatively studied in this section. Inner characteristics of the capillary system are investigated in the first subsection, including the distributions of the induced potentials, the ion species and the electric conductivities. As a kind of novel power source, studies on terminal characteristics, mainly including the overall electric resistances, the streaming potentials (i.e., open-circuit potentials), the maximum streaming currents, as well as the current-potential curves, under different operation conditions obviously are the most essential aspects since those terminal characteristics pave the way for real applications. Therefore, the terminal characteristics of both the capillary system and the single capillary are comparatively studied in the following three subsections. Meanwhile, the relationships between the inner and the terminal characteristics of a capillary system are also simultaneously investigated through analyzing the various induced IonCPs.

5.3.1 Distributions of potential, ion species and electric conductivity

In order to make clear what essentially happen behind the non-linear property of the current-potential curves for a capillary system, inner distributions of the induced potentials, the ion species and the electric conductivities at the zero potential status, the zero current status and the intermediate status should be investigated first. As simulated in this study, under given conditions of surface charge density of –6, Debye length of 1 and applied pressure of 6000, the streaming potential is numerically calculated as 104.06. The maximum streaming current is obtained when the output potential equals zero. In

addition to these two statuses, an intermediate status with an output potential of 52.03 in between 0 and 104.06 is also investigated. The distributions of the induced potentials, the ion species and the electric conductivities at those three statuses mentioned above are summarized as shown in Figure 5.4.

It is seen from the potential distributions as shown in Figure 5.4.a-d that, at low output potential such as 0 or 52.03, the potential within the capillary system decreases sharply to a negative value at the entrance region. This is because that, at this region, the absolute value of the potential due to the negative surface charge $\tilde{\sigma}_s$ is larger than that of the induced potential here. In addition, the potential variations within the reservoirs are relatively smaller compared to that within the charged channel. Furthermore, the potential within the charged channel almost linearly increases with increasing the axial position.

Parameter / Status of	Potential $\tilde{\phi}$	Net charge $\sum z_k \tilde{c}_k$	Electric conductivity $\tilde{\sigma} = \sum z_k^2 \frac{1}{Pe_k} \tilde{c}_k$
Zero potential (0)	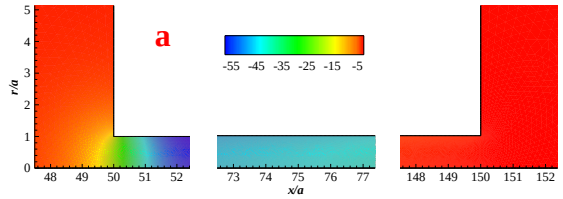	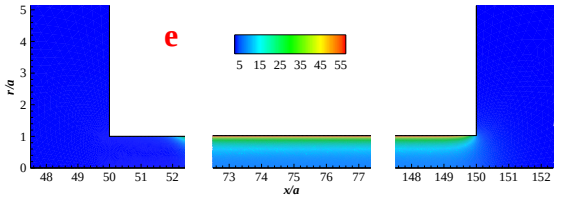	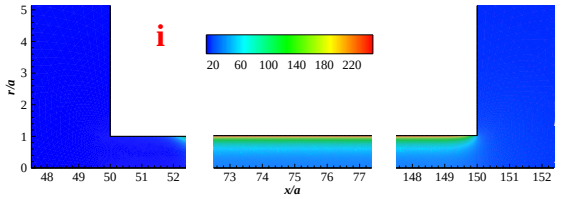
Intermediate potential (52.03)	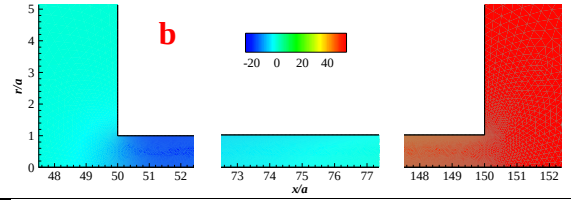	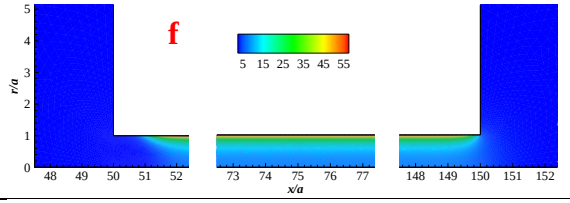	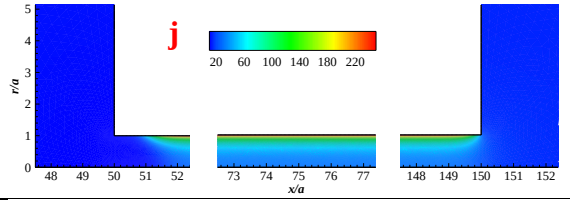
Streaming Potential (104.06)	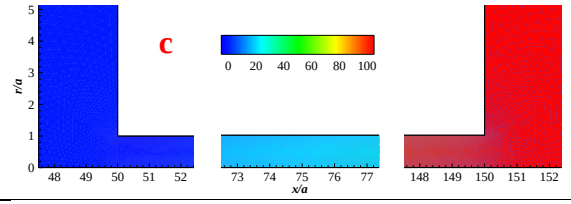	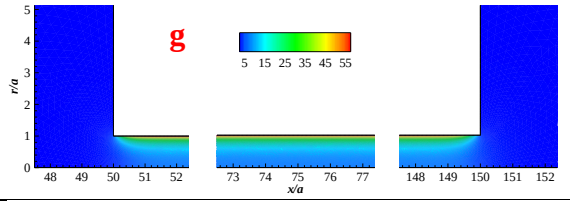	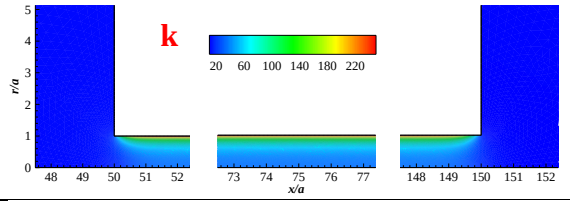
Distribution along central axis	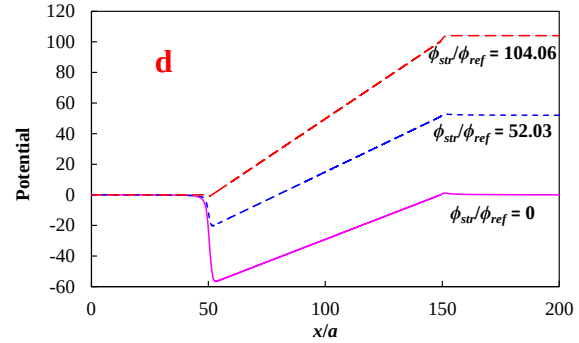	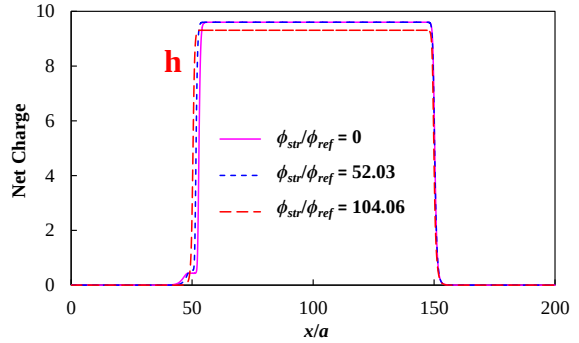	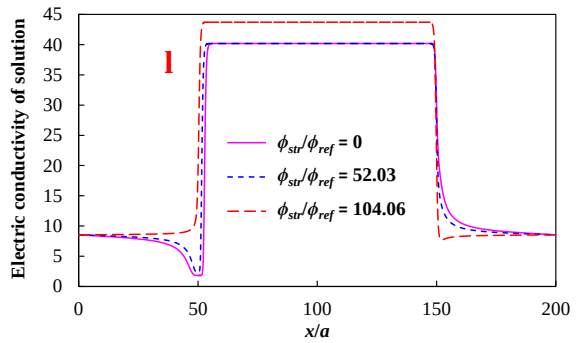

Figure 5.4 Distributions of the induced potentials, the net charges and the electric conductivities in the capillary system under given conditions of $\tilde{\sigma}_s$ = –6, K = 1 and $\tilde{p}_0$ = 6000.

In order to study the current property of this battery system, the component factors, including the net charge distribution and the electric conductivity distribution should be investigated first. It is because that, according to Eq. (5.9), the term of net charge is related with the convection current density and the term of electric conductivity is related with the migration current density. There is also a current term in Eq. (5.9) named as diffusion current density. However, the effects of this term to the overall current can be reasonably neglected since, according to both the surface distributions and the axial distribution of net charge as shown in Figure 5.4.e-h, there is almost no net charge gradient along axial direction except the entrance and the exit regions. Besides, it also shows that the net charges within the charged channel are much higher than that in reservoirs, and for a certain pressure, the net charges within the charged channel perform quite close with each other at any output potential. Those findings prove that the net charge distribution is mainly influenced by the surface charge rather than the induced output potential.

For the investigation of the electric conductivity as shown in Figure 5.4.i-l, since it is much related to concentrations of all ion species rather than concentration of the single ion species or the net charge, concentration distributions of cations and anions are also provided here as shown in Figure 5.5 to facilitate the conductivity analyses. The ion concentration distributions reveal that, although slightly ion enrichment and depletion appear at the entrance and the exit regions for open-circuit status, significant ion depletion and enrichment happen at the entrance and the exit regions for almost all other closed-circuit status. Particularly, the lower the output potential is, the more serious the IonCP is. All distributions of net charge concentration, ion species concentration and

conductivity clearly show that, the distributions of conductivity share the similar trends with that of electroneutral solution in the reservoir regions but another kind of similar trends with that of the net charge in the main capillary region. This is mainly because that, compared to the net charge concentration in the reservoir region, the conductivity is almost only sensitive to the overwhelming electroneutral solution concentration. However, in the capillary region, the sharply increased concentration of net charge, appearing in positive status to balance the negative surface charges, contributes the most to the greatly increased conductivities compared to the electroneutral solution. Those distribution trends can be further concluded that, the conductivity is dominated by the electroneutral solution in the reservoir region and by the net charge in the capillary region.

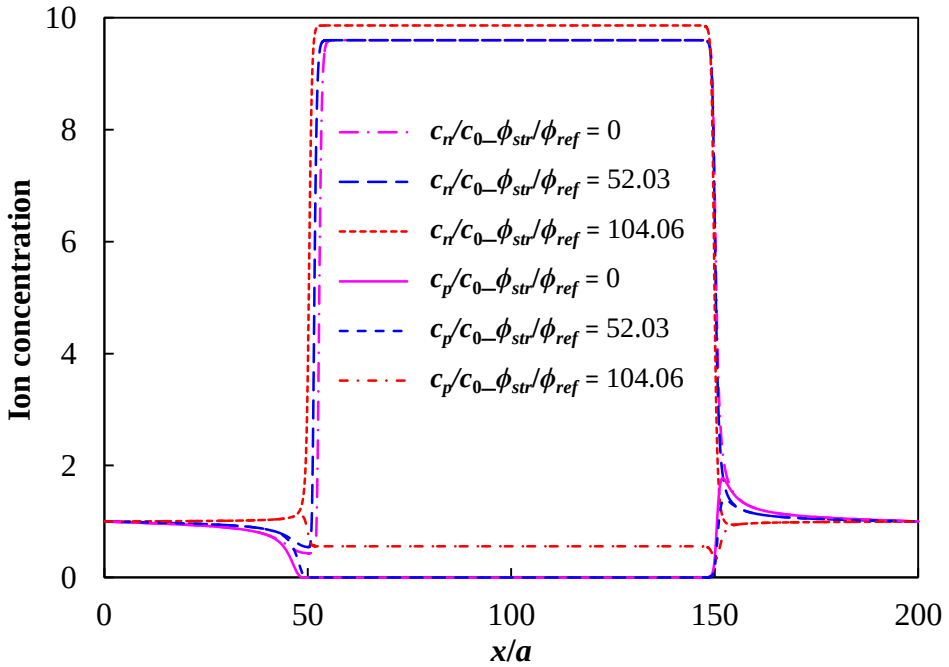

Figure 5.5 Distributions of positive and negative ions along central axis under conditions of $\tilde{\sigma}_s$ = –6, *K* = 1 and $\tilde{p}_0$ = 6000.

The results above are the commonly investigated aspects about the pressure-driven EK flow through a capillary system. In addition to those studies on the direct inner distributions, it is even meaningful to study the potential and the current supplied to the external electric circuit. Taking the output potential of 52.03 under conditions of $\tilde{\sigma}_s$ = –6, K = 1 and $\tilde{p}_0$ = 6000 as an example, the potential and the current distributions along axial direction are shown in Figure 5.6. Here, for a certain axial position, the potential is the average potential of that cross-section and the current is the area integration of the current density of that cross-section. It is seen from this figure that the average potential distribution along the axial direction is similar with the potential distribution along the central axis, and the overall current along the axial direction is constant although the current components, including the convection current, the diffusion current and the migration current, dramatically fluctuate at the entrance and the exit regions. For the reservoir regions, the convection current and the diffusion current are almost zero while the migration current has a comparatively higher positive value. Therefore, the overall current is dominated by the migration current in those regions. However, for the main charged capillary region, the magnitude of the forward convection current is larger than that of the backward conduction current, giving rise to an overall forward current. Generally, both the convection current and the migration current contribute the most to the overall current of this energy conversion system. Besides, it is also found that the potential variations within the reservoirs are fairly insignificant, which implies that the existing reservoirs itself almost have no effect on the output potential.

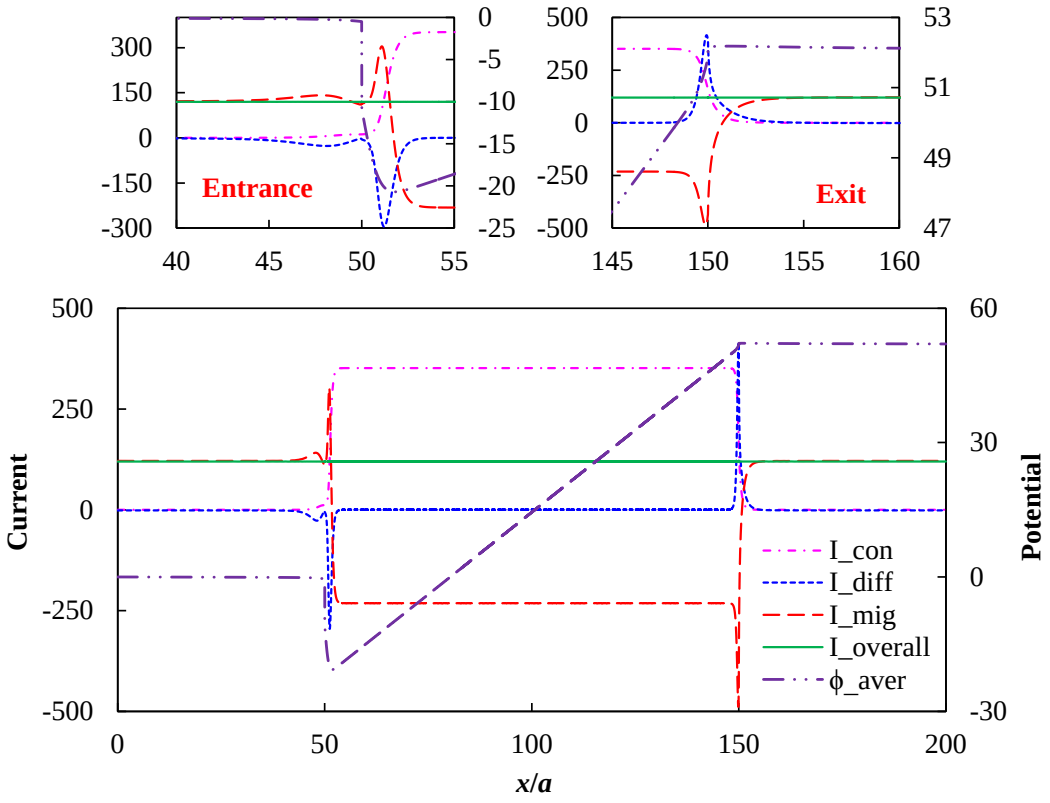

Figure 5.6 The potential and the current distributions along axial direction at the output potential of 52.03 under conditions of $\tilde{\sigma}_s$ = –6, *K* = 1 and $\tilde{p}_0$ = 6000. Here, for a certain axial position, the potential is the area-weighted average potential and the current is the area integration of the corresponding current density at that cross-section.

5.3.2 System resistance and non-linear property of current-potential curve

As evidently shown in Figure 5.4.l, the axial distributions of the electric conductivity of solution, significant variations appear in both capillary and reservoir regions along with increasing the output potential. Consequently, even larger overall electric resistance variations should be reasonably obtained by series of derivations and integrations to the electric conductivity over the whole domain of the capillary system. Meanwhile, the most

essential thing is that, the overall resistance directly influences the output potential. Therefore, it is important to investigate this property parameter, the overall resistance $\tilde{R}_{e,sys}$, to further evaluate the energy conversion system.

As the capillary system is equivalently treated as a battery, the overall electric resistance of this system $\tilde{R}_{e,sys}$ is composed of electric resistances of two reservoirs, $\tilde{R}_{e,rl}$ and $\tilde{R}_{e,rr}$, and electric resistance of charged channel, $\tilde{R}_{e,c}$. Since these three electric resistances are connected with each other in series, a relationship of electric resistance is obtained as:

$$\tilde{R}_{e,sys} = \tilde{R}_{e,rl} + \tilde{R}_{e,c} + \tilde{R}_{e,rr} \tag{5.15}$$

Although the whole system bears non-uniform conductivity, the charged capillary domain and the reservoir domains share the same integration element as shown in Figure 5.7.

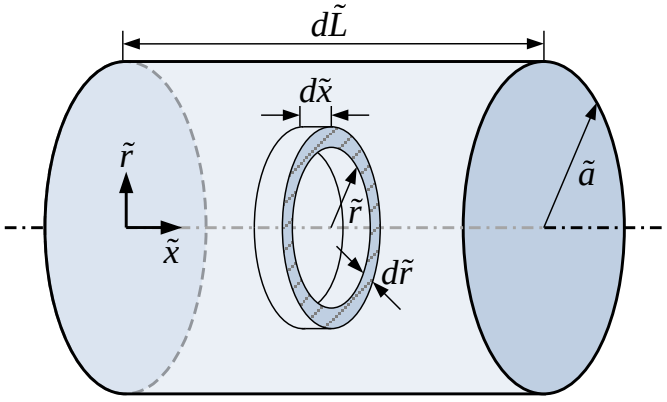

Figure 5.7 The integration element of a cylindrical volume filled with electrolyte solution.

It is assumed that the electric conductivity within the integral hollow-cylinder-shaped infinitesimal is constant. Then the electric resistance of one typical integration element is given as:

$$d\tilde{R}_{e,d\tilde{r}} = \frac{1}{\tilde{\sigma}} \frac{d\tilde{x}}{2\pi\tilde{r}d\tilde{r}} \tag{5.16}$$

For a given length of the infinitesimal hollow cylinder $d\tilde{x}$, it is assumed all the n concentric integration elements are connected with each other in parallel. Then, based on Ohm's law, the overall electric resistance of a slice of cylinder, $d\tilde{R}_e$, i.e., length resistance, calculated as:

$$\frac{1}{d\tilde{R}_e} = \int_n \frac{1}{d\tilde{R}_{e,d\tilde{r}}} = \int_0^{\tilde{a}} \frac{1}{\frac{1}{\tilde{\sigma}} \frac{d\tilde{x}}{2\pi\tilde{r}d\tilde{r}}} = \int_0^{\tilde{a}} \frac{\tilde{\sigma}2\pi\tilde{r}d\tilde{r}}{d\tilde{x}} = \frac{1}{d\tilde{x}} \int_0^{\tilde{a}} \tilde{\sigma}2\pi\tilde{r}d\tilde{r} \tag{5.17}$$

which is further deduced into the following form:

$$d\tilde{R}_e = \frac{d\tilde{x}}{\int_0^{\tilde{a}} \tilde{\sigma}2\pi\tilde{r}d\tilde{r}} \tag{5.18}$$

In addition, all the m slices of cylinder are reasonably assumed to be connected in series. Then the overall resistance for a complete cylinder is finally obtained as:

$$\tilde{R}_e = \int_m d\tilde{R}_e = \int_0^{\tilde{L}} \frac{d\tilde{x}}{\int_0^{\tilde{a}} \tilde{\sigma}2\pi\tilde{r}d\tilde{r}} = \int_0^{\tilde{L}} \frac{1}{\int_0^{\tilde{a}} \tilde{\sigma}2\pi\tilde{r}d\tilde{r}} d\tilde{x} \tag{5.19}$$

All resistances of the capillary and the reservoirs can be readily achieved by this equation. And then, the overall resistance of the capillary system is achieved by summing up all resistances of the capillary and the two reservoirs according to Eq. (5.15). As clear shown by Eq. (5.19), the resistance of a resistor is not only related with conductance per volume, but also related with the cross-section area and the length of the resistor. Particularly, it is in reversal proportions to the electric conductance and the cross-section

area but in direct proportion to the length. For the capillary system, although there is significant electric conductivity variation along the central axis as shown in Figure 5.4.l, the cross-section area of reservoir is extremely larger than that of the capillary, which ultimately gives rise to the almost zero length resistance in the reservoir regions and the relatively high length resistance in the capillary region as shown in Figure 5.8. Exactly, the calculation about the overall resistance shows that, much more than 99.5% of the electric resistance of the capillary system is from the electric resistance of the capillary for all cases. In addition, for the case of with IonCP, the length resistances in the capillary region are significantly enlarged at the two ends of the capillary but almost the same with that for the case of without IonCP in between the entrance and the exit regions. This is mainly because that, compared to the traditional theory with zero ion concentration gradient along axial direction, the existing reservoirs in a capillary system, cooperating with the capillary surface charges, greatly affect distributions of cations and anions, inducing non-zero ion concentration gradients along axial direction at the entrance and the exit regions, i.e., aforementioned IonCP phenomena. While, the ion concentrations for both cases are almost the same in between the entrance and the exit regions due to the identical surface charge density. Therefore, it is just those IonCP phenomena giving rise to the dramatic fluctuations of length resistance at the entrance and the exit regions, and the reservoir itself almost has no effect on the overall resistance. Although Chang and Yang have already realized that the existing reservoirs indeed have great influences on the generated powers and the energy conversion efficiencies, their analysis, based on many theoretical simplifications and approximations, simply attributed those influences to the resistances from reservoirs rather than the induced IonCPs within the entrance and

the exit regions [55]. However, this numerical study, without any simplification and approximation, thoroughly demonstrates that the induced IonCPs and the significant variations of the capillary resistance due to the IonCPs are the essential causes for the reduced energy conversion performance rather than the resistance from the reservoirs.

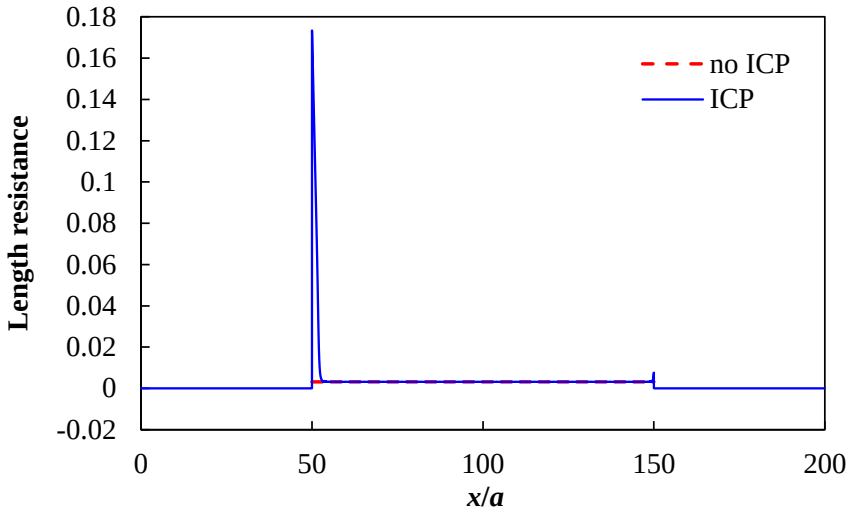

Figure 5.8 Variations of the length resistance along the axial direction calculated at the half of streaming potentials under common preconditions of $\tilde{\sigma}_s$ = –6, *K* = 1 and $\tilde{p}_0$ = 6000.

A summary about the overall electric resistance variations with the applied pressure $\tilde{p}_0$, the surface charge density $\tilde{\sigma}_s$ and the inversed Debye length *K* are shown in Figure 5.9.a-c. All these figures has a common feature that, the overall resistance of the capillary system increases with decreasing the output potential and reaches the maximum value when the output potential is zero. From the zero output current status to the zero output potential status, more and more significant IonCP phenomena happen as shown in Figure 5.5, specially, ion solution depletion at the entrance region and ion enrichment at the exit region. As already proved in last paragraph, the extent of IonCP phenomenon determines

the positive deviation degree of the length resistance. Therefore, the decreasing output potential gives rise to higher and higher deviation of length resistance and thus creates ascending overall electric resistance. Due to those resistance variations, the corresponding current-potential curves are also simultaneously affected.

The overall resistances and the corresponding current-potential curves for both cases of with IonCP and without IonCP are fully exhibited in Figure 5.9.d-l under different conditions of various $\tilde{p}_0$, various $\tilde{\sigma}_s$ and various *K*. All those figures are also share other common features that, for the case of without IonCP phenomena, i.e., traditional theory with only a single capillary domain, the overall resistances for all conditions are stable at a certain value no matter how the output potential changes and the corresponding current-potential curves linearly vary with the output potential; however, for the case of with IonCP phenomena, i.e., theory provided in this study with a capillary and two connected reservoirs, the overall resistances increase and the corresponding current-potential curves non-linearly increase with decreasing the output potential. The essential reason for those findings is that, according to Eq. (5.19), the overall electric resistance is a function of concentrations of ion species and geometry. For a given geometry with a certain surface charge density, the distributions of all ion species within the domain are invariable for the case of without IonCP phenomenon but significantly influenced by the varying output potential for the case of with IonCP phenomenon, especially at the entrance and the exit regions. Therefore, with decreasing the output potential, the overall resistances are stable at a certain value for the case of without IonCP but increase for the case of with IonCP. As for the current-potential curves, it is necessary to look back to the current expressions. For the case of a single capillary, the current, given by Eq. (5.14), is always a linear

function of the output potential. However, for the case of a capillary system, the current, given by Eq. (5.9), is a complex function of output potential since both the ion concentration distributions and the velocity field are also directly restrained by the varying output potential. But on the whole, the decreasing output potential definitely gives rise to more serious IonCPs, which more significantly hinders the current flux, inducing a much lower output current compared to that of the traditional theory.

In addition to the common features elaborated above, the particular effects of each parameter on the resistance and the current-potential curve are also explored as follows. The pressure effect on the overall electric resistance is shown in Figure 5.9.a and on the current-potential curves for selected $\tilde{p}_0$ of 10, 3000 and 6000 are shown in Figure 5.9.d-f. It is observed that, under conditions of a given $\tilde{\sigma}_s$ of –6 and a given K of 1, the higher the applied pressure is, the larger the resistance variation is. It is because that, with increasing the applied pressure from 10 to 6000, the velocity fields at the entrance and the exit regions also get more dramatic variations, which, in turn, expand the IonCP regions. Those anabatic IonCP regions will make ion species passing through capillary system even harder, giving rise to larger variation of the overall resistance and reduced output current.

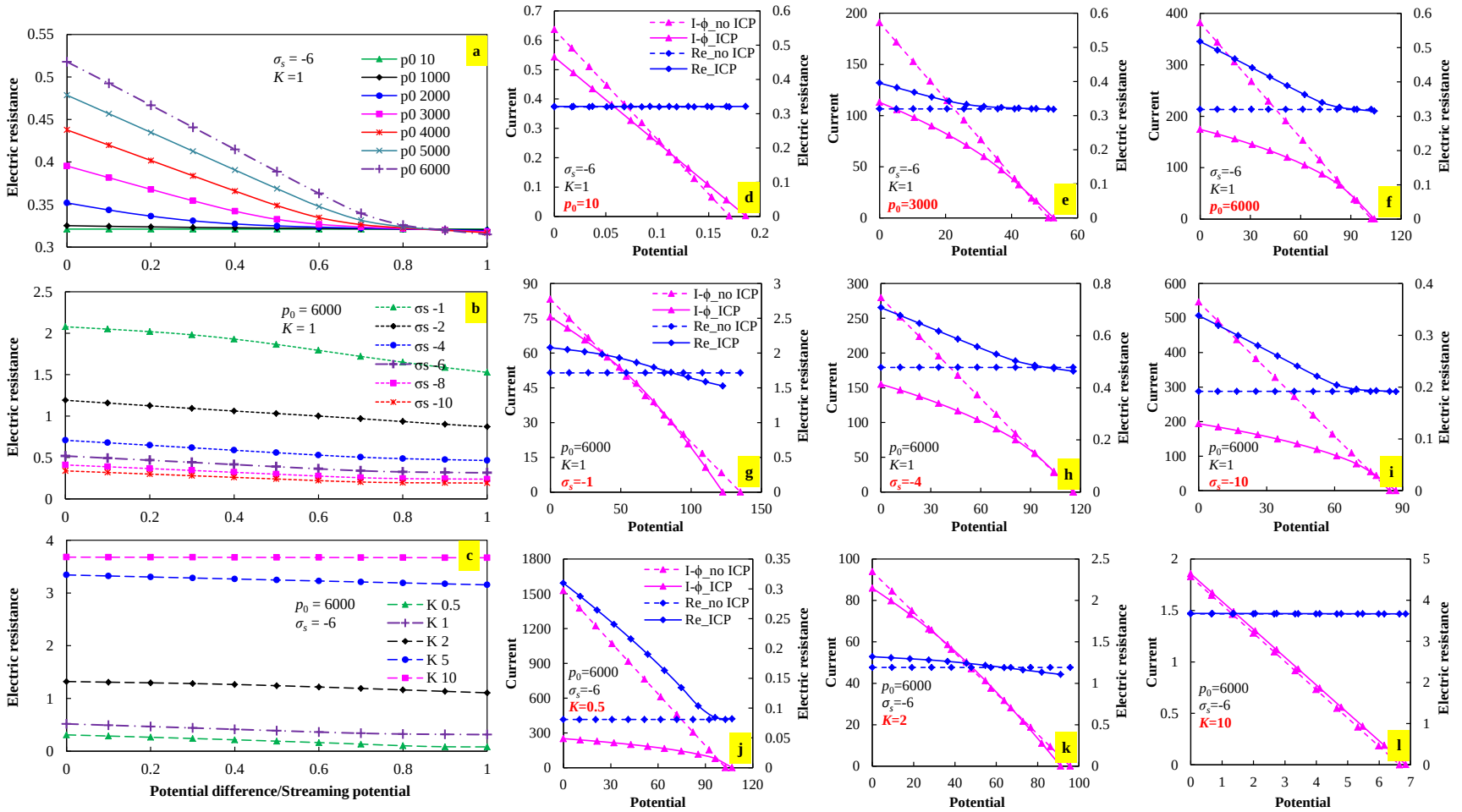

Figure 5.9 Variations of the overall electric resistance with the applied pressure $\tilde{p}_0$ (a), the surface charge density $\tilde{\sigma}_s$ (b) and the inversed Debye length *K* (c) for a capillary system. Variations of the overall resistance and the corresponding current-potential curve under different conditions of various $\tilde{p}_0$ (d-f), $\tilde{\sigma}_s$ (g-i) and *K* (j-l).

The surface charge density effect on the overall electric resistance is shown in Figure 5.9.b. It is observed that, not like the pressure effect with great variations in the overall resistance, the varying surface charge density obviously influence the overall level of the resistance at conditions of a given $\tilde{p}_0$ of 6000 and a given *K* of 1. Particularly, the overall resistance becomes less and less along with increasing the absolute value of surface charge density and almost reaches a plateau when the surface charge density is beyond –10. As known that, the negatively charged capillary attracts cations and repels anions, generating an overall positively charged space near the surface. Obviously, compared to the case of capillary with small absolute value of surface charge density, more ions, including both cations and anions, accumulate near the capillary surface with large absolute value of surface charge density to counterbalance the surface charges, which gives rise to higher solution conductivity and ultimately leads to lower overall electric resistance. The surface charge density effect on the current-potential curves at three selected surface charge densities of –1, –4 and –10 are shown in Figure 5.9.g-i. Although the overall resistance at lower absolute value of surface charge density is generally higher than that at higher absolute value of surface charge density, the capillary with higher absolute value of surface charge density acts much more like a unipolar of cations which greatly facilitates the passage of cations but hinders the anions passing through. Therefore, much more serious IonCP phenomena will happen at the entrance and the exit regions of capillary with higher absolute value of surface charge density, which, as already proved, will ultimately generate larger variation of overall resistance, leading to much more serious non-linear curves.

Finally, at conditions of a given $\tilde{p}_0$ of 6000 and a given $\tilde{\sigma}_s$ of –6, the inversed Debye length effect on the overall electric resistance is shown in Figure 5.9.c and on the current-potential curves for selected *K* of 0.5, 2 and 10 are shown in Figure 5.9.j-l. Along with increasing the *K* from 0.5 to 10, the variations of the overall resistance becomes smaller and smaller, and the overall level of resistance is higher and higher. At low *K*, taking $K = 0.5$ as an example, the EDL significantly overlaps within the charged capillary, generating a unipolar of cations. In this situation, more and more serious IonCP phenomena happen with the descending output potential, leading to larger variation of the overall resistance. Therefore, the corresponding current-curve becomes seriously non-linear as shown in Figure 5.9.j. On the contrary, at high *K*, taking $K = 10$ as an example, the capillary almost has no capacity of selecting ions since the EDL, located just near by the capillary surface, is quite thin. All cations and anions can easily pass through this capillary, inducing almost no IonCP phenomena at the entrance and the exit regions. Therefore, the overall resistance of the capillary system maintains almost constant for all output potentials and an almost linear current-potential curve is thus created at $K = 10$.

In general, the applied pressure mainly affects the variation amplitude of the overall resistance, the surface charge density mainly affects the fiducial value of the overall resistance and the EDL thickness affects the overall resistance on both aspects. And the non-linear property of current-potential curve wholly dependents on the variation amplitude of the overall resistance, specially, larger variation of overall resistance gives rise to larger extent of non-linear curves.

According to the traditional theory with linear current-potential curve, the maximum output power occurs at the half of the streaming potential where the current is just the

half of the maximum streaming current [36, 55]. However, it is another story for the capillary system with IonCP phenomena. As afore elaborated, significant non-linear current-potential curves are found within the capillary system, especially for conditions of high applied pressure, high surface charge density and small inversed Debye length. Thus, it is hard to theoretically predict the maximum output power for the capillary system with complex IonCP phenomena. In the following two sections, in addition to the comparison studies on the streaming potential and the maximum streaming current, the comparison study on the maximum output power is also conducted to further investigate the performance properties of the pressure-driven EK flow though a single capillary and through a capillary system.

5.3.3 Effects of applied pressure

The effects of the applied pressure on terminal characteristics of the streaming potential, the maximum streaming current and the maximum power under the condition of $K = 1$ are respectively shown in Figure 5.10.a-c. Those figures also show comparisons between the cases of without IonCP and with IonCP. The detailed effects on each parameter are elaborated as follows.

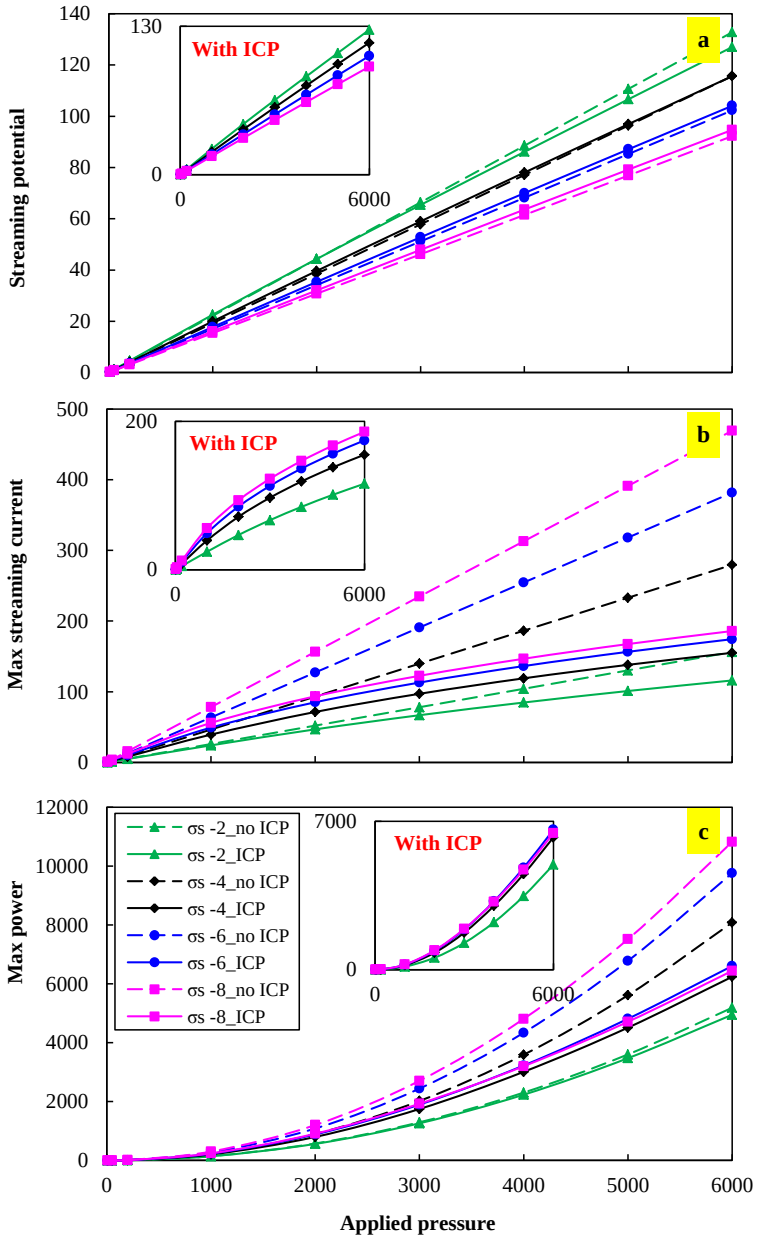

Figure 5.10 Effects of the applied pressure on the streaming potential (a), the maximum current (b) and the maximum power (c) under the condition of K = 1.

Effects of the applied pressure on the streaming potential shown in Figure 5.10.a reveal that, the streaming potentials for both cases of without IonCP and with IonCP at a given K of 1 perform quite close with each other and almost linearly increase with the ascending applied pressure under any surface charge density. It is essentially because

that, the streaming potential is achieved at the condition of zero output current. In this situation, the streaming potential is a function of axial velocity and ion concentrations. As for the case of without IonCP, since the ion concentration distributions for a given surface charge density do not vary at any pressure, the electric body force imposed by the free ions on the velocity field also does not vary with applied pressure and thus the velocity field should be a linear rise function of the ascending applied pressure. Consequently, the streaming potential linearly increases with increasing the applied pressure for the case of without IonCP at any given surface charge density. In addition, at zero current status, only slightly IonCPs happen within the capillary system as shown in Figure 5.5, which gives rise to the relatively similar trends with that for the case of without IonCP, i.e., almost linear variation of the streaming potential with the applied pressure.

Effects of the applied pressure on the maximum streaming current as shown in Figure 5.9.b display that, the streaming currents for the case of without IonCP linearly increases with increasing the applied pressure, and the streaming currents for the case of with IonCP also increase with increasing the applied pressure, but with slower speed. It is essentially on account of that the maximum streaming current is achieved when the output potential is zero. According to Eq. (5.9) and Eq. (5.14), the migration current, in the opposite direction of the streaming current, is zero and thus the maximum streaming current is only function of concentrations of ion species and axial velocity. Concentrations of ion species under conditions of a given surface charge density and a given EDL thickness are not influenced by the varying flow field for the case of a single capillary, but significantly affected for the case of a capillary system. Particularly, the

higher the applied pressure is, the more serious the nonuniformity of the concentrations of ion species at the entrance and the exit regions is and thus the larger the negative effect on the current flux is. Consequently, the maximum streaming current for the case of a single capillary without IonCP effect is only a function of axial velocity, which linearly increases with the growth of the applied pressure. But for the case of a capillary system with IonCP effects, the maximum streaming current is indeed a complex function of the applied pressure, specifically, increasing with the growth of the applied pressure with a slower speed.

Effects of the applied pressure on the maximum output power as shown in Figure 5.10.c tell that, the maximum output powers for both cases at a certain surface charge density monotonously increase with the growth of the applied pressure but the speed is relatively low for the case of with IonCP. As predicted by traditional theory, the maximum output power increases with increasing the applied pressure in a parabolic speed since both the streaming potential and the maximum streaming current are linear increasing functions of the applied pressure and also the current-potential curve is linear. However, for the capillary system, although the maximum output power generally increases with increasing the applied pressure, more energy is also dissipated at the entrance and the exit regions due to the existing IonCPs. Therefore, the growth of the maximum output power with increasing the applied pressure for the case of with IonCP is relatively slower compared to that for the case of without IonCP.

5.3.4 Effects of surface charge density

The effects of the surface charge density on parameters including the streaming potential, the maximum streaming current and the maximum power under the condition

of $\tilde{p}_0$ = 6000 are respectively shown in Figure 5.11.a-c. Those figures also show the comparisons between the cases of without IonCP and with IonCP. One common feature is that, for both cases of without IonCP and with IonCP, the lower *K* always gives rise to higher performance. As known that, the inverse Debye length, *K*, defined as the ratio of the capillary radius to the EDL thickness, represents the distribution region of EDL. Meanwhile, at a given applied pressure, the general axial velocity profile of the cross-section of the capillary is much like a paraboloid, i.e., the velocity is highest at the center, but becomes smaller and smaller along with increasing the radius, and finally reaches zero at the capillary wall. For lower *K* such as *K* = 1, the positively charged EDL region fills in all the capillary space. As the *K* increases from 1, the EDL shrinks within a thinner and thinner region in the vicinity of the capillary surface. Although the space charge density within the EDL region for a given surface charge density becomes larger due to the thinner shrinking EDL, the velocity field there is smaller, giving rise to less contribution to the overall energy conversion process. Therefore, it is concluded that the lower *K* value always leads to higher energy conversion performance for both cases. The detailed effects on each parameter are elaborated as follows.

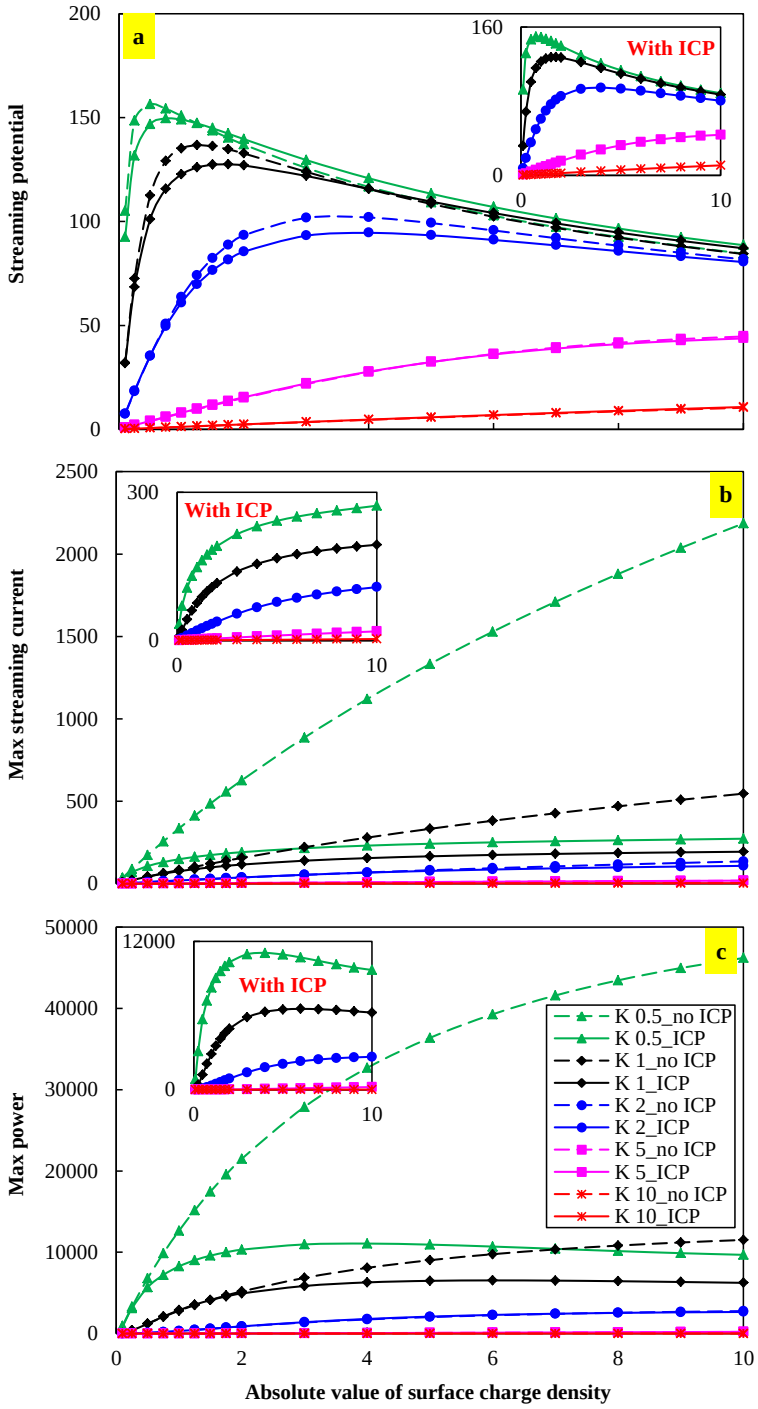

Figure 5.11 Effects of the surface charge density on the streaming potential (a), the maximum current (b) and the maximum power (c) under the condition of $\tilde{p}_0$ = 6000.

Effects of the surface charge density on the streaming potential as shown in Figure 5.11.a reveal that, with increasing the surface charge density, the streaming potentials for both cases of without IonCP and with IonCP at a given EDL thickness perform fairly close with each other, and both increase first and then decrease for smaller K such as 0.5, 1 or 2 but monotonously increase for larger K such as 5 or 10. The essential reason for all of those trends can be reasonably tracked back to the definition of streaming potential. As well known, the streaming potential is obtained when the overall output current is zero. In this case, the overall resistance of a capillary system at a given EDL thickness is relatively close with that of a single capillary for any given surface charges since the discrepancy of concentration distributions of ion species for both cases is not significant. Therefore, the variation of streaming potentials with surface charge density for both cases of without IonCP and with IonCP at a given EDL thickness performs quite close with each other. In addition, as already concluded, the diffusion current only has little effect on the overall current for the case of with IonCP and thus the streaming potential for this case, similar with that for the case of without IonCP, is almost only a function of velocity, net charge and conductance. Therefore, the variations of those three influencing factors with the changing surface charge density at a given applied pressure and a given EDL thickness are the essential causes to the variation trends of streaming potential. For the thick EDL, taking $K = 1$ as an example, both cations and anions co-exist within the overlapped EDL and the space within the capillary is positively charged everywhere. With increasing the surface charge density within the range of from 0 to 1.5, more cations are attracted and more anions are repelled, which gives rise to increments in both net charge and conductance. However, the increment in net charge is faster than that in

conductance which induced a faster increment in the streaming current term. Therefore, the streaming potential rises with the growth of the surface charge density when the surface charge density is lower than 1.5. When the surface charge density continuous increases after 1.5, most of the cations become more and more tightly attracted within the thin layer in the vicinity of the charged capillary surface by the electrostatic force, which indeed do not contribute to the streaming current as much as the case of before 1.5. But the conductance still increases as much as the case of before 1.5. Consequently, the induced streaming potential begins to decline after the surface charge density of 1.5. For the thin EDL, taking K = 10 as an example, the positively charged EDL region only accumulating within a thin layer in the vicinity of the capillary surface. With increasing the surface charge density from 0 to 10, the streaming current term is almost linearly increases but, compared to the variation of streaming current term, the electric conductivity only slightly increases. Therefore, the final streaming potential for higher K of 10 monotonously increases with the ascending surface charge density.

Effects of the surface charge density on the maximum streaming current as shown in Figure 5.11.b display that, at given applied pressure and EDL thickness, the maximum streaming currents for both cases increase with the increment of the surface charge density. The same, the reason for those variation trends should also be tracked back to the definition of the maximum streaming current which exactly is the convection current induced by the pressure-driven flow though a charged capillary at zero output potential. It is only a function of concentrations of ion species and axial velocity. At a given applied pressure, the flow field for capillary with any given surface charge density almost does not vary. In addition, for a given K, the increment in surface charge density always gives

rise to more net charges gathering in the EDL region and thus creates increased maximum streaming currents for both cases. However, with increasing the surface charge density, most of those increasing cations closely gather on the surface of the charged capillary due to the electrostatic force, contributing less to the increment of the maximum streaming current. Therefore, the increment speeds of the maximum streaming current with increasing the surface charge density are lower for both cases. As for the larger *K*, such as 2, 5 or 10, the entire EDL is constrained within a thin region near the capillary surface where the axial velocity is considerably small. Meanwhile, the negative effects of the IonCPs on the maximum streaming current for the case of with IonCP can also be reasonably neglected due to that both cations and anions can easily pass through the capillary system. Thus, maximum streaming currents for both cases are significantly small and perform quite close with each other. As for the smaller *K*, such as 0.5 or 1, the serious IonCPs at the entrance and the exit regions within a capillary system significantly reduce the increment of the maximum streaming current when increasing the surface charge density, inducing larger discrepancy of the maximum streaming currents between those two cases.

Effects of the surface charge density on the maximum output power as shown in Figure 5.11.c tell that, for the case of without IonCP at any *K*, the maximum output power always increases with the increment of surface charge density with a lower speed, especially for smaller *K*. This is because that, for a single capillary under a given applied pressure, although more effective cations are involved in the energy conversion process when increasing the surface charge density, more cations are closely attached on the capillary surface at the same time and thus contributes less to the output energy.

However, for the case of with IonCP, similar trend can only be found at higher K such as 2, 5 or 10. This is mainly due to that, at high K, only slight IonCPs happen within the capillary system, which makes the energy conversion process within a capillary system much similar with that within the single capillary. Therefore, the maximum output powers at higher K such as 2, 5 or 10 perform quite close with each other. For smaller K such as 0.5 or 1, the maximum output powers increase first and then decrease along with increasing the surface charge density. This is mainly attributed to the energy losses at the IonCP regions. Taking K = 0.5 as an example, more serious IonCP phenomena are induced by further increasing the surface charge density after $\tilde{\sigma}_s$ = –3, especially for relatively lower K and thus more energy is required there to overcome the increased resistant force at those regions. Finally, the maximum output power descends along with increasing the surface charge density.

5.4 Summary

A systematic comparison study was numerically conducted to investigate the IonCP effects on the energy conversion performances of the pressure-driven EK flow in a capillary system. The method of dimensionless analysis for both cases of with IonCP and without IonCP was adopted in this study since it is much more generic for a series of operation conditions fitting for a particular dimensionless relationship. The simulation process was improved by setting the output current rather than the output potential gradient as zero at the outlet when solving the streaming potential. In addition to the in-depth analysis on the inner characteristics, including distributions of the induced potentials, the ion species and the electric conductivities, investigations on the terminal

characteristics, mainly including the overall electric resistances, the streaming potentials (i.e., open-circuit potentials), the maximum streaming currents as well as the current-potential curves, are also conducted. Collectively, all the results and discussion provide comprehensive evaluation on the performance of the pressure-driven EK energy conversion system and, simultaneously, pave the way for further real applications. The main research findings are concluded as follows:

1. The existing reservoirs, together with the capillary surface charge, give rise to various IonCPs at the entrance and the exit regions within a capillary system;
2. For the case of with IonCP, the applied pressure $\tilde{p}_0$ mainly affects the variation amplitude of the overall resistance, the surface charge density $\tilde{\sigma}_s$ mainly affects the fiducial value of the overall resistance and the inverse Debye length *K* affects the overall resistance on both aspects. In addition, the non-linear property of current-potential curve wholly dependents on the variation amplitude of the overall resistance, specially, larger variation of overall resistance gives rise to significant non-linear curves;
3. The terminal characteristics, including the streaming potential, the maximum current and the maximum power, monotonously increase with the applied pressure $\tilde{p}_0$ but complicatedly vary with the surface charge density $\tilde{\sigma}_s$. In general, however, influencing factors, including the applied pressure $\tilde{p}_0$, the surface charge density $\tilde{\sigma}_s$ and the EDL thickness, with lager value give rise to much more serious IonCPs and thus induce more energies being consumed to overcome the negative effects from IonCPs, and finally lead to much more reduced energy conversion performance compared to the traditional theory without IonCPs;

4. It is those IonCPs that induce a series of discrepancies in the overall electric resistance, the streaming potential, the maximum streaming current and the maximum output power from the traditional theory results while the properties of reservoir almost have no effect on the terminal characteristics.

Nomenclature

a	Channel radius [m]
c_k	Concentration of the ion species k [M]
D_k	Diffusivity of ion species k [m^2 s^{-1}]
E	Streaming potential gradient [V m^{-1}]
F	Faraday constant [C V^{-1}]
i	Current density [A m^{-2}]
I	Current [A]
L	Length [m]
p	Pressure [Pa]
Pe	Péclet number [-]
R	Universal gas constant [J K^{-1} mol^{-1}]
Re	Reynolds number [-]
Re	Electric resistance [Ω]
T	Temperature [K]
u	Velocity [m s^{-1}]
z_k	Valence of the ion species k [-]

Greek symbols

ε	Permittivity of material [C m^{-1} V^{-1}]
ε_0	Permittivity of vacuum (free space), 8.854×10^{-12} [C m^{-1} V^{-1}]
ε_r	Relative dielectric constant [-]

ζ Zeta potential [V]

η Dynamic viscosity [kg m^{-1} s^{-1}] or [Pa s]

κ Inverse of the EDL thickness [m^{-1}]

ρ Fluid density [kg m^{-3}]

σ^{∞} Conductivity of electrolyte solution in the bulk [S m^{-1}] or [A V^{-1} m^{-1}]

ϕ_l Electric potential at the left end of the capillary [V]

ϕ_L Electric potential at the left end of the reservoir [V]

ϕ_r Electric potential at the right end of the capillary [V]

ϕ_R Electric potential at the right end of the reservoir [V]

Subscripts

0 Bulk solution

c Capillary

in Inlet

k Ion species

lo Electric load

out Outlet

r Reservoir

rl Reservoir of the left handside

rr Reservoir of the right handside

ref Reference parameter

Chapter 6: Experimental enhancement to forward osmosis (FO) - electrokinetic (EK) energy conversion system

6.1 Introduction

As already calculated in section 3.4, the energy conversion efficiency of the proposed forward osmosis (FO) - electrokinetic (EK) energy conversion system for the typical seawater and river water is estimated around 0.15%. Although it is competitive compared to other pressure-driven EK energy conversion technologies, such as the mechanical-electrokinetic battery [27] and the electrokinetic micro/nano-channel battery [28] with maximum energy conversion efficiencies of 0.77% and 0.045%, respectively, it still has a great potential to be further improved. In this chapter, two main experimental studies are conducted to enhance the energy conversion efficiency of the FO-EK system. Particularly, the improvement in the operation mode, continuously refreshing the draw solution (DS) instead of previously applied stack mode, and the surface treatment to the porous glass are investigated and discussed in the following two subsections.

6.2 Enhancement to FO-EK energy conversion system by continuous flow mode

It is already demonstrated in Chapter 4 that the FO flow rate in a separated FO module can be reasonably improved by applying tangential flow, namely a kind of convection flow, to timely refresh the DS. In this section, the advanced continuous flow mode by applying tangiential flow to the FO-EK system, instead of the stack mode with slower osmosis process, is further experimentally investigated to improve the performance of the FO-EK energy conversion system. As for the experiment of continuous flow mode, the tangential flow rate is the most essential parameter in determining the FO submodule performance and then the overall FO-EK system performance. Therefore, various tangential flow rates are applied to characterize the effects of the continuous flow model on the performance of the FO-EK energy conversion system.

6.2.1 Experiment

6.2.1.1 Experiment setup

Compared to the previous experimental study on the stack FO-EK energy conversion system in Chapter 3, the whole experiment setup employed in this section was the same except the FO submodule, as shown in Figure 6.1, where two pumps (Cole Parmer Masterflex L/S, 77301-22 Digital Modular Drive and 77301-21 Pump Drive Motor W/7518-00 Easy Load) were installed to separately circulate the fresh DS and FS through the FO submodule. In addition, three dampeners were mounted before/after the pumps to

smoothen the pulsation flow generated by the peristaltic pumps. The porous glass PG3 with radius of 9 mm and thickness of 3.72 mm and the cellulose triacetate (CTA) membrane with effective surface area of 0.0144 m^2 were used as the EK porous medium and FO semipermeable membrane.

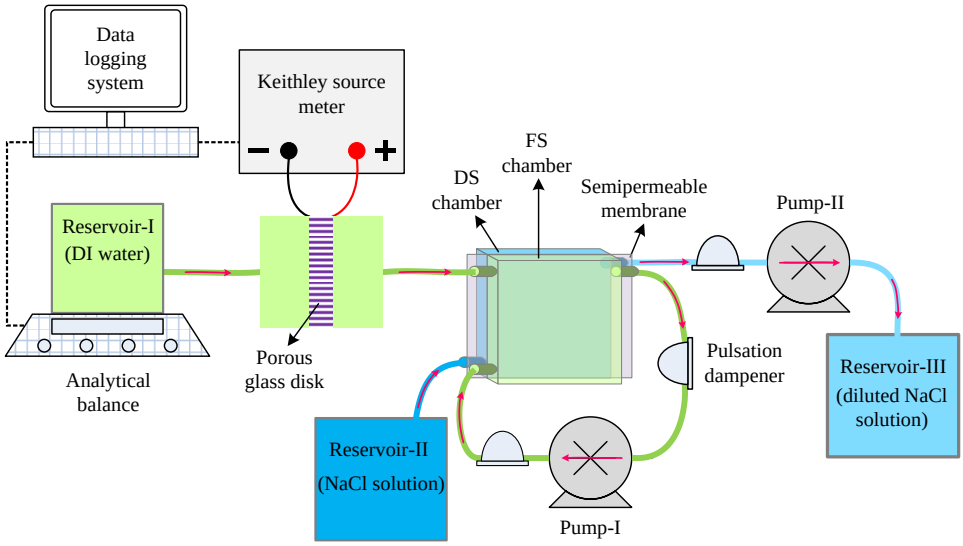

Figure 6.1 Schematic of the experimental FO-EK system with continuous flow mode.

6.2.1.2 Experiment procedure

The same with previous experimental study on the FO-EK stack system, the DI water was used as the FS and the NaCl solutions with five concentrations, 0.5 M, 1 M, 2 M, 3 M and 4 M, were individually used as the DS. In addition, the tangential flow rates of the continuous flows for both DS and FS were designed at 0 ml min^{-1}, 2 ml min^{-1}, 4 ml min^{-1}, 6 ml min^{-1}, 8 ml min^{-1}, 10 ml min^{-1}, 20 ml min^{-1}, 30 ml min^{-1}, 40 ml min^{-1}, 50 ml min^{-1}, 60 ml min^{-1}, and 70 ml min^{-1}. The procedure for carrying out the experiments was summarized as:

a. Soaked a new porous glass in DI water for 1 hour and soaked a newly tailored FO semipermeable membrane in the ultrasonic bath filled with DI water for 1 hour. Meanwhile, clean and dry all the components of the EK submodule and the FO submodule;
b. Respectively sealed the porous glass and the FO membrane in the EK submodule and the FO submodule;
c. Filled DI water into the EK submodule manually. Meanwhile, gradually filled DI water and NaCl solution with concentration of 0.5 M into the FS chamber and the DS chamber simultaneously by the pump at the same flow rate of 60 ml min^{-1}. Attentions should be carefully paid to avoid air bubbles being trapped in the EK submodule and the FO submodule;
d. Rapidly set up all the relevant experiment equipment into a system as shown in Figure 6.1;
e. Run the pumps at the volume flow rates from 0 ml min^{-1} to 70 ml min^{-1} as elaborated above. Each run with a specific volume flow rate lasted for about 1 hour. The streaming potential, the maximum streaming current, and the weight loss of the DI water within the reservoir-I were simultaneously recorded by the computer during each run;
f. Disassembled the whole setup after finishing all the runs in step e and repeated steps a-e at least three times to conduct the repeatability experiment for DS with concentration of 0.5 M;
g. Repeated steps a-f for every other DS concentrations of 1 M, 2 M, 3 M and 4 M.

All the recorded data were post-processed accordingly to explore relationships between the applied tangential volume flow rate and the performance of the FO-EK energy conversion system, accompanied by the corresponding error margins. The thorough results and discussion for the experiment of the continuous flow mode are elaborated in the following section.

6.2.2 Results and discussion

6.2.2.1 FO flux

It is already concluded in Chapter 4 that, at the DS concentration of 1 M, the external concentration polarization (ECP) region within the separated FO system can be reasonably constrained within a significant thin region in the vicinity of the membrane surface due to the continuously applied tangential flow and thus the FO flux is efficiently enhanced. In particular, as shown in the inner graph of Figure 6.2, the FO flux monotonously increases with increasing the tangential flow rate at a lower speed. Differently, the FO flux of the FO-EK energy conversion system, as shown in the outer graph of Figure 6.2, firstly increases with the growth of tangential flow rate before 40 ml min^{-1} but then decreases with continuously increasing the tangential flow rate after 40 ml min^{-1}. The difference between those two graphs is mainly attributed to that: on the one hand, the size of the inlets/outlets is quite close with that of the FO chambers in the separated FO system, which makes the entire FO semipermeable membrane uniformly exposed to the tangential flow. On the contrary, the size of the inlets/outlets is significantly smaller than that of the FO chambers in the FO-EK system, which makes the entire FO semipermeable membrane unevenly bearing the tangential flow and thus

greatly reduces the enhancing capacity of the tangential flow, especially at the larger tangential flow rate; on the other hand, the connected EK module and tubing system in the FO-EK energy conversion system also exert significant negative effects on the FO flux. Particularly, the higher the tangential flow rate is, the more serious the negative effects are. Therefore, with increasing the tangential flow rate, the FO flux steadily rises for the pure FO system but firstly increases and then decreases for the FO-EK energy conversion system.

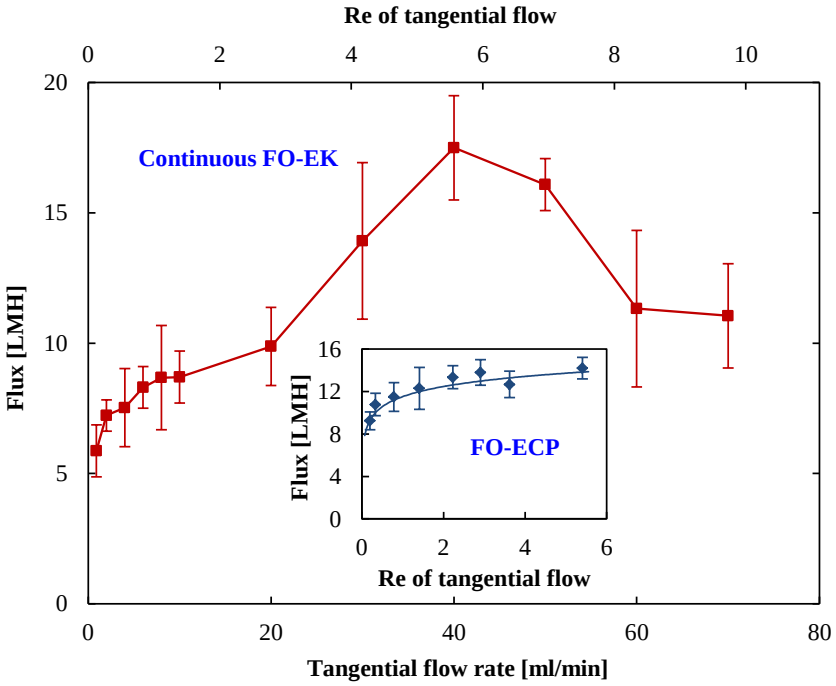

Figure 6.2 Effects of the tangential flow on the FO flux at the DS concentration of 1 M. The inner graph shows the relationship between the FO flux and the Reynolds number of the tangential flow within the separated FO microchannel system. In addition, the outer graph shows the relationship between the FO flux and the tangential flow rate within the FO-EK energy conversion system. The lower and the upper horizontal axes represent the tangential flow rate and the corresponding Reynolds number, respectively.

In addition to the comparison study above, a completed FO flux variations with the tangential flow rate for all five DS concentrations in the FO-EK energy conversion system are shown in Figure 6.3. All those five curves in this figure, corresponding to the five DS concentrations, show a similar trend, i.e., the FO flux increases with increasing the tangential flow rate, and reaches the maximum FO flux at the tangential flow rate around 40 ml min^{-1}, and then slightly descends after 40 ml min^{-1}. This finding demonstrates that, compared to the stack mode, the continuous flow mode can reliably enhance the performance of the FO-EK energy conversion system. However, due to the size difference between the inlets/outlets and the FO chambers and the negative effects from the connected EK submodule and tubing system, the FO flux cannot be monotonously increased by increasing the tangential flow rate but descends after a certain tangential flow rate.

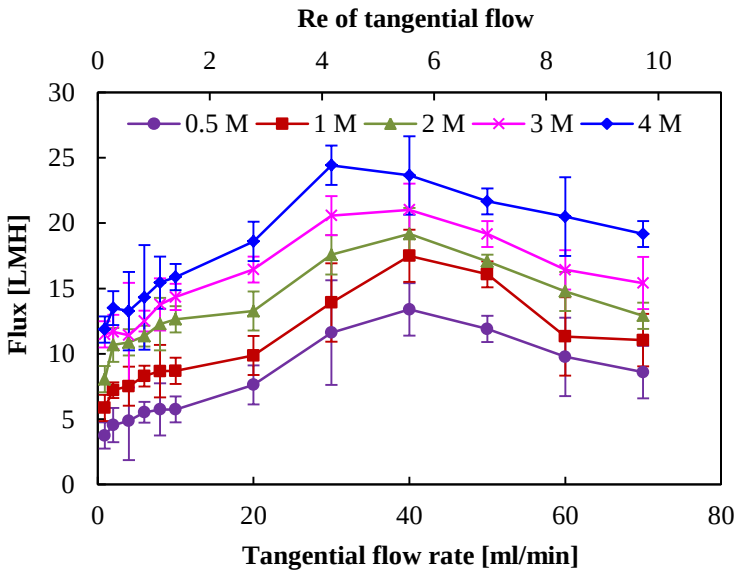

Figure 6.3 Effects of the tangential flow on the FO flux of the FO-EK energy conversion system.

6.2.2.2 Streaming potential and maximum streaming current

As already calculated in Chapter 3, the electric double layer (EDL) thickness for the working fluid of DI water is around 0.3 μm. Meanwhile, the average pore raduis of PG3 used in this experiment is estimated as 6 μm. For a pure pressure-driven EK flow with large ratio of the microchannel radius to the EDL thickness, particularly larger than 10 as already proved in Chapter 5, the streaming potential and the maximum streaming current almost linearly increase with the rising volume flow rate of the pressure-driven flow through the microchannel. In addition, the volume flow rate is in proportional to the FO flux for the FO-EK energy conversion system. Therefore, similar variation trends of the streaming potential and the maximum streaming current with that of the FO flux are achieved as respectively shown in Figure 6.4.a and Figure 6.4.b.

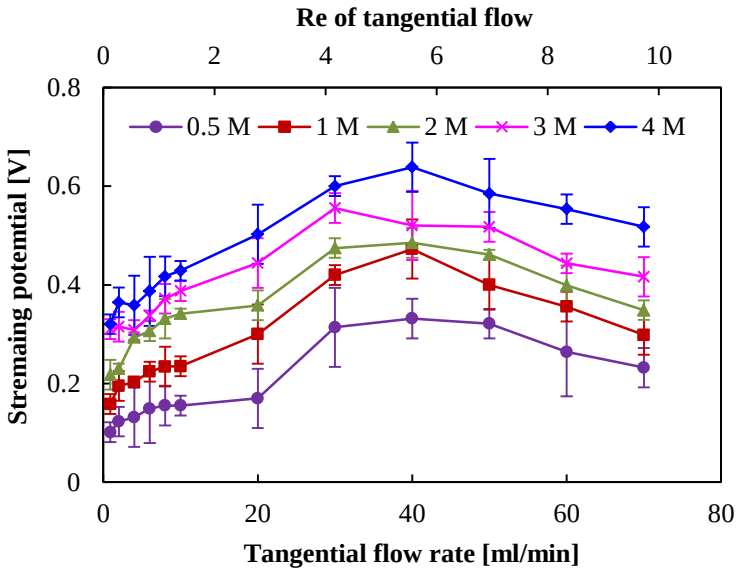

a

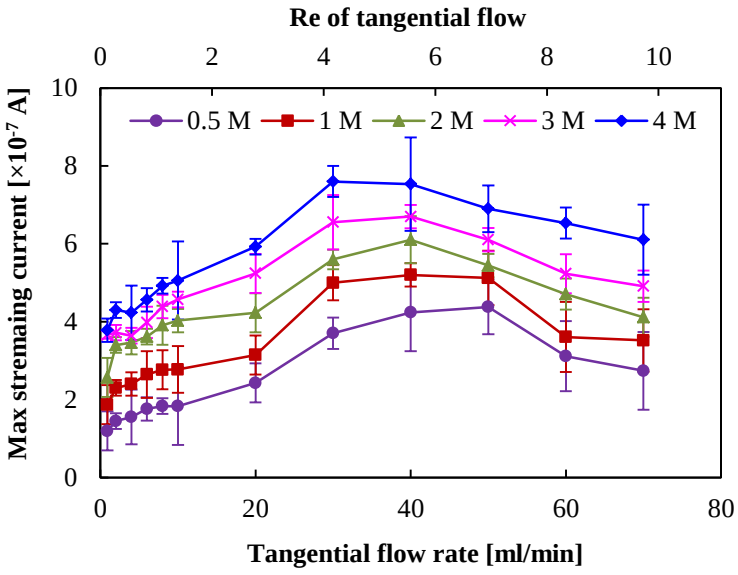

b

Figure 6.4 Effects of the tangential flow on the streaming potential (a) and the maximum streaming current (b) of the FO-EK energy conversion system.

Obviously, although there are slightly declines at high tangential flow rate, both the streaming potentials and the maximum streaming currents, compared with the previously achieved results in the stack FO-EK system, are greatly enhanced by the continuously applied tangential flow. The maximum values of those two parameters for all five DS concentrations appear at the tangential flow rate ranging from 30 ml min^{-1} to 50 ml min^{-1} with the corresponding Re number ranging from 4.17 to 6.95.

6.2.2.3 Maximum power density

Based on the working fluid of DI water and the porous media of PG3, the current-potential curve, according to the conclusion of Chapter 5, can be reasonably regarded as linear. Then the maximum power density is easily achieved according to Eq. (3.35) and Eq. (3.36). The effects of the tangential flow on the maximum power density are shown

in Figure 6.5. It shows that, similar with the trends of the streaming potential and the maximum streaming current, the maximum power densities for all five DS concentrations are significantly improved by the continuous flow mode, especially for the tangential flow rate ranging from 30 ml min^{-1} to 50 ml min^{-1}. The maximum increment among all the enhanced power densities, according to calculations, reaches up to as much as 9.6 times higher at the DS concentration of 0.5 M and the tangential flow rate of 40 ml min^{-1}.

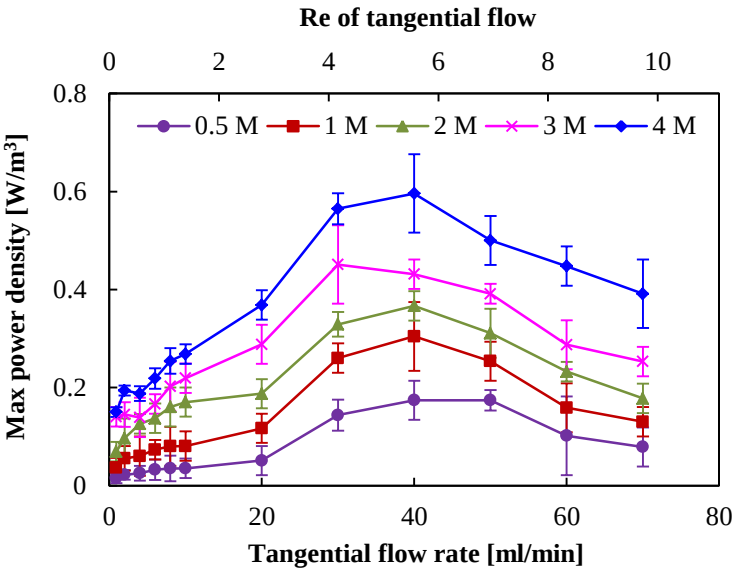

Figure 6.5 Effects of the tangential flow on the maximum power density of the FO-EK energy conversion system.

6.3 Enhancement to FO-EK energy conversion system by surface treatments to the porous glass

According to conclusions obtained in Chapter 5, for the working fluid of DI water and the porous media of PG3, the induced streaming potential, maximum streaming

current and maximum power density by the pressure-driven EK flow always monotonously increase with increasing the surface charge density. Obviously, enhancements in the surface charge density can greatly improve energy conversion performance of the pressure-driven EK flow. What's more, although it is assumed in Chapter 3 that all the void pores or spaces within the porous glass are connected, the porous glass surface indeed cannot be fully filled with liquid due to the complex tortuous structure of the porous glass. Amounts of air bubbles are probably trapped inside some blind pores. Therefore, some powerful approaches should also be implemented to dislodge all the air bubbles out from the porous glass, thus create larger volume charge density, and finally further enhance the energy conversion performance of the pressure-driven EK flow.

In this part, two surface treatment approaches, ultrasonic treatment and sodium dodecyl sulfate (SDS) surfactant treatment, will be separately and cooperatively conducted to enhance the energy conversion performance of the pressure-driven EK flow. On the one hand, one of the most common applications of ultrasonic treatment is to be as cleaner. Compared to the other chemical cleaning methods, the ultrasonic cleaner can efficiently clean contaminants or debris without damaging or polluting the object's surface structure. Meanwhile, the ultrasonic vibrations as well as the induced high temperature also effectively eliminates the trapped air bubbles from the complex tortuous structure of the porous glass, making the porous glass being fully contacted with liquid and thus giving rise to higher volume charge density. On the other hand, as one of the most researched anionic surfactants, the SDS is widely used in many cleaning and hygiene products. In addition to this unique cleaning property, the SDS surfactant

treatment can also modify the surface properties of the glass channel due to its special amphiphilic structure consisting of a 12-carbon tail attached to a sulfate group [148]. Generally, both of those two approaches can effectively clean and degas the porous glass and, essentially, make it being fully wetted, which greatly benefits to the stability and efficiency of the energy conversion performance of the pressure-driven EK flow through the porous glass.

6.3.1 Experiment

6.3.1.1 Experiment setup

Experimental study mainly focuses on investigating effects of surface treatments, particularly ultrasonic treatment and SDS surfactant treatment to the porous glass, on the energy conversion performance of the pressure-driven EK flow. The machine, ultrasonic cleaner (Branson 8510MT) with frequency of 40 KHz, was applied to provide ultrasonic treatment on the porous glass. Meanwhile, SDS (Sigma-Aldrich) was employed as anionic surfactant. DI water was used to prepare SDS solution and generate EK power all through the experiments. The conductivity of the DI water was strictly kept within 0.9 ~ 1.1 μS cm^{-1}. Totally four different SDS solution concentrations were prepared for the surfactant treatment, namely 3 mM, 6 mM, 8.2 mM and 12 mM, which followed by ultrasonic process for an hour to enhance the dissolution of SDS in DI water. For the porous media, only PG3, giving rise to the best energy conversion performance as demonstrated in Chapter 3, was employed in this experimental study.

Since the experiments in this part only focus on surface treatments to the porous glass, the experiment setup was simplified by replacing the FO submodule mentioned in

Chapter 3 with a pump (Cole Parmer Masterflex L/S, 77301-22 Digital Modular Drive and 77301-21 Pump Drive Motor W/7518-00 Easy Load). The overall experiment setup is shown in Figure 6.6. A flow dampener was placed between the pump and the EK holder to regulate the pulse flow supplied by the pump. The measured weight loss of the DI water within the reservoir-I was logged into the computer, which would be post-processed to volume flow rate. Meanwhile, the measured streaming potential and maximum streaming current were simultaneously recorded by the computer.

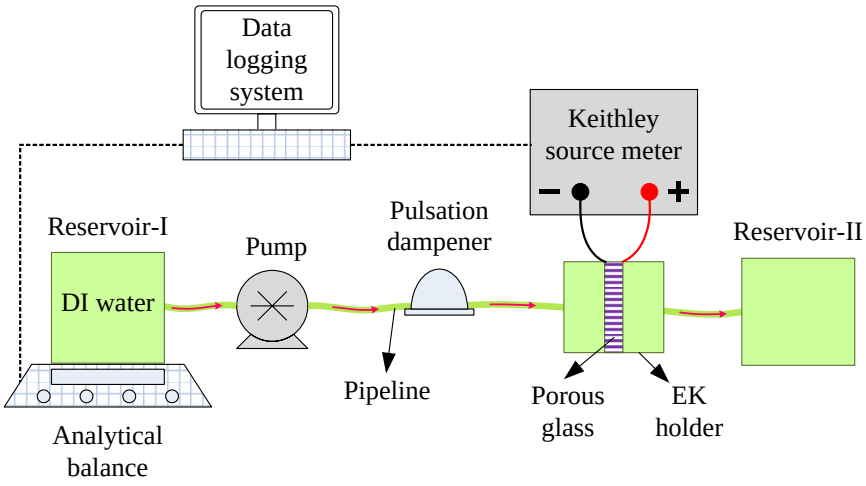

Figure 6.6 Schematic of the experiment setup for surface treatment on porous glass.

6.3.1.2 Experiment procedure

The procedure for the ultrasonic treatment was very simple, i.e., putting the beaker filled with a new PG3 and DI water into the basin of the running ultrasonic cleaner for 1 hour. In addition, the procedure of surfactant treatment to a porous glass with SDS solution was as follows:

a. Referring to Figure 6.6, replaced the DI water in reservoir-I with the prepared SDS solution (3 mM, 6 mM, 8.2 mM or 12 mM) and then pumped the prepared SDS solution through the porous glass at volume flow rate of 5 ml min^{-1} for 1 hour. During the treatment, the SDS solutions were constantly subjected to a mild heating source created by the hot plate to enhance the surfactant adsorption;
b. Stopped circulating the SDS solution and incubated the porous glass for another 30 minutes to further enhance the surfactant adsorption;
c. Continuously pumped DI water at volume flow rate of 5 ml min^{-1} through the porous glass to flush away the redundant SDS solution and then stopped pumping when the measured potential difference was stabilized.

In order to compare the experiment results from the PG3 treated by SDS with that untreated by SDS under the same conditions, another treatment by pure DI water, i.e., SDS solution of 0 mM, should also be added to the surfactant treatment with exactly the same experimental procedure from the step a to the step c. The combined surface treatment meant that, prior to being treated by the SDS solution as mentioned above, the porous glass should be treated by the ultrasonic first.

For each run with a newly surface-treated porous glass, the performance testing system was then set up based on the schematic shown in Figure 6.6. The weight loss of DI water, the streaming potential and the maximum streaming current at 5 different volume flow rates, namely 5 ml min^{-1}, 10 ml min^{-1}, 15 ml min^{-1}, 20 ml min^{-1} and 25 ml min^{-1}, were successively measured and recorded.

6.3.2 Results and discussion

In this part, the effects of two surface treatments, namely the ultrasonic treatment and the SDS surfactant treatment, on the performance parameters of the pressure-driven EK energy conversion process, including the streaming potential, the maximum streaming current and the maximum power density, are thoroughly discussed. In order to explore what indeed happened to the porous glass after being treated by both approaches, it is necessary to make clear the interface structure between the silica glass and the DI water. It has already been concluded that any silica glass surface contacting with water is consisted by silanol (SiOH) groups, a kind of hydrophilic group and directly providing negative surface charge of SiO^-, and alternatively located inactive siloxane (SiOSi) bridges, a kind of hydrophobic group [149, 150]. Based on this specific structure, all the experimental findings can be readily discussed and explained.

6.3.2.1 Effects of ultrasonic treatment

Figure 6.7.a and Figure 6.7.b show that the generated streaming potential and maximum streaming current almost linearly increase with increasing the flow rate, which is in consistent with the conclusions obtained in Chapter 5. In addition, compared to the porous glass not treated by ultrasonic, the porous glass treated by ultrasonic gives rise to higher streaming potentials and maximum streaming currents and also creates significantly shorter error bars. Those phenomena are mainly attributed to that the ultrasonic treatment process, accompanied by dramatic ultrasonic vibrations and high induced temperature, eliminates tiny air bubbles trapped inside the porous glass, and thus

makes the porous glass being fully wetted by DI water, and finally creates more stable and higher volume charge densities all through the experiments.

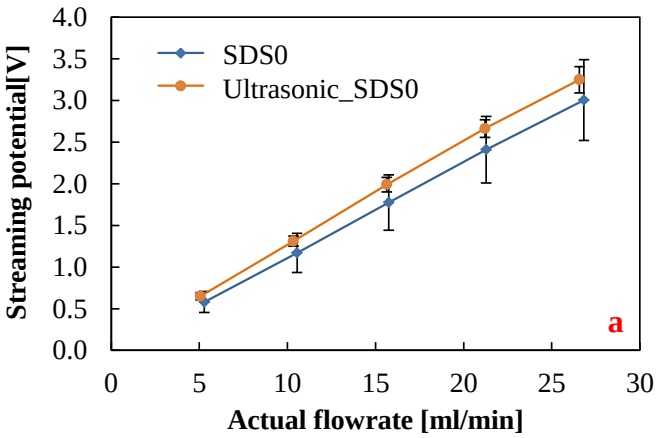

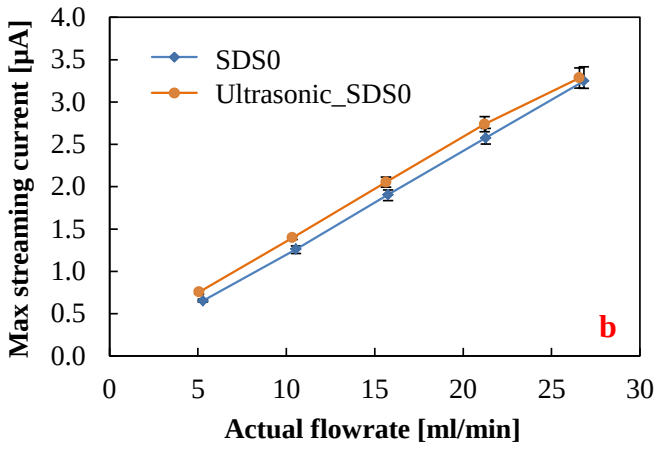

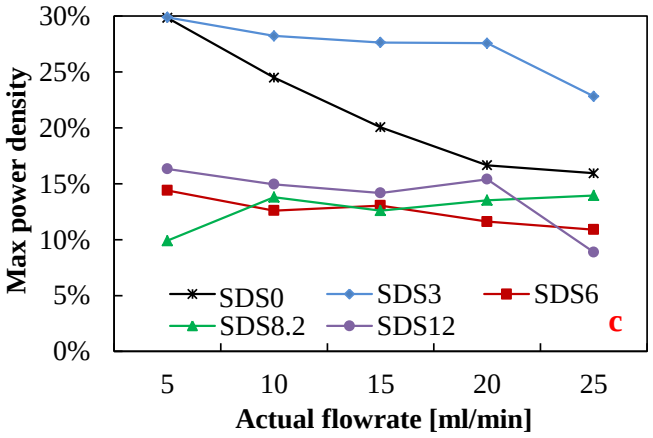

Figure 6.7 Effects of the ultrasonic treatment on the energy conversion performance of the pressure-driven EK flow through porous glass PG3. In figures a and b, 'SDS0' represents that the porous glass is treated by pure DI water (equally regarded as SDS solution with concentration of 0 mM) strictly following the procedure of SDS surfactant treatment; meanwhile, 'Ultrasonic_SDS0' represents that the porous glass is firstly treated by ultrasonic and then subsequently treated by SDS 0 mM. In figure c, all curves show comparison between two sets of the maximum power densities. One set is obtained from the porous glass only treated by the SDS surfactant (including 0 mM, 3 mM, 6mM, 8.2mM or 12 mM), while the other set is obtained from the porous glass firstly treated by ultrasonic and subsequently treated by SDS (also including 0 mM, 3 mM, 6mM, 8.2mM or 12 mM). For each SDS solution concentration, the increment of the power densities is achieved by comparing the latter set to the former set.

Since both the generated streaming potential and maximum streaming current are almost linear increasing functions of the flow rate, the maximum power density can be easily achieved according to Eq. (3.35) and Eq. (3.36). Instead of the net value of the maximum power density, investigations in this aspects mainly focus in the increment of the maximum power density, which is shown in Figure 6.7.c. All positive increments in the maximum power densities show that the porous glass treated by ultrasonic outperforms the porous glass untreated by ultrasonic. Particularly for the trend of the maximum power density from the porous glass treated by 0 mM SDS (i.e., DI water), the explanations mainly include that: on the one hand, as a effective cleaner, the ultrasonic can efficiently clean the porous glass, making the previously contaminant-covered pore surface being fully exposed to DI water; on the other hand, the native degasing function of the ultrasonic treatment also makes the previously bubble-occupied space in the porous glass being fully filled by DI water. Obviously, both of those two aspects can significantly involve more effective surface, specifically more negative surface charges,

in the energy conversion process of the pressure-driven EK flow. In addition, with increasing the flow rate, the dynamic pressure is higher, which also benefits more to the degasing process of the porous glass untreated by ultrasonic. Therefore, the improvement at higher flow rate is not as significant as that at lower flow rate. For the trends of the maximum power densities from the porous glasses treated by SDS solutions (with concentrations larger than 0mM), the essential reason also because that the ultrasonic treatment can involve more effective surface area in the energy conversion process as elaborated above. However, the mechanism is a little bit different. Particularly, in addition to involving more hydrophilic silanol groups, which directly gives rise to larger volume charge density, the ultrasonic treatment also simultaneously involves more hydrophobic siloxane bridge groups being contacted with SDS solutions. The hydrophobic tails of the SDS molecules will be adsorbed onto the hydrophobic siloxane bridge groups, leaving the negatively charged hydrophilic head exposing in the bulk liquid. Obviously, this self-assembled monolayer indirectly gives rise to more negative surface charges, i.e., higher surface charge density. Consequently, the porous glass treated by ultrasonic shows better energy conversion performance compared to the corresponding one untreated by ultrasonic.

6.3.2.2 Effects of SDS surfactant treatment

After being treated by ultrasonic, the overall surface charges of the porous glass became much more stabilized. Then the SDS surfactant treatment with five different solution concentrations was separately conducted to the ultrasonic-treated porous glass. The effects of the SDS surfactant treatment on the energy conversion performance of the pressure-driven EK flow through the porous glass PG3 is shown in Figure 6.8.

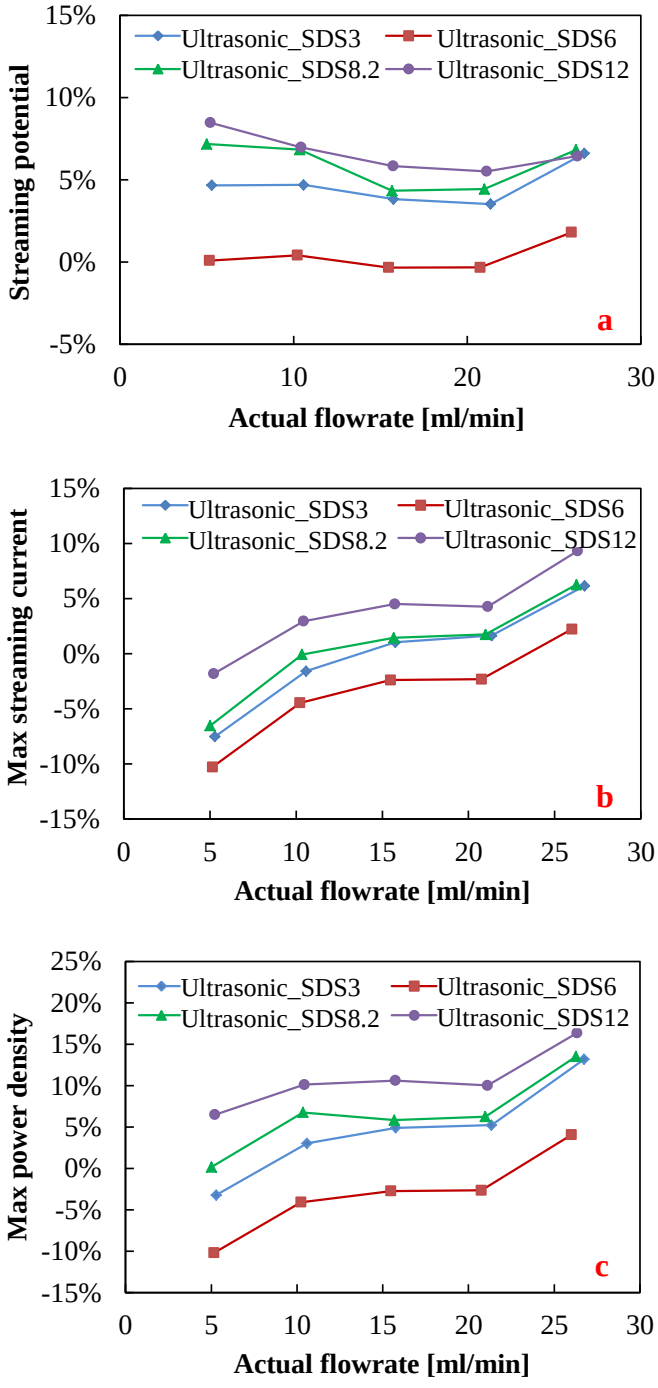

Figure 6.8 Effects of the SDS surfactant treatment on the energy conversion performance of the pressure-driven EK flow through porous glass PG3. All curves show the increments of the energy conversion performance from the porous glass treated by ultrasonic and SDS solutions with concentration of larger than 0 mM. The benchmark corresponding to all the comparisons is the energy conversion performance from the porous glass treated by ultrasonic and SDS 0 mM.

It is observed that, the PG3 treated by ultrasonic and SDS 12 mM always yields the highest enhancement to the energy conversion performance while the PG3 treated by ultrasonic and SDS 6 mM always yields the lowest enhancement. In addition, high flow rate also benefits more to energy conversion process compared to the low flow rate which sometimes even degrades the energy conversion performance. Finally, calculations show that, compared to the porous glass without any surface treatment, the porous glass treated by ultrasonic and SDS 12 mM gives rise to the best energy conversion performance with the maximum power density of 3.08 W m^{-3} and the corresponding increment of 27.3%.

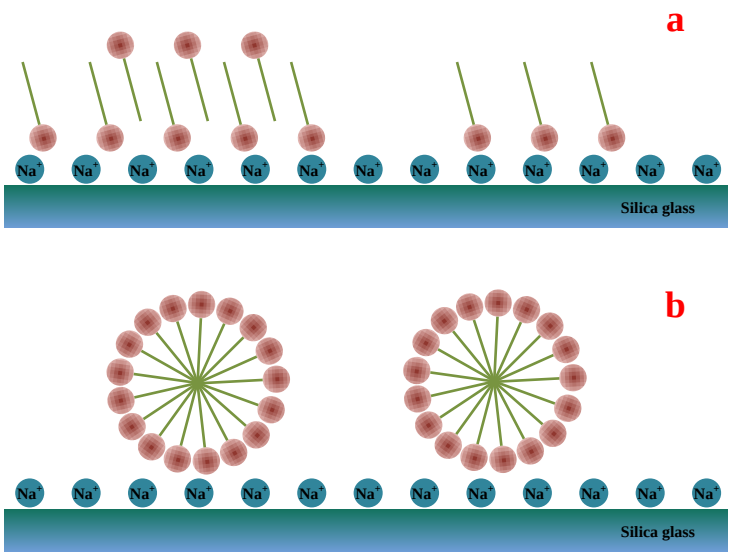

Figure 6.9 Schematic of four stages of surfactant aggregating on the silica glass surface.

As for the high flow rate always benefitting more to energy conversion process compared to the low flow rate, it is because that, with increasing the flow rate, more negatively charged surface is involved in energy conversion process due to the higher dynamic pressure, giving rise to better energy conversion performance. As for the variation trends at different SDS concentrations, it can be ultimately attributed to the

aggregation of SDS molecules onto the porous glass surface. As well known, the critical hemimicelle concentration (HMC) and the critical micelle concentration (CMC) of the SDS solution are around 1.6 mM and 8.2 mM, respectively. When the concentration of the SDS solution is between HMC and CMC as shown in Figure 6.9.a, the Na^+ ions on the glass surface are saturated while the SDS^- ions start to form bilayers, i.e., hemimicelle, near the glass surface. When the concentration of the SDS solution is beyond CMC as shown in Figure 6.9.b, the previously formed bilayers begin to aggregate, forming micelles [148]. Consequently, compared to the other three statuses corresponding to concentrations of 3 mM, 8.2 mM and 12 mM, the status corresponding to 6 mM is that the glass surface is the most partially covered by the dilayers. Those dilayers are hardly flushed away by the DI water, which induces more positive ions fill in the bare spaces to counterbalance the surface charges, giving rise to seemingly shrinking EDL. As already proved in Chapter 5, thinner EDL gives rise to lower energy conversion efficiency. Meanwhile, the SDS 6 mM provides relatively smaller number of SDS^- ions adsorbed onto the hydrophobic groups of the porous glass and thus creates smaller number of indirect surface charges. Therefore, the porous glass treated by SDS 6 mM shows the lowest enhancement to the energy conversion performance. Differently, compare to the other three statuses corresponding to concentrations of 3 mM, 6 mM and 8.2 mM, the status corresponding to 12 mM is that the glass surface is fully covered by the micelles. Those micelles are easily flushed away by the DI water, which almost has no interference on the EDL. Under this situation, the SDS 12 mM provides relatively largest number of SDS^- ions adsorbed onto the hydrophobic groups of the porous glass and thus gives rise

to highest surface charge density. Therefore, the porous glass treated by SDS 12 mM shows the highest enhancement to the energy conversion performance.

6.4 Summary

Two main experimental studies are conducted in this chapter to enhance the energy conversion performance of the proposed FO-EK system, and they are the continuous flow mode and the surface treatments to the porous glass PG3. As for the continuous flow mode, the tangential flow rate is found to be the most essential parameter in determining the FO submodule performance and then the overall FO-EK system performance. Therefore, a series of tests based on various tangential flow rates are conducted to characterize the effects of the continuous flow model on the performance of the FO-EK energy conversion system. As for the surface treatment, the surface/volume charge density is the most enssential factor in determining the energy conversion performance of the pressure-driven EK flow though a porous glass with pore size being of much larger than the EDL thickness. Therefore, two surface treatment approaches, namely the ultrasonic treatment and the SDS surfactant treatment, are conducted to increase the surface/volume charge density and thus enhance the energy conversion performance of the pressure-driven EK flow. Based on comprehensive results and discussion from those two experimental studies, main findings are summarized as follows:

1. For the continuous flow mode, all the performance parameters of the FO-EK system, including the FO flux, the streaming potential, the maximum streaming current and the maximum power density, show inverted v-shape variation with the tangential flow rate. The optimum operation tangential flow rate happens at the region from 30 ml

min^{-1} to 50 ml min^{-1}. The maximum increment of all the enhanced power densities, according to calculations, reaches up to as much as 9.6 times higher at DS concentration of 0.5 M and tangential flow rate of 40 ml min^{-1}.

2. For the surface treatments, both the ultrasonic treatment and the SDS surfactant treatment to the porous glass can significantly improve the energy conversion performance of the pressure-driven EK flow. Particularly, in addition to its intrinsic advantages as an effective cleaning and degasing means, the ultrasonic treatment also facilitates the subsequent SDS surfactant treatment by inducing more hydrophobic groups for adsorbing the SDS molecules, which gives rise to higher surface charge density and thus leads to higher energy conversion performance. The maximum increment from the porous glass PG3 corporately treated by both ultrasonic and SDS 12 mM is calculated at around 27.3 % with corresponding power density of 3.08 W m^{-3}.

Chapter 7: Conclusions and recommendations

7.1 Contributions of this dissertation

In this work, studies are carried out emphasizing on a novel forward osmosis (FO) - electrokinetic (EK) energy conversion system which is proposed and developed by taking advantages of the EK and the FO techniques. This hybrid energy conversion technique is more advantageous over the other similar electric energy conversion techniques, such as the PRO and the EK techniques. This is due to the following facts that: on the one hand, compared to the PRO systems, the proposed system operates in low pressure environment, especially in FO sub-module, thus has much lower requirement on FO membrane and also much less membrane scaling and fouling problems. Therefore, it is more cost effective. On the other hand, unlike the other pressure-driven EK systems where pumps are needed to provide the pressure driven flow, this hybrid system is directly driven by the salinity gradient energy to generate electricity without any extra energy input like pumping power. However, the main limitation of this hybrid energy conversion technique lies in the low energy conversion efficiency of EK process.

The entire dissertation research can be summarized as followings. Firstly, comprehensive theoretical and experimental studies are conducted in Chapter 3 to assess and characterize the performance of the FO-EK energy conversion system. Secondly, since concentration polarization (CP) phenomena happened in both FO and EK submodules can reduce the energy conversion performance of the stack FO-EK system, another two studies on the CPs are successively conducted in Chapter 4 and Chapter 5

respectively on the FO process and the EK process. Finally, based on the results of the CP studies, strategies and the corresponding experimental tests for improving the FO-EK energy conversion system and enhancing the energy conversion performance of the FO-EK system are proposed and implemented in Chapter 6. In conclusion, this dissertation focuses a novel FO-EK energy conversion method, develops the relevant mathematical models, builds the integral experimental systems, and finally improves the overall system to achieve higher energy conversion performance. Meanwhile, the research approaches employed in this work include theoretical development, numerical simulation and experimental investigation. The major contributions made by this research work are provided as below:

1. **Characterization of the novel forward osmosis (FO) - electrokinetic (EK) energy conversion system**

The first main contribution is that, inspired by the tremendous salinity gradient energy at the river mouth, this study presents a novel hybrid FO-EK energy conversion system, consisting of a FO submodule and an EK submodule, to convert the salinity gradient energy into electric energy. For the overall system, a suction force generated in the FO submodule due to the mechanism of FO draws water through a porous glass disk housed in the EK submodule. When such osmotic pressure-driven flow passes across the porous glass, the streaming potential and the streaming current are simultaneously generated and they can be harvested as the power source to an external electric circuit. This hybrid energy conversion technique has been demonstrated considerably advantageous due to its friendly operating environment and no any extra energy requirement like pumping power.

Another main contribution is the theoretical study for the pressure-driven EK flow through a porous medium. Particularly, compared to the commonly used uniform-capillary model, this study develops a heterogeneous-capillary model for the pressure-driven EK flow through a porous medium, which is proved to be prominently more consistent with experimental results.

2. External concentration polarization (ECP) in forward osmosis (FO)

The first main contribution is innovatively introducing the microtechnology into the FO process. Due to significant advantages over large-scale systems used in conventional FO studies, a micro-FO-device is fabricated and utilized to systematically study the predominating ECP phenomenon in FO process. It is because of the novel application of the microtechnology in FO process so that this work successively achieves the experimental visualization and quantitative characterization of the ECP layer, which haven't been done by other researchers.

The second main contribution is that the convection-diffusion model is found to be superior to the commonly used film theory. Film theory is a one-dimensional (1D) analytical model based on assumptions that, solvent permeating flux along the membrane is axially invariant and it has no effect to the axial velocity field. However, both theoretical study based on convection-diffusion model and experimental study show that the thickness of the ECP layer varies along with the axial direction. Thus, the solvent permeating flux and the axial velocity field, accordingly, vary with the axial direction.

The third main contribution is that the study on the ECP in FO process provides valuable optimizing approach to FO process. At low Re numbers ranging from 0 to 1, the FO performance is predominately determined by the ECP phenomenon due to the

significantly reduced osmotic pressure within the ECP layer. Although the FO flux is low at this Re number range, the FO efficiency is high. On the contrary, at high Re number larger than 1, the ECP phenomenon is greatly reduced by applying high tangential flow rate. However, the enhancement in FO flow rate is not significant due to the little variation of ECP layer, leading to considerably low FO efficiency. In this situation, if a higher flow rate is needed, the methods such as reducing ICP or using high performance semipermeable membranes are preferred rather than simply increasing the tangential flow rate.

3. Ion concentration polarization (IonCP) in pressure-driven electrokinetic (EK) flow through a capillary system

The main contribution is that, the study of the IonCP in pressure-driven EK flow through a capillary system figures out the way how the IonCP essentially affects the inner characteristics and the terminal characteristics of the capillary system and the relationships between those two kinds of characteristics, and, consequently paves the way for further practical applications. Particularly, the dimensionless numerical analysis is adopted and the simulation process is improved by setting the output current rather than the previously applied output potential gradient as zero at the outlet when solving for the streaming potential. In addition to the in-depth and comprehensive analyses on the inner characteristics (including distributions of the induced potentials, the ion species and the electric conductivities), investigations on the terminal characteristics (including the overall electric resistances, the streaming potentials, the maximum streaming currents and the current-potential curves) are also conducted. Finally, the relationships between the inner and the terminal characteristics of the capillary system are fully explored through

analyzing the IonCPs occurrence during pressure-driven EK energy conversion process in a capillary system.

7.2 Recommendations for future studies

7.2.1 Further experimental enhancement to FO-EK energy conversion system

As experimentally studied in Chapter 6, the FO flux, the streaming potential, the maximum streaming current and the maximum power density, show inverted v-shape variation with the tangential flow rate, namely firstly increasing and then decreasing with the tangential flow rate. According to analysis, this is mainly attributed to the significant size difference between the small inlets/outlets and the large FO chambers, which makes the entire FO semipermeable membrane unevenly bearing the tangential flow and thus greatly diminishes the enhancement capacity of the tangential flow. Therefore, further improvement on the continuous flow, as shown in Figure 7.1, by applying more uniform tangential flow to the FO submodule is necessary. In addition, in order to make use of the gravitational force to further enhance the FO performance, the FO submodule is recommended to be placed horizontally with the FS and the DS chambers respectively being at the upside and underside of the semipermeable membrane. This suggested placement is also much closer to the natural phenomena when the riverwater, with relatively higher water level, meeting with the seawater, with relatively lower water level, at the river mouth.

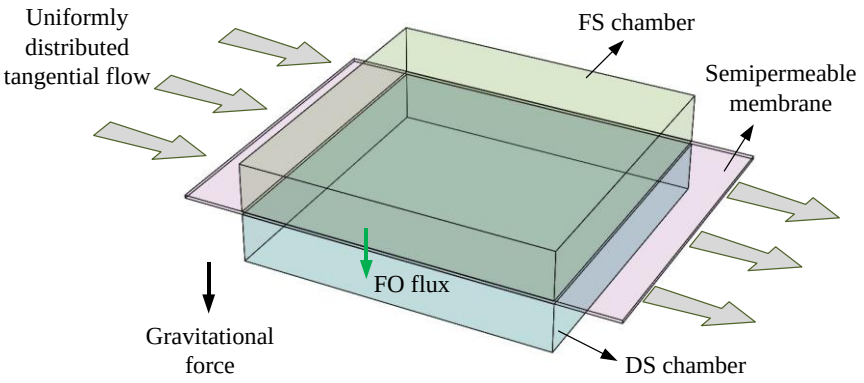

Figure 7.1 Schematic of further improvement for the FO submodule.

Furthermore, it is introduced in the Literature review section that slip boundary occurrence at the hydrophobic surface of micro/nano-channels can significantly enhance the EK energy conversion process. However, the requirement of high hydrophobic surface normally is in contradiction with that of the high zeta potential. How to practically balance those two aspects to achieve better hydrodynamic and EK performance is an interesting and promising development direction. Consequently, in addition to the surface treatment studies already conducted in this work, another two surface treatment methods are also recommended for future study:

1. Treat silica micro/nano-channel with carboxyl groups. It has been proved that, compared to the original silica material with a zeta potential of −42mV, the silica material modified by carboxyl groups exhibits an increased zeta potential up to −72mV with almost no alteration of the wetting property [151];
2. Treat silica micro/nano-channel with poly (propylene glycol) methacrylate (PPGMA). For silica material modified by PPGMA, the zeta potential is almost not affected while the ability of adsorbing water molecules significantly decreases, i.e., there is a

great enhancement in the hydrophobicity through the surface modification process while keeping the zeta potential unchanged [152].

7.2.2 Further experimental study on the IonCP in pressure-driven EK flow through a capillary system

Literature review in this work shows that only a few theoretical studies on the pressure-driven EK energy conversion process recognize that the IonCP phenomena reduce the generated electric power and the energy conversion efficiency. Compared to their studies, this work conducts a much more comprehensive numerical study to investigate the effects of the IonCP on the energy conversion performance of the pressure-driven EK flows. However, all existing studies only focus on theoretical or numerical analyses. So far, there is no experimental research work investigating the IonCP phenomena and the related effects on the pressure-driven EK flows. In order to fill in this research gap, two preliminary proposals for the experimental study based on research results in this work are provided for future study. The corresponding conceptual experiment setups are shown in Figure 7.2, which are designed mainly for the experimental studies on the IonCP through a porous medium and through a capillary.

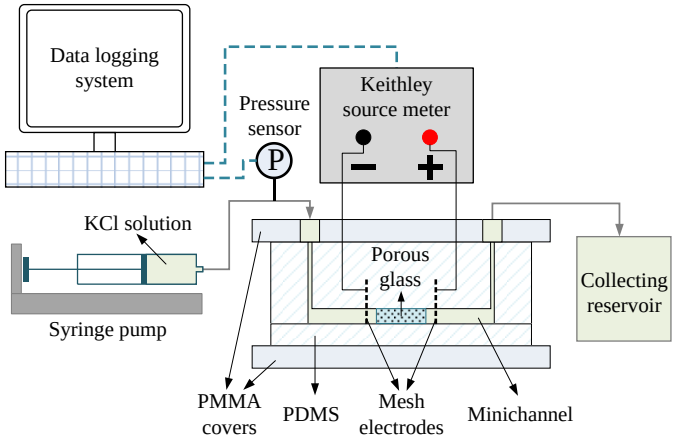

a

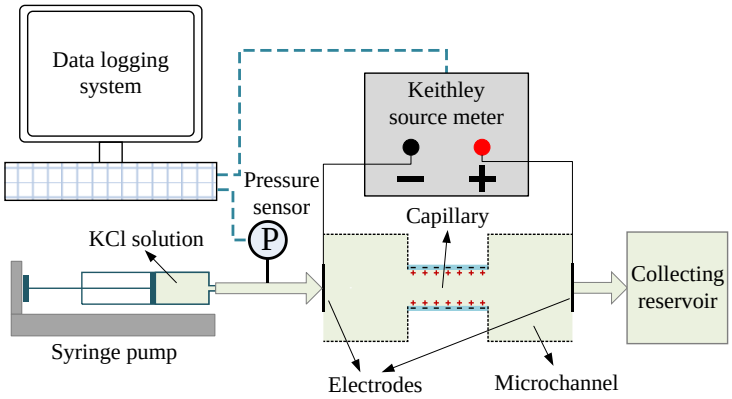

b

Figure 7.2 Schematic of experiment setups for studying the IonCP though a porous medium (a) and through a capillary (b). The Keithley source meter is utilized in both experimental studies as a measuring apparatus and simultaneously as an external electric load.

7.2.3 Enhance energy conversion performance of the pressure-driven EK flow by applying non-Newtonian nanofluids

Berli studied that, some kinds of non-Newtonian nanofluids, such as polymer solutions and colloidal suspensions which contain discrete entities in the nanoscale, can

be used as flow media for the electroosmosis flow instead of simple electrolyte solutions to give rise to higher thermodynamic efficiency [153]. As shown in Figure 7.3, when such kinds of non-Newtonian nanofluids are forced passing through a micro/nano-channel by a pressure gradient, a certain degree of wall depletion with depletion layer of δ will happen at the interfacial region. If the thickness of EDL λ is smaller than δ, the streaming current will be free of the macromolecules or nanoparticles in the bulk liquid. As known that, the viscosity of non-Newtonian nanofluids is a function of the shear rate $\dot{\gamma}$, i.e., $\mu_p(\dot{\gamma})$, which has been proved to be always higher than the viscosity of simple electrolyte solution, μ_s [154]. It means that, if proper polymer solutions are utilized in such a micro/nano-channel, the viscosity of the nanofluids in the bulk must be relatively higher than that in the depletion layer. In addition, based on Eq. (3.13) and Eq. (3.14), the maximum energy conversion efficiency for the case of $\lambda << a$ can be approximated as $\eta_{\max} = \frac{1}{4}\frac{\alpha_{12}^2}{\alpha_{11}\alpha_{22}}$ [29, 32, 155, 156]. According to expressions of all coefficients, it is evidently observed that the method of adding water-soluble polymer or nano-particles into the background electrolyte solution will reduce the coefficient α_{22} without altering α_{12} and thus logically increase the energy conversion efficiency. Therefore, the approach of exploring and investigating some proper non-Newtonian nanofluids to increase the energy conversion efficiency of the pressure-driven EK process is recommended for future study.

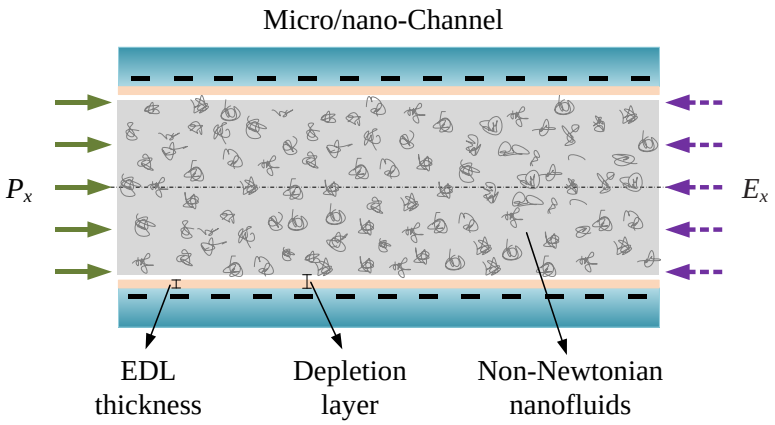

Figure 7.3 Schematic of the EK flow of a non-Newtonian nanofluids through a micro/nano-channel.

7.2.4 FO-EK energy conversion by recycling brackish solution

The EO-EK energy conversion system is initially proposed to generate electric energy by utilizing the salinity gradient at the river mouth where the riverwater meets with the seawater. Beside, this section is going to recommend another potential application as shown in Figure 7.4.a, which combines the so-called membrane capacitive deionization (MCDI) technique and the FO-EK technique. This hybrid system, shortly named as MCDI-FO-EK system, is proposed to produce deionized water and simultaneously generate electric power.

Particularly, a MCDI device, integrating both the advantages of carbon nanotubes/carbon nanofibers (CNTs/CNFs) composite film and ion-exchange membrane, was proposed to intermittently generate deionized water with a byproduct of brackish solution [157]. The corresponding operation principle of the MCDI device is summarized in Figure 7.4.b. In order to achieve continuous operating mode, two MCDI devices, as

shown in Figure 7.4.c, are employed in the MCDI module. When MCDI-A is in the recovery mode, the energy stored in this unit will be released to MCDI-B to achieve the deionization process in the second unit. Once the MCDI-B is saturated, the charging process will be reverted, which means the MCDI-B releases energy to the MCDI-A to accomplish the desalination process. Clearly, this special design can continuously generate deionized water with a byproduct of brackish solution. Then the brackish solution goes into the FO-EK module to driven the energy conversion process and thus generates electricity.

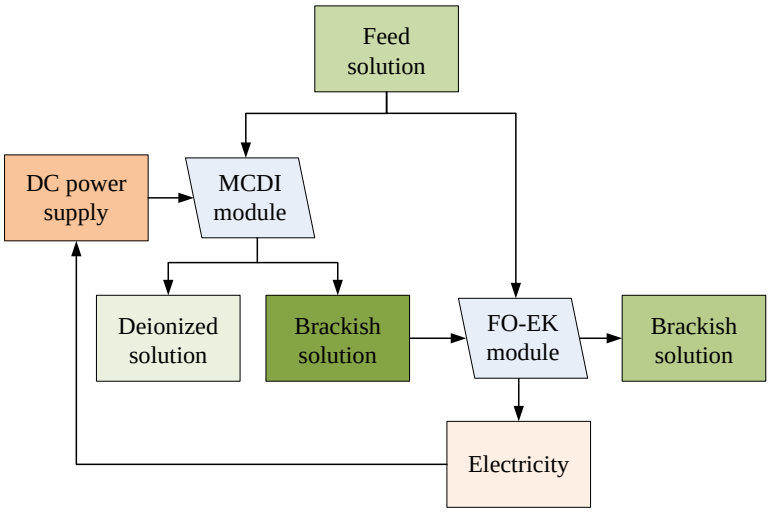

a

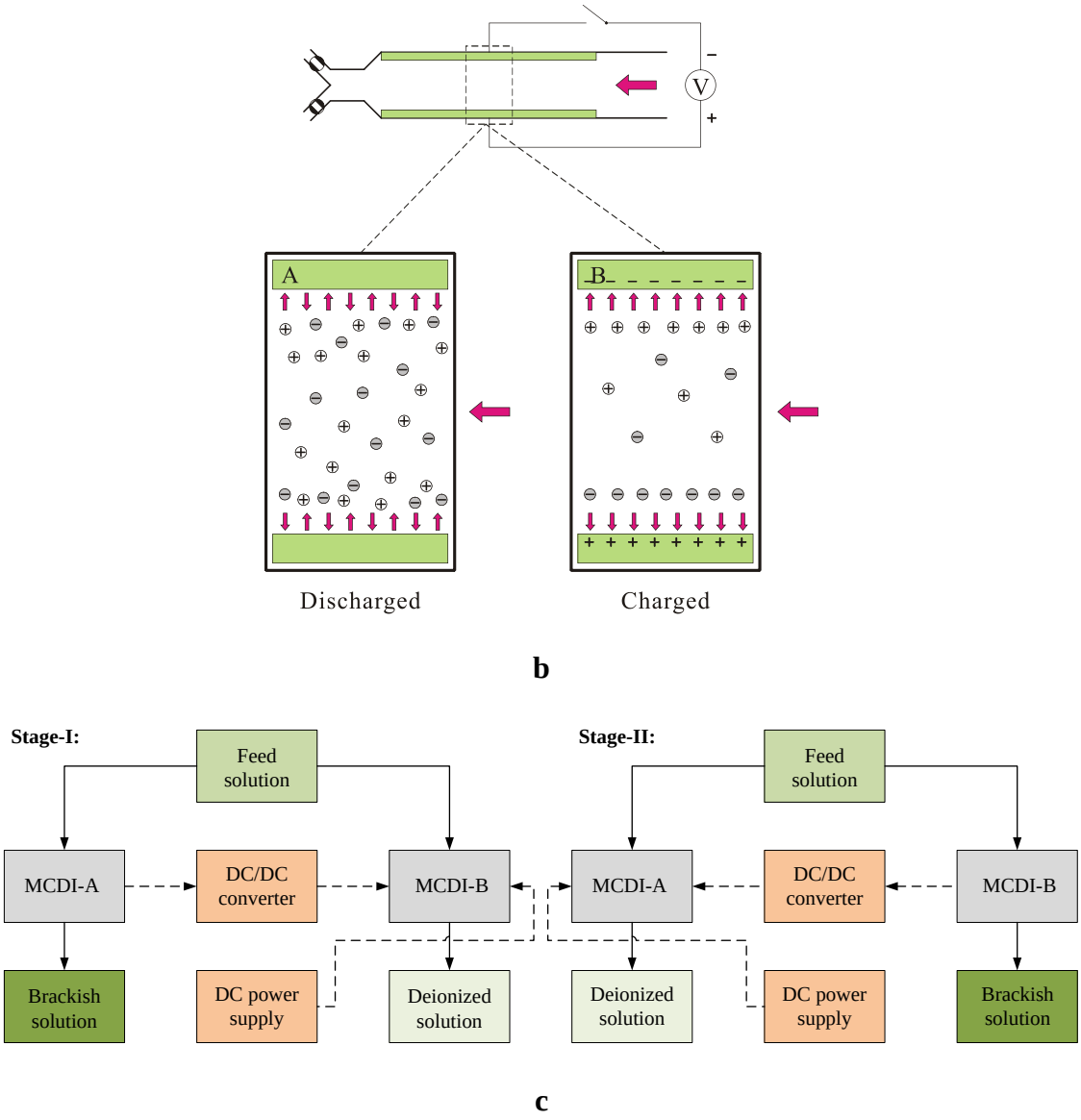

Figure 7.4 a. Flow chart of the Membrane Capacitive Deionization-Forward Osmosis-Electrokinetic (MCDI-FO-EK) system. b. Operation principle of a single MCDI device. Phase A: The carbon electrodes are initially uncharged, i.e., in the state of PZC (potential of zero potential). Phase B: When the electrodes are charged, the electrodes surfaces will adsorb counterions; this is a deionization process. c. Flow chart of the MCDI module in continuous operating mode.

References

1. Norman, R.S., *Water salination: a source of energy.* Science, 1974. **186**(4161): p. 350-352.
2. Kiviat, F.E., *Energy recovery from saline water by means of electrochemical cells.* Science, 1976. **194**(4266): p. 719-720.
3. Ramon, G.Z., B.J. Feinberg, and E.M.V. Hoek, *Membrane-based Production of Salinity-gradient Power*. Energy & Environmental Science, 2011. **4**: p. 4423-4434.
4. Sales, B.B., et al., *Direct power production from a water salinity difference in a membrane-modified supercapacitor flow cell.* Environmental Science and Technology, 2010. **44**(14): p. 5661-5665.
5. Rica, R.A., et al., *Ions transport and adsorption mechanisms in porous electrodes during capacitive-mixing double layer expansion (CDLE).* Journal of Physical Chemistry C, 2012. **116**(32): p. 16934-16938.
6. Burheim, O.S., et al., *Faster time response by the use of wire electrodes in capacitive salinity gradient energy systems.* Journal of Physical Chemistry C, 2012. **116**(36): p. 19203-19210.
7. Achilli, A., T.Y. Cath, and A.E. Childress, *Power generation with pressure retarded osmosis: an experimental and theoretical investigation.* Journal of Membrane Science, 2009. **343**(1-2): p. 42-52.
8. Zhao, K. and H. Wu, *Size effects of pore density and solute size on water osmosis through nanoporous membrane.* Journal of Physical Chemistry B, 2012. **116**(45): p. 13459-13466.
9. Dlugolecki, P., et al., *Practical potential of reverse electrodialysis as process for sustainable energy generation.* Environmental Science and Technology, 2009. **43**(17): p. 6888-6894.
10. Brogioli, D., *Extracting renewable energy from a salinity difference using a capacitor.* Physical Review Letters, 2009. **103**(5): p. 058501.
11. La Mantia, F., et al., *Batteries for efficient energy extraction from a water salinity difference.* Nano Letters, 2011. **11**(4): p. 1810-1813.
12. Pasta, M., et al., *A desalination battery.* Nano Letters, 2012. **12**(2): p. 839-843.
13. Yang, C., K.C. Hon, and S.C. Low, *A method and systems for electrokinetic power generation by forward osmosis*. 2011, U.S. Patent.

14. Hon, K.C., et al., *A method of producing electrokinetic power through forward osmosis.* Applied Physics Letters, 2012. **101**(14): p. 143902.

15. Everett, D.H., *Basic principles of colloid science*. Royal Society of Chemistry paperbacks. 1988, London: Royal Society of Chemistry. xv, 243 p.

16. Hunter, R.J., *Zeta potential in colloid science : principles and applications*. Colloid science,. 1981, London ; New York: Academic Press. xi, 386 p.

17. Iler, R.K., *The chemistry of silica : solubility, polymerization, colloid and surface properties, and biochemistry*. 1979, New York: Wiley. xxiv, 866 p.

18. Bard, A.J. and L.R. Faulkner, *Electrochemical methods : fundamentals and applications*. 2nd ed. 2001, New York: Wiley. xxi, 833 p.

19. Masliyah, J.H. and S. Bhattacharjee, *Electrokinetic and colloid transport phenomena*. 2006, Hoboken, N.J.: Wiley-Interscience. xxiv, 707 p.

20. Probstein, R.F., *Physicochemical hydrodynamics an introduction*. 2005, John Wiley & Sons, Inc.: Hoboken.

21. Wang, L., et al., *Study on pressurizing electroosmosis pump for chromatographic separation.* Talanta, 2006. **70**(2): p. 358-363.

22. Takamura, Y., et al., *Low-voltage electroosmosis pump for stand-alone microfluidics devices.* Electrophoresis, 2003. **24**(1-2): p. 185-192.

23. L'Hostis, F., et al., *Solid state AC electroosmosis micro pump on a Chip.* 2006 International Conference on Nanoscience and Nanotechnology, Vols 1 and 2, 2006: p. 463-466.

24. Guo, Q.Q., et al., *Design of a relaying electroosmosis pump driven by low-voltage DC.* Microsystem Technologies-Micro-and Nanosystems-Information Storage and Processing Systems, 2009. **15**(7): p. 1009-1015.

25. Schoch, R.B., J. Han, and P. Renaud, *Transport phenomena in nanofluidics.* Reviews of Modern Physics, 2008. **80**(3): p. 839-883.

26. Oddy, M.H. and J.G. Santiago, *A method for determining electrophoretic and electroosmotic mobilities using AC and DC electric field particle displacements.* Journal of Colloid and Interface Science, 2004. **269**(1): p. 192-204.

27. Lu, M.C., et al., *A mechanical-electrokinetic battery using a nano-porous membrane.* Journal of Micromechanics and Microengineering, 2006. **16**(4): p. 667-675.

28. Yang, J., et al., *Electrokinetic microchannel battery by means of electrokinetic and microfluidic phenomena*. Journal of Micromechanics and Microengineering, 2003. **13**(6): p. 963-970.

29. Daiguji, H., et al., *Theoretical study on the efficiency of nanofluidic batteries.* Electrochemistry Communications, 2006. **8**(11): p. 1796-1800.

30. Pennathur, S., J.C. Eijkel, and A. van den Berg, *Energy conversion in microsystems: is there a role for micro/nanofluidics?* Lab on a Chip, 2007. **7**(10): p. 1234-7.

31. Wang, M.R. and Q.J. Kang, *Electrochemomechanical energy conversion efficiency in silica nanochannels.* Microfluidics and Nanofluidics, 2010. **9**(2-3): p. 181-190.

32. Chang, C.-C. and R.-J. Yang, *Electrokinetic energy conversion in micrometer-length nanofluidic channels.* Microfluidics and Nanofluidics, 2009. **9**(2-3): p. 225-241.

33. van der Heyden, F.H.J., et al., *Electrokinetic energy conversion efficiency in nanofluidic channels.* Nano Letters, 2006. **6**(10): p. 2232-2237.

34. Yang, C. and D. Li, *Analysis of electrokinetic effects on the liquid flow in rectangular microchannels.* Colloids and Surfaces A, 1998. **143**(2–3): p. 339-353.

35. Kwok, D.Y. and J. Yang, *Effect of liquid slip in electrokinetic parallel-plate microchannel flow.* Journal of Colloid and Interface Science, 2003. **260**(1): p. 225-233.

36. Daiguji, H., et al., *Electrochemomechanical energy conversion in nanofluidic channels.* Nano Letters, 2004. **4**(12): p. 2315-2321.

37. Olthuis, W., et al., *Energy from streaming current and potential.* Sensors and Actuators B: Chemical, 2005. **111-112**: p. 385-389.

38. Chun, M.S., T.S. Lee, and N.W. Choi, *Microfluidic analysis of electrokinetic streaming potential induced by microflows of monovalent electrolyte solution.* Journal of Micromechanics and Microengineering, 2005. **15**(4): p. 710-719.

39. van der Heyden, F.H.J., D. Stein, and C. Dekker, *Streaming currents in a single nanofluidic channel.* Physical Review Letters, 2005. **95**(11).

40. Mirbozorgi, S.A., H. Niazmand, and M. Renksizbulut, *Streaming electric potential in pressure-driven flows through reservoir-connected microchannels.* Journal of Fluids Engineering, 2007. **129**(10): p. 1346.

41. van der Heyden, F.H.J., et al., *Power generation by pressure-driven transport of ions in nanofluidic channels.* Nano Letters, 2007. **7**(4): p. 1022-1025.

42. Ren, Y. and D. Stein, *Slip-enhanced electrokinetic energy conversion in nanofluidic channels.* Nanotechnology, 2008. **19**(19): p. 195707.

43. Soong, C.Y., P.W. Hwang, and J.C. Wang, *Analysis of pressure-driven electrokinetic flows in hydrophobic microchannels with slip-dependent zeta potential.* Microfluidics and Nanofluidics, 2009. **9**(2-3): p. 211-223.

44. Wu, J.K. and L. Wang, *Flow behavior in microchannel made of different materials with wall slip velocity and electro-viscous effects.* Acta Mechanica Sinica, 2010. **26**(1): p. 73-80.

45. Renksizbulut, M., J. Jamaati, and H. Niazmand, *Pressure-driven electrokinetic slip-flow in planar microchannels.* International Journal of Thermal Sciences, 2010. **49**(7): p. 1165-1174.

46. Joly, L., et al., *Hydrodynamics within the Electric Double Layer on Slipping Surfaces.* Physical Review Letters, 2004. **93**(25): p. 257805.

47. Joly, L., et al., *Liquid friction on charged surfaces: from hydrodynamic slippage to electrokinetics.* The Journal of chemical physics, 2006. **125**(20): p. 204716.

48. Bouzigues, C.I., P. Tabeling, and L. Bocquet, *Nanofluidics in the debye layer at hydrophilic and hydrophobic surfaces.* Physical Review Letters, 2008. **101**(11): p. 114503.

49. Meyer, E.E., K.J. Rosenberg, and J. Israelachvili, *Recent progress in understanding hydrophobic interactions.* Proceedings of the National Academy of Sciences of the United States of America, 2006. **103**(43): p. 15739-46.

50. Churaev, N.V., et al., *Electrokinetic properties of methylated quartz capillaries.* Advances in Colloid and Interface Science, 2002. **96**(1-3): p. 265-278.

51. Stone, H.A., A.D. Stroock, and A. Ajdari, *Engineering flows in small devices.* Annual Review of Fluid Mechanics, 2004. **36**(1): p. 381-411.

52. Davidson, C. and X. Xuan, *Electrokinetic energy conversion in slip nanochannels.* Journal of Power Sources, 2008. **179**(1): p. 297-300.

53. Einzel, D., P. Panzer, and M. Liu, *Boundary condition for fluid flow: curved or rough surfaces.* Physical Review Letters, 1990. **64**(19): p. 2269.

54. Eijkel, J., *Liquid slip in micro- and nanofluidics: recent research and its possible implications.* Lab on a Chip, 2007. **7**(3): p. 299-301.

55. Chang, C.-C. and R.-J. Yang, *Electrokinetic energy conversion in micrometer-length nanofluidic channels.* Microfluidics and Nanofluidics, 2010. **9**(2-3): p. 225-241.

56. Yan, Y., et al., *Energy conversion efficiency of nanofluidic batteries: hydrodynamic slip and access resistance.* The Journal of Physical Chemistry C, 2013. **117**(16): p. 8050-8061.

57. Ehlert, S., D. Hlushkou, and U. Tallarek, *Electrohydrodynamics around single ion-permselective glass beads fixed in a microfluidic device.* Microfluidics and Nanofluidics, 2008. **4**(6): p. 471-487.

58. Nischang, I., et al., *Concentration polarization and nonequilibrium electroosmotic slip in hierarchical monolithic structures.* Electrophoresis, 2008. **29**(5): p. 1140-1151.

59. Nischang, I., et al., *Concentration polarization and nonequilibrium electroosmotic slip in dense multiparticle systems.* Langmuir, 2007. **23**(18): p. 9271-9281.

60. Nischang, I., G.F. Chen, and U. Tallarek, *Electrohydrodynamics in hierarchically structured monolithic and particulate fixed beds.* Journal of Chromatography A, 2006. **1109**(1): p. 32-50.

61. Suss, M.E., et al., *Electroosmotic pump performance is affected by concentration polarizations of both electrodes and pump.* Sensors and Actuators A: Physical, 2011. **165**(2): p. 310-315.

62. Zangle, T.A., A. Mani, and J.G. Santiago, *On the propagation of concentration polarization from microchannel-nanochannel interfaces Part II: Numerical and experimental study.* Langmuir, 2009. **25**(6): p. 3909-3916.

63. BEN, Y. and H.-C. CHANG, *Nonlinear Smoluchowski slip velocity and micro-vortex generation.* Journal of Fluid Mechanics, 2002. **461**: p. 229-238.

64. Mishchuk, N.A. and P.V. Takhistov, *Electroosmosis of the second kind.* Colloids and Surfaces A: Physicochemical and Engineering Aspects, 1995. **95**(2–3): p. 119-131.

65. Manzanares, J.A., et al., *Numerical simulation of the nonequilibrium diffuse double layer in ion-exchange membranes.* The Journal of Physical Chemistry, 1993. **97**(32): p. 8524-8530.

66. Dukhin, S.S., *Electrokinetic phenomena of the second kind and their applications.* Advances in Colloid and Interface Science, 1991. **35**(0): p. 173-196.

67. Mirbozorgi, S.A., H. Niazmand, and M. Renksizbulut, *Streaming electric potential in pressure-driven flows through reservoir-connected microchannels.* Journal of Fluids Engineering, 2007. **129**(10): p. 1346-1357.

68. Chein, R., C. Liao, and H. Chen, *Electrokinetic energy conversion efficiency analysis using nanoscale finite-length surface-charged capillaries.* Journal of Power Sources, 2009. **187**(2): p. 461-470.

69. Leinweber, F.C. and U. Tallarek, *Nonequilibrium Electrokinetic Effects in Beds of Ion-Permselective Particles.* Langmuir, 2004. **20**(26): p. 11637-11648.

70. Strathmann, H., *Ion-exchange membrane separation processes*. 2004, Elsevier: Burlington.

71. Cath, T.Y., A.E. Childress, and M. Elimelech, *Forward osmosis: principles, applications, and recent developments.* Journal of Membrane Science, 2006. **281**(1-2): p. 70-87.

72. Chung, T.-S., et al., *Forward osmosis processes: Yesterday, today and tomorrow.* Desalination, 2011(0).

73. Holloway, R.W., et al., *Forward osmosis for concentration of anaerobic digester centrate.* Water Research, 2007. **41**(17): p. 4005-4014.

74. Zhang, S., et al., *Well-constructed cellulose acetate membranes for forward osmosis: Minimized internal concentration polarization with an ultra-thin selective layer.* Journal of Membrane Science, 2010. **360**(1-2): p. 522-535.

75. Su, J., et al., *Cellulose acetate nanofiltration hollow fiber membranes for forward osmosis processes.* Journal of Membrane Science, 2010. **355**(1-2): p. 36-44.

76. Wang, K.Y., R.C. Ong, and T.S. Chung, *Double-skinned forward osmosis membranes for reducing internal concentration polarization within the porous sublayer.* Industrial and Engineering Chemistry Research, 2010. **49**(10): p. 4824-4831.

77. Wang, K.Y., et al., *Enhanced forward osmosis from chemically modified polybenzimidazole (PBI) nanofiltration hollow fiber membranes with a thin wall.* Chemical Engineering Science, 2009. **64**(7): p. 1577-1584.

78. Wang, K.Y., T.S. Chung, and J.J. Qin, *Polybenzimidazole (PBI) nanofiltration hollow fiber membranes applied in forward osmosis process.* Journal of Membrane Science, 2007. **300**(1-2): p. 6-12.

79. Gerstandt, K., et al., *Membrane processes in energy supply for an osmotic power plant.* Desalination, 2008. **224**(1-3): p. 64-70.

80. Wang, R., et al., *Characterization of novel forward osmosis hollow fiber membranes.* Journal of Membrane Science, 2010. **355**(1-2): p. 158-167.

81. McCutcheon, J.R. and M. Elimelech, *Influence of membrane support layer hydrophobicity on water flux in osmotically driven membrane processes.* Journal of Membrane Science, 2008. **318**(1-2): p. 458-466.

82. Elimelech, M., J.R. McCutcheon, and R.L. McGinnis, *Desalination by ammonia-carbon dioxide forward osmosis: Influence of draw and feed solution concentrations on process performance.* Journal of Membrane Science, 2006. **278**(1-2): p. 114-123.

83. Mulder, M., *Basic principles of membrane technology*. 2nd ed. 1996, Dordrecht ; Boston: Kluwer Academic. 564 p.

84. Mehta, G.D. and S. Loeb, *Internal polarization in the porous substructure of a semipermeable membrane under pressure-retarded osmosis.* Journal of Membrane Science, 1978. **4**(2): p. 261-265.

85. Loeb, S. and R.S. Norman, *Osmotic power plants.* Science, 1975. **189**(4203): p. 654-655.

86. McCutcheon, J.R. and M. Elimelech, *Influence of concentrative and dilutive internal concentration polarization on flux behavior in forward osmosis.* Journal of Membrane Science, 2006. **284**(1-2): p. 237-247.

87. Tan, C.H. and H.Y. Ng, *Modified models to predict flux behavior in forward osmosis in consideration of external and internal concentration polarizations.* Journal of Membrane Science, 2008. **324**(1-2): p. 209-219.

88. Robinson, R.A. and R.H. Stokes, *Tables of osmotic and activity coefficients of electrolytes in aqueous solution at 25-degrees-c.* Transactions of the Faraday Society, 1949. **45**(7): p. 612-624.

89. McCutcheon, J.R. and M. Elimelech, *Modeling water flux in forward osmosis: Implications for improved membrane design.* Aiche Journal, 2007. **53**(7): p. 1736-1744.

90. Guillen, G. and E.M.V. Hoek, *Modeling the impacts of feed spacer geometry on reverse osmosis and nanofiltration processes.* Chemical Engineering Journal, 2009. **149**(1-3): p. 221-231.

91. Lorenz, P.B., *The phenomenology of electro-osmosis and streaming potential.* Journal of Physical Chemistry, 1952. **56**(6): p. 775-778.

92. Yang, C., D. Li, and J.H. Masliyah, *Modeling forced liquid convection in rectangular microchannels with electrokinetic effects.* International Journal of Heat and Mass Transfer, 1998. **41**(24): p. 4229-4249.

93. Rice, C.L. and R. Whitehead, *Electrokinetic flow in a narrow cylindrical capillary.* Journal of Physical Chemistry, 1965. **69**(11): p. 4017-4024.

94. Yang, C. and D. Li, *Electrokinetic effects on pressure-driven liquid flows in rectangular microchannels.* Journal of Colloid and Interface Science, 1997. **194**(1): p. 95-107.

95. Kang, Y., C. Yang, and X. Huang, *Electroosmotic flow in a capillary annulus with high zeta potentials.* Journal of Colloid and Interface Science, 2002. **253**(2): p. 285-294.

96. Mazur, P. and J.T.G. Overbeek, *On electro-osmosis and streaming-potentials in diaphragms: II. General quantitative relationship between electro-kinetic effects.* Recueil des Travaux Chimiques des Pays-Bas, 1951. **70**(1): p. 83-91.

97. Liapis, A.I. and J.J. Meyers, *Network modeling of the convective flow and diffusion of molecules adsorbing in monoliths and in porous particles packed in a chromatographic column.* Journal of Chromatography A, 1999. **852**(1): p. 3-23.

98. Liapis, A.I. and J.J. Meyers, *Network modeling of the intraparticle convection and diffusion of molecules in porous particles packed in a chromatographic column.* Journal of Chromatography A, 1998. **827**(2): p. 197-213.

99. Santiago, J.G., et al., *Porous glass electroosmotic pumps: design and experiments.* Journal of Colloid and Interface Science, 2003. **268**(1): p. 143-153.

100. Saksena, S. and A.L. Zydney, *Pore-size distribution effects on electrokinetic phenomena in semipermeable membranes.* Journal of Membrane Science, 1995. **105**(3): p. 203-215.

101. Nield, D.A. and A. Bejan, *Convection in porous media*. 3rd ed. 2006, New York: Springer. xxiii, 640 p.

102. Brown, G., *The history of the Darcy-Weisbach equation for pipe flow resistance*, in *Environmental and Water Resources History*. 2002. p. 34-43.

103. Lee, T., et al., *The electrokinetic microfluidic flow in multi-channels with emergent applicability toward micro power generation.* Korean Journal of Chemical Engineering, 2005. **22**(4): p. 528-535.

104. Gruber, M.F., et al., *Computational fluid dynamics simulations of flow and concentration polarization in forward osmosis membrane systems.* Journal of Membrane Science, 2011. **379**(1–2): p. 488-495.

105. Sagiv, A. and R. Semiat, *Finite element analysis of forward osmosis process using NaCl solutions.* Journal of Membrane Science, 2011. **379**(1–2): p. 86-96.

106. Jin, X., et al., *Removal of boron and arsenic by forward osmosis membrane: Influence of membrane orientation and organic fouling.* Journal of Membrane Science, 2012. **389**(0): p. 182-187.

107. Widjojo, N., et al., *The role of sulphonated polymer and macrovoid-free structure in the support layer for thin-film composite (TFC) forward osmosis (FO) membranes.* Journal of Membrane Science, 2011. **383**(1–2): p. 214-223.

108. Park, M., et al., *Determination of a constant membrane structure parameter in forward osmosis processes.* Journal of Membrane Science, 2011. **375**(1–2): p. 241-248.

109. Tang, C.Y., et al., *Coupled effects of internal concentration polarization and fouling on flux behavior of forward osmosis membranes during humic acid filtration.* Journal of Membrane Science, 2010. **354**(1–2): p. 123-133.

110. Ge, Q.C., et al., *Exploration of polyelectrolytes as draw solutes in forward osmosis processes.* Water Research, 2012. **46**(4): p. 1318-1326.

111. Yong, J.S., W.A. Phillip, and M. Elimelech, *Coupled reverse draw solute permeation and water flux in forward osmosis with neutral draw solutes.* Journal of Membrane Science, 2012. **392–393**(0): p. 9-17.

112. Zhao, S. and L. Zou, *Relating solution physicochemical properties to internal concentration polarization in forward osmosis.* Journal of Membrane Science, 2011. **379**(1–2): p. 459-467.

113. Yen, S.K., et al., *Study of draw solutes using 2-methylimidazole-based compounds in forward osmosis.* Journal of Membrane Science, 2010. **364**(1–2): p. 242-252.

114. Garcia-Castello, E.M., J.R. McCutcheon, and M. Elimelech, *Performance evaluation of sucrose concentration using forward osmosis.* Journal of Membrane Science, 2009. **338**(1-2): p. 61-66.

115. McCormick, P., et al., *Water, salt, and ethanol diffusion through membranes for water recovery by forward (direct) osmosis processes.* Journal of Membrane Science, 2008. **325**(1): p. 467-478.

116. Achilli, A., T.Y. Cath, and A.E. Childress, *Selection of inorganic-based draw solutions for forward osmosis applications.* Journal of Membrane Science, 2010. **364**(1–2): p. 233-241.

117. Zhang, S., et al., *Cellulose esters for forward osmosis: characterization of water and salt transport properties and free volume.* Polymer, 2012. **53**(13): p. 2664-2672.

118. Qi, S., et al., *Double-skinned forward osmosis membranes based on layer-by-layer assembly—FO performance and fouling behavior.* Journal of Membrane Science, 2012. **405–406**(0): p. 20-29.

119. Su, J., et al., *Enhanced double-skinned FO membranes with inner dense layer for wastewater treatment and macromolecule recycle using Sucrose as draw solute.* Journal of Membrane Science, 2012. **396**(0): p. 92-100.

120. Fang, W., et al., *Composite forward osmosis hollow fiber membranes: integration of RO- and NF-like selective layers to enhance membrane properties of anti-scaling and anti-internal concentration polarization.* Journal of Membrane Science, 2012. **394–395**(0): p. 140-150.

121. Setiawan, L., et al., *Fabrication and characterization of forward osmosis hollow fiber membranes with antifouling NF-like selective layer.* Journal of Membrane Science, 2012. **394–395**(0): p. 80-88.

122. Arena, J.T., et al., *Surface modification of thin film composite membrane support layers with polydopamine: Enabling use of reverse osmosis membranes in pressure retarded osmosis.* Journal of Membrane Science, 2011. **375**(1–2): p. 55-62.

123. Wei, J., et al., *Synthesis and characterization of flat-sheet thin film composite forward osmosis membranes.* Journal of Membrane Science, 2011. **372**(1–2): p. 292-302.

124. Setiawan, L., et al., *Fabrication of novel poly(amide–imide) forward osmosis hollow fiber membranes with a positively charged nanofiltration-like selective layer.* Journal of Membrane Science, 2011. **369**(1–2): p. 196-205.

125. Mi, B. and M. Elimelech, *Chemical and physical aspects of organic fouling of forward osmosis membranes.* Journal of Membrane Science, 2008. **320**(1–2): p. 292-302.

126. Loeb, S., et al., *Effect of porous support fabric on osmosis through a Loeb-Sourirajan type asymmetric membrane.* Journal of Membrane Science, 1997. **129**(2): p. 243-249.

127. Mehta, G.D., *Further results on the performance of present-day osmotic membranes in various osmotic regions.* Journal of Membrane Science, 1982. **10**(1): p. 3-19.

128. Mehta, G.D. and S. Loeb, *Performance of permasep B-9 and B-10 membranes in various osmotic regions and at high osmotic pressures.* Journal of Membrane Science, 1978. **4**(0): p. 335-349.

129. Cath, T.Y., D. Adams, and A.E. Childress, *Membrane contactor processes for wastewater reclamation in space: II. Combined direct osmosis, osmotic distillation, and membrane distillation for treatment of metabolic wastewater.* Journal of Membrane Science, 2005. **257**(1–2): p. 111-119.

130. Cath, T.Y., et al., *Membrane contactor processes for wastewater reclamation in space: Part I. Direct osmotic concentration as pretreatment for reverse osmosis.* Journal of Membrane Science, 2005. **257**(1–2): p. 85-98.

131. Jung, D.H., et al., *Simulation of forward osmosis membrane process: Effect of membrane orientation and flow direction of feed and draw solutions.* Desalination, 2011. **277**(1-3): p. 83-91.

132. Lee, S., et al., *Comparison of fouling behavior in forward osmosis (FO) and reverse osmosis (RO).* Journal of Membrane Science, 2010. **365**(1–2): p. 34-39.

133. Xiao, D., et al., *A modeling investigation on optimizing the design of forward osmosis hollow fiber modules.* Journal of Membrane Science, 2012. **392–393**(0): p. 76-87.

134. Xiao, D., et al., *Modeling salt accumulation in osmotic membrane bioreactors: Implications for FO membrane selection and system operation.* Journal of Membrane Science, 2011. **366**(1–2): p. 314-324.

135. Lee, K.L., R.W. Baker, and H.K. Lonsdale, *Membranes for power generation by pressure-retarded osmosis.* Journal of Membrane Science, 1981. **8**(2): p. 141-171.

136. Mehta, G.D. and S. Loeb, *Internal polarization in the porous substructure of a semipermeable membrane under pressure-retarded osmosis.* Journal of Membrane Science, 1978. **4**(0): p. 261-265.

137. Loeb, S., *Production of energy from concentrated brines by pressure-retarded osmosis : I. Preliminary technical and economic correlations.* Journal of Membrane Science, 1976. **1**(0): p. 49-63.

138. Gu, B., et al., *Mathematical model of flat sheet membrane modules for FO process: Plate-and-frame module and spiral-wound module.* Journal of Membrane Science, 2011. **379**(1–2): p. 403-415.

139. Li, W., Y. Gao, and C.Y. Tang, *Network modeling for studying the effect of support structure on internal concentration polarization during forward osmosis: Model development and theoretical analysis with FEM.* Journal of Membrane Science, 2011. **379**(1–2): p. 307-321.

140. Ramon, G., Y. Agnon, and C. Dosoretz, *Dynamics of an osmotic backwash cycle.* Journal of Membrane Science, 2010. **364**(1–2): p. 157-166.

141. de Vilhena, M.T., *An analytical solution of the steady state convective-diffusion equation with space dependent diffusion coefficient.* Journal of Membrane Science, 1992. **71**(1–2): p. 51-56.

142. Reali, M., G. Dassie, and G. Jonsson, *Computation of salt concentration profiles in the porous substrate of anisotropic membranes under steady pressure-retarded-osmosis conditions.* Journal of Membrane Science, 1990. **48**(2–3): p. 181-201.

143. Lyster, E. and Y. Cohen, *Numerical study of concentration polarization in a rectangular reverse osmosis membrane channel: Permeate flux variation and hydrodynamic end effects.* Journal of Membrane Science, 2007. **303**(1-2): p. 140-153.

144. Loeb, S., F. Van Hessen, and D. Shahaf, *Production of energy from concentrated brines by pressure-retarded osmosis : II. Experimental results and projected energy costs.* Journal of Membrane Science, 1976. **1**(0): p. 249-269.

145. Jensen, K.H., et al., *Osmotically driven flows in microchannels separated by a semipermeable membrane.* Lab on a Chip, 2009. **9**(14): p. 2093-2099.

146. Culbertson, C.T., S.C. Jacobson, and J. Michael Ramsey, *Diffusion coefficient measurements in microfluidic devices.* Talanta, 2002. **56**(2): p. 365-373.

147. Munson, B.R., et al., *Fundamentals of fluid mechanics*. 2013: Hoboken, NJ : John Wiley & Sons, Inc., ©2013. 7th edition.

148. Bu, K.-H., *Surfactant mediated passivation to achieve chemical mechanical polishing selectivity*. 2007, University of Florida: Ann Arbor. p. 133.

149. Bolis, V., et al., *Hydrophilic and hydrophobic sites on dehydrated crystalline and amorphous silicas.* Journal of the Chemical Society-Faraday Transactions, 1991. **87**(3): p. 497-505.

150. Ismail, F., C. Malins, and N.J. Goddard, *Alkali treatment of dye-doped sol-gel glass films for rapid optical pH sensing.* Analyst, 2002. **127**(2): p. 253-257.

151. Nabeshi, H., et al., *Effect of surface properties of silica nanoparticles on their cytotoxicity and cellular distribution in murine macrophages.* Nanoscale research letters, 2011. **6**(1): p. 93.

152. Shin, Y., et al., *Surface properties of silica nanoparticles modified with polymers for polymer nanocomposite applications.* Journal of Industrial and Engineering Chemistry, 2008. **14**(4): p. 515-519.

153. Berli, C.L.A., *Output pressure and efficiency of electrokinetic pumping of non-Newtonian fluids.* Microfluidics and Nanofluidics, 2009. **8**(2): p. 197-207.

154. Bird, R.B., *Dynamics of polymeric liquids*. 2nd ed. 1987, New York: Wiley.

155. Chein, R., K. Tsai, and L. Yeh, *Analysis of effect of electrolyte types on electrokinetic energy conversion in nanoscale capillaries.* Electrophoresis, 2010. **31**(3): p. 535-45.

156. Xuan, X. and D. Li, *Thermodynamic analysis of electrokinetic energy conversion.* Journal of Power Sources, 2006. **156**(2): p. 677-684.

157. Li, H., et al., *Electrosorptive desalination by carbon nanotubes and nanofibres electrodes and ion-exchange membranes.* Water Research, 2008. **42**(20): p. 4923-4928.

Publications

Journal papers

1. **Yanmei Jiao**, Chun Yang, and Yuejun Kang, "Energy Conversion from Salinity Gradients by Forward Osmosis-Electrokinetics", Journal of Physical Chemistry C. 2014 118(20), 10574-10583.
2. **Yanmei Jiao**, Chun Yang, and Yuejun Kang, "Study of External Concentration Polarization in Forward Osmosis" (In written).
3. **Yanmei Jiao**, Chun Yang, and Yuejun Kang, "Numerical study on electric properties of pressure-driven electrokinetic process" (In written).

Conference papers

1. **Yanmei Jiao**, Chun Yang, Yuejun Kang, Kar Cherng Hon, "Enhancement of Elecrtrokinetic Power Generation by Surface Treatment on a Porous Glass", The 3rd International Conference on Informatics, Environment, Energy and Applications (IEEA 2014), Shanghai, China. DOI: 10.7763/IPCBEE. 2014. V66.12.

Encyclopedia chapters

1. **Yanmei Jiao**, Yuejun Kang, Chun Yang, "Osmosis and its applications", Encyclopedia of Microfluidics and Nanofluidics, DOI 10.1007/978-3-642-27758-0_1741-1, 2013.

Appendices

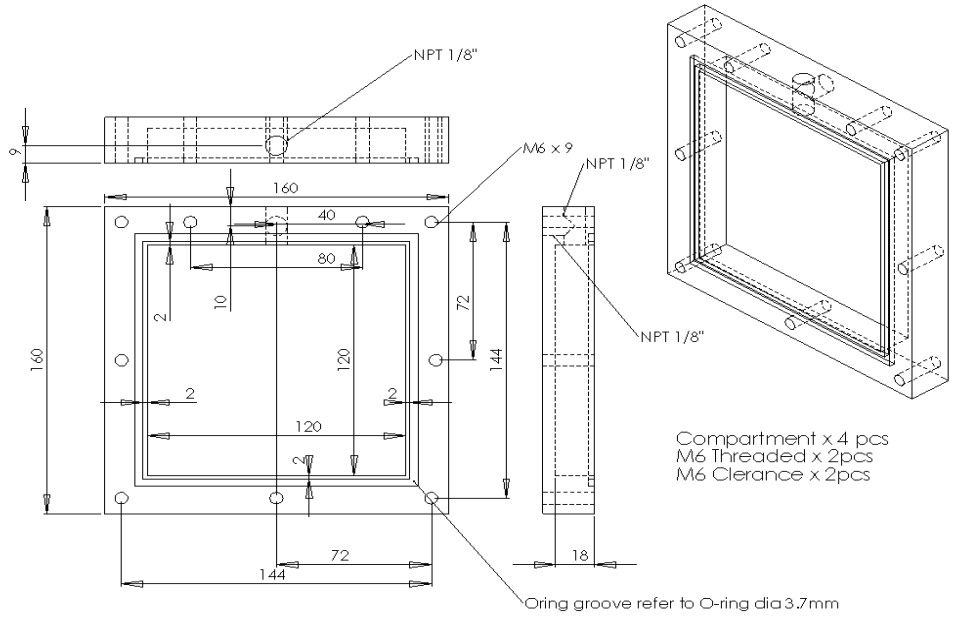

Appendix A. Forward osmosis (FO) submodule assembly with unit of mm.

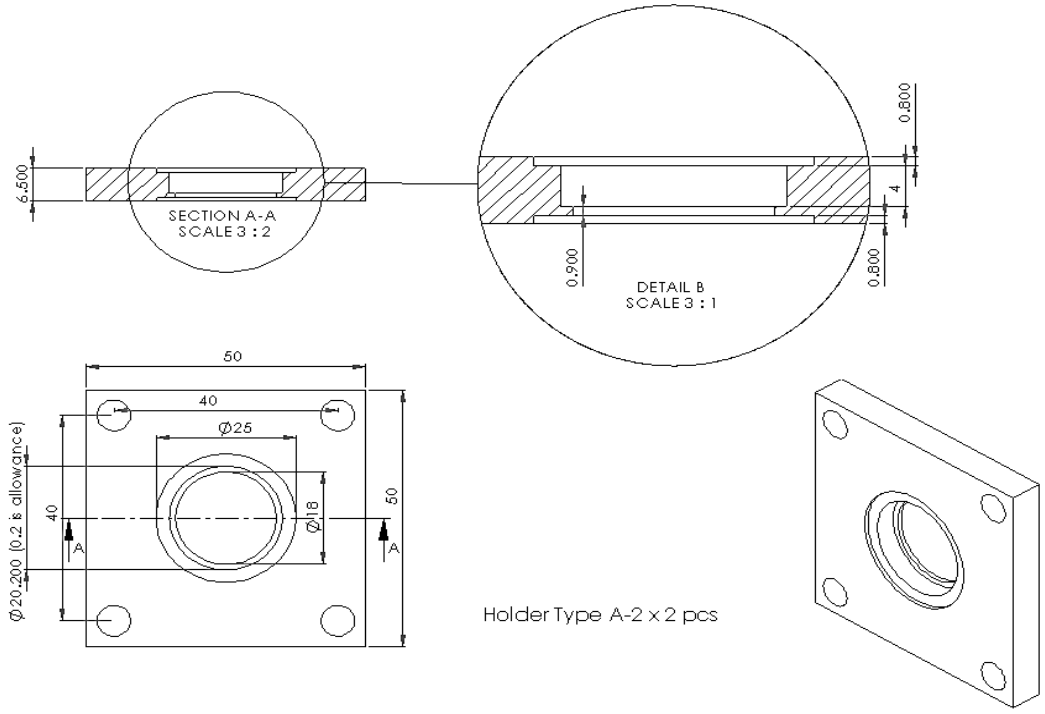

Appendix B. Electrokinetic (EK) submodule assembly with unit of mm.

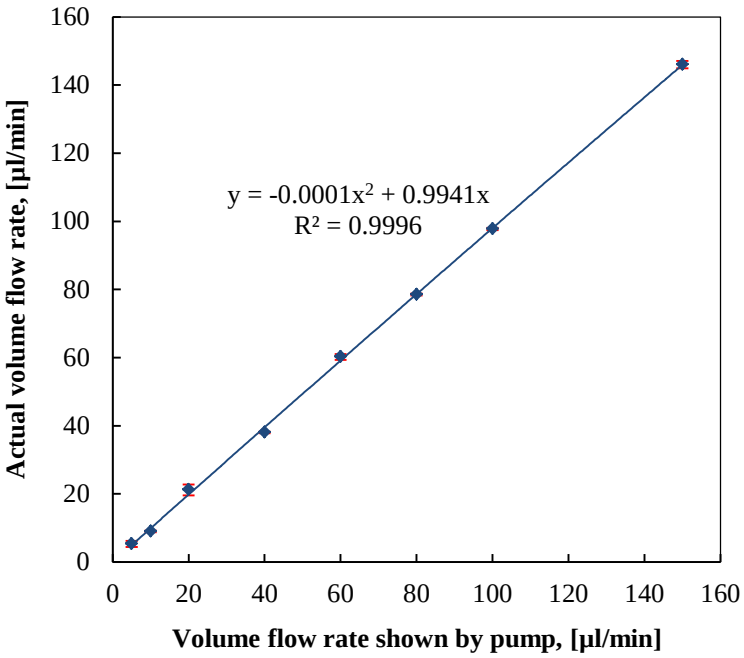

Appendix C. Calibrated relationship between volume flow rate shown by pump and actual volume flow rate. The discrete data are obtained from calibration experiment and the solid curve represents the fitted relationship between the displayed volume flow rate and the real volume flow rate.